arXiv:0708.0790v2 [astro-ph] 1 Nov 2007

STELLAR EVOLUTIONARY EFFECTS ON THE ABUNDANCES OF PAH AND SN-CONDENSED DUST IN GALAXIES

Frédéric Galliano, Eli Dwek

Observational Cosmology Lab., Code 665, NASA Goddard Space Flight Center, Greenbelt MD 20771, USA

`galliano@astro.umd.edu`

and

Pierre Chanial

Astrophysics Group, Blackett Laboratory, Imperial College, Prince Consort Road, London SW7 2AZ, UK

ABSTRACT

Spectral and photometric observations of nearby galaxies show a correlation between the strength of their mid-IR aromatic features, attributed to PAH molecules, and their metal abundance, leading to a deficiency of these features in low-metallicity galaxies. In this paper, we suggest that the observed correlation represents a trend of PAH abundance with galactic age, reflecting the delayed injection of carbon dust into the ISM by AGB stars in the final post-AGB phase of their evolution. AGB stars are the primary sources of PAHs and carbon dust in galaxies, and recycle their ejecta back to the interstellar medium only after a few hundred million years of evolution on the main sequence. In contrast, more massive stars that explode as Type II supernovae inject their metals and dust almost instantaneously after their formation. We first determined the PAH abundance in galaxies by constructing detailed models of UV-to-radio SED of galaxies that estimate the contribution of dust in PAH-free H II regions, and PAHs and dust from photodissociation regions, to the IR emission. All model components: the galaxies' stellar content, properties of their H II regions, and their ionizing and non-ionizing radiation fields and dust abundances, are constrained by their

observed multiwavelength spectrum. After determining the PAH and dust abundances in 35 nearby galaxies using our SED model, we use a chemical evolution model to show that the delayed injection of carbon dust by AGB stars provides a natural explanation to the dependence of the PAH content in galaxies with metallicity. We also show that larger dust particles giving rise to the far-IR emission follow a distinct evolutionary trend closely related to the injection of dust by massive stars into the ISM.

Subject headings: ISM: dust – infrared: galaxies – galaxies: starburst – galaxies: evolution – stars: post-AGB – supernovae remnants

1. INTRODUCTION

Spectral and photometric observations of nearby galaxies with the *Infrared Space Observatory* (*ISO*) and the *Spitzer Space Telescope* have provided the opportunity to investigate the inter-relations between global galactic properties, such as morphology, star formation activity, spectral energy distribution (SED), metallicity, and dust abundance and composition. In particular, these observations have enabled detailed studies of the correlation of dust abundances and composition with metal enrichment in galaxies spanning a wide range of metallicities. Since the metallicity of galaxies evolves monotonically with time, galaxies with different metallicities provide snapshots of the evolutionary history of galaxies.

An exciting result provided by *ISO* spectral observations of nearby galaxies was the discovery of a striking correlation between the strength of their mid-IR aromatic features and their metallicity (Madden et al. 2006). Low-metallicity galaxies exhibited very weak or no aromatic features. Observations of the 8-to-24 μm bands flux ratio obtained with *Spitzer*/IRAC and *Spitzer*/MIPS instruments showed a correlation of this flux ratio with the galaxies' oxygen abundance (Engelbracht et al. 2005). Since the *Spitzer*/IRAC$_{8\mu m}$ band is supposed to trace the strength of the aromatic features, and the *Spitzer*/MIPS$_{24\mu m}$ that of the continuum emission from the hot non-aromatic dust component, this correlation seemed to confirm the trends discovered by *ISO*. This correlation was independently confirmed by Wu et al. (2006) and O'Halloran et al. (2006) from spectral observations of low-metallicity blue compact dwarf galaxies with the *Spitzer*/IRS instrument.

The aromatic features are most commonly attributed to the vibrational modes of Polycyclic Aromatic Hydrocarbons (PAHs; Léger & Puget 1984; Allamandola et al. 1985), which are large planar molecules made of 50 to 1000 carbon atoms. Their ubiquity makes them an important component of dust models (Désert et al. 1990; Dwek et al. 1997; Zubko et al.

2004; Draine & Li 2007), locking up $\sim 15 - 20\%$ of the total amount of interstellar carbon (Zubko et al. 2004, with solar abundance constraints). They mostly reside in galactic photodissociation regions (PDRs), where they play an important role in the heating of the gas by providing photo-electrons (e.g. Tielens & Hollenbach 1985; Bakes & Tielens 1994), and in interstellar chemistry by providing surfaces for chemical reactions. Because of their small sizes, PAHs are stochastically heated by the interstellar radiation fields. The relative strength of some of the aromatic features depends on their ionization state, and varies therefore significantly with the physical condition of the environment (Hony et al. 2001; Vermeij et al. 2002; Galliano et al. 2007). Understanding the evolution of PAHs and their relation to the global properties of galaxies is therefore extremely important because of the complex mutual influences between PAHs, and their ambient radiative and gaseous surroundings.

Several explanations have been offered for the correlation of the intensity of the PAH features with metallicity. The first suggests that the trend reflects an increase in the destruction efficiency of PAHs in low metallicity environments (Galliano et al. 2003, 2005; Madden et al. 2006). Low-metallicity environments are bathed with harder photons than our Galaxy, due to the higher effective temperature of their stars, and their young age. Moreover, the paucity of dust allows this hard radiation field to penetrate deeper into the ISM, compared to high-metallicity systems, selectively destroying the PAH molecules by photoevaporation or photodissociation. This explanation is consistent with the models of population synthesis and dust evolution of Dwek et al. (2000). Assuming that PAHs are efficiently destroyed by UV photons in H II regions, their models showed an evolutionary trend of PAH features with time, as the relative contribution of ionizing OB stars to the galaxy's SED decreases with time. A second explanation has been proposed by O'Halloran et al. (2006), who suggested that PAHs are destroyed by the numerous shocks observed in low metallicity systems. To support their proposition, they showed an anti-correlation between the PAH-to-continuum ratio and the $[\text{Fe\,II}]_{25.99\mu m}/[\text{Ne\,II}]_{12.81\mu m}$ line ratio, the latter being supposedly a shock tracer. The problem with this explanation is that there is no observational evidence that PAHs are selectively destroyed in shocks. On the contrary, Reach et al. (2002) showed that, in the shocked medium of 3C 391, both the PAH features and the underlying continuum disappear.

All previous explanations attribute the paucity of PAHs to destructive processes that are more efficient in the early stages of galaxy evolution. In contrast, Dwek (2005) suggested that the observed correlation reflects an evolutionary trend of the sources of interstellar PAHs with metallicity. PAHs and carbon dust are mostly produced in asymptotic giant branch (AGB) stars which, unlike massive stars, recycle their ejecta into the ISM after a significantly longer time of main sequence evolution. The observed correlation of PAH line intensities with metallicity is therefore a trend of PAH abundance with galactic age, reflecting the delayed injection of PAHs and carbon dust into the ISM by AGB stars in their final, post-AGB,

phase of their evolution.

Such distinct evolutionary trends of SN and AGB produced dust with time were predicted by Dwek (1998) and more recently by Morgan & Edmunds (2003). In particular, the latter show the evolutionary trend of AGB dust with time. This trend can be translated as a trend with metallicity if galaxies approximately share a global "cosmic" star formation history.

The goal of this paper is to present a detailed evolutionary model to examine whether the observed trend of PAH line intensity with metallicity reflects an evolutionary trend of PAH abundance with metallicity. This requires the determination of PAH abundance from the strength of their aromatic features in the galaxies for which this trend has been observed, and the use of a chemical evolution model to follow the change of PAH abundance with galactic metallicity (Dwek 1998). The paper is organized as follows. We first present in §2 the sample of nearby galaxies that were considered in our analysis. In §3, we describe the method we used to separate the contributions of H II regions and photodissociation regions to the global SED, in order to determine the abundances of PAHs and larger grains in these galaxies in §4. In §5, we briefly describe the chemical evolution model used in the calculations, and compare its results to the abundances derived from our SED modeling. The results of the paper are briefly summarized in §6.

Throughout this paper we will refer to the solar abundances by Grevesse & Sauval (1998), the oxygen number abundance being $12 + \log(\mathrm{O/H})_\odot = 8.83$, the Helium and heavy elements to gas mass ratios $Y_\odot = 0.248$ and $Z_\odot = 0.017$, respectively. Besides, we assume that the helium abundance is independent of the metallicity.

2. THE SAMPLE OF NEARBY GALAXIES

2.1. Source Selection

In order to properly characterize the PAH emission, we considered galaxies whose mid-IR spectrum has been observed, either with one of the spectrographs onboard the *ISO* satellite, or with the *Spitzer*/IRS. We combined ISO samples of starbursts and AGNs (Laurent et al. 2000), spirals (Roussel et al. 2001), ellipticals (Xilouris et al. 2004), dwarf galaxies (Madden et al. 2006), and the low-metallicity sources of the *Spitzer* sample presented by Engelbracht et al. (2005) which were observed by *Spitzer*/IRS. Among the ellipticals, only NGC 1399 has a mid-IR spectrum. Consequently, our sample includes various types of galaxies and covers a wide range of metallicities and star formation activity (Table 1).

The modeling that will be presented in §3 requires the assembly of data covering the stellar as well as the dust emission components, for each galaxy. First, we need most of the U, B, V, R, I, J, H, K fluxes, to constrain the stellar spectrum shape. Photometric J, H and K bands are available for almost all of our sources, thanks to the 2MASS survey (Jarrett et al. 2003). We rejected the galaxies Arp 118, Arp 236, Arp 299 and NGC 4038, for which no B and V bands were reported. Second, the far-IR SED is used to constrain the intensity of the interstellar radiation field (ISRF). Hence, we rejected galaxies which have not been detected by IRAS or MIPS, such as HS 0822+3542, Tol 1214-277 and Tol 65. In addition, our mass estimates are normalised to the Hydrogen mass. We therefore rejected the galaxy IRAS 23128-5919, for which no H I observation was reported. Finally, we removed M 31 from our sample, since its angular diameter is too large to build a consistent observed total SED.

The global properties of the selected sources are presented in Table 1. If relevant, the distances were homogenised to $H_0 = 71$ km s^{-1} Mpc^{-1}. The masses have been scaled to the adopted distance.

Table 1. Select Properties of the Sample

Name	R.A. (J2000)	Dec. (J2000)	Mid-IR spectrograph	Distance (Mpc)	$12 + \log(\mathrm{O/H})$	[ref.]	$M_{\mathrm{H\,I}}$ ($10^8\ M_\odot$)	[ref.]	$M_{\mathrm{H_2}}$ ($10^8\ M_\odot$)	[ref.]	Notes
Haro 11	$00^h36^m52\overset{s}{.}5$	$-33°33'19''$	*Spitzer*/IRS	92	7.9	[2]	$\lesssim 1^{(?)}$	[2]	$\lesssim 1$	[2]	Pec H II
NGC 253	$00^h47^m32\overset{s}{.}9$	$-25°17'18''$	*ISO*/CAM	3.3	9.0	[3]	18	[4]	17	[5]	H II
NGC 520	$01^h24^m34\overset{s}{.}9$	$+03°47'31''$	*ISO*/CAM	27	(?)		35	[6]	35	[7]	Pec H II
NGC 613	$01^h34^m17\overset{s}{.}5$	$-29°24'58''$	*ISO*/CAM	19	9.2	[8]	37	[9]	$\cdots$		Sy
NGC 891	$02^h22^m33\overset{s}{.}4$	$+42°20'57''$	*ISO*/CAM	9.6	8.9	[10]	76	[9]	49	[9]	Edge-on
NGC 1068	$02^h42^m40\overset{s}{.}6$	$-00°00'47''$	*ISO*/CAM	15	9.0	[11]	22	[12]	74	[13]	Sy
NGC 1097	$02^h46^m19\overset{s}{.}1$	$-30°16'28''$	*ISO*/CAM	12	9.0	[14]	51	[15]	$\gtrsim 7.3$	[16]	Sy
NGC 1140	$02^h54^m33\overset{s}{.}5$	$-10°01'44''$	*ISO*/CAM	25	8.0	[17]	52	[18]	$\cdots$		Irr H II
NGC 1365	$03^h33^m35\overset{s}{.}6$	$-36°08'23''$	*ISO*/CAM	19	9.1	[19]	130	[20]	170	[21]	Sy
SBS 0335-052	$03^h37^m44\overset{s}{.}0$	$-05°02'38''$	*Spitzer*/IRS	54	7.3	[22]	9.9	[23]	$\cdots$		BCD
NGC 1399	$03^h38^m29\overset{s}{.}1$	$-35°27'03''$	*ISO*/CAM	21	(?)		$\lesssim 2$	[9]	$\cdots$		cD
IC 342	$03^h46^m49\overset{s}{.}7$	$+68°05'45''$	*ISO*/CAM	3.8	8.9	[24]	130	[9]	50	[9]	H II
NGC 1569	$04^h30^m49\overset{s}{.}1$	$+64°50'52''$	*ISO*/CAM	2.2	8.2	[25]	1.3	[26]	0.50	[27]	Irr H II
NGC 1808	$05^h07^m42\overset{s}{.}3$	$-37°30'47''$	*ISO*/CAM	11	9.1	[28]	18	[29]	20	[30]	Sy
II Zw 40	$05^h55^m42\overset{s}{.}7$	$+03°23'29''$	*ISO*/CAM	10	8.1	[31]	4.2	[9]	0.23	[9]	BCD
He 2-10	$08^h36^m15\overset{s}{.}2$	$-26°24'34''$	*Spitzer*/IRS	8.7	8.9	[25]	3.1	[32]	1.6	[32]	Irr H II
I Zw 18	$09^h34^m02\overset{s}{.}0$	$+55°14'28''$	*Spitzer*/IRS	13	7.2	[22]	1.2	[33]	$\cdots$		BCD
M 82	$09^h55^m51\overset{s}{.}8$	$+69°40'46''$	*ISO*/CAM	3.6	9.0	[34]	9.0	[35]	13	[36]	Irr H II
NGC 3256	$10^h27^m51\overset{s}{.}1$	$-43°54'17''$	*ISO*/CAM	37	8.9	[37]	62	[38]	300	[39]	Pec H II
Mrk 33	$10^h32^m31\overset{s}{.}9$	$+54°24'04''$	*Spitzer*/IRS	20	8.4	[37]	4.3	[40]	0.70	[41]	Irr H II
Mrk 153	$10^h49^m05\overset{s}{.}0$	$+52°20'08''$	*Spitzer*/IRS	37	7.8	[42]	6.7	[43]	$\cdots$		BCD
VII Zw 403	$11^h27^m59\overset{s}{.}9$	$+78°59'39''$	*Spitzer*/IRS	4.5	7.7	[22]	0.69	[40]	$\cdots$		BCD
UM 448	$11^h42^m12\overset{s}{.}4$	$+00°20'03''$	*Spitzer*/IRS	70	8.0	[44]	47	[45]	24	[45]	Pec H II
NGC 4945	$13^h05^m26\overset{s}{.}2$	$-49°28'15''$	*ISO*/CAM	3.9	(?)		45	[46]	17	[47]	Edge-on Sy
Centaurus A	$13^h25^m28\overset{s}{.}0$	$-43°01'06''$	*ISO*/CAM	3.8	~ 9	[48]	11	[49]	2.0	[50]	Elliptical Sy
M 51	$13^h29^m52\overset{s}{.}7$	$+47°11'43''$	*ISO*/CAM	8.4	8.7	[51]	50	[52]	56	[53]	
M 83	$13^h37^m00\overset{s}{.}7$	$-29°51'58''$	*ISO*/CAM	4.5	9.2	[54]	51	[55]	49	[56]	H II

Table 1—Continued

Name	R.A. (J2000)	Dec. (J2000)	Mid-IR spectrograph	Distance (Mpc)	$12 + \log(\text{O/H})$	[ref.]	$M_{\text{H\,I}}$ ($10^8\ M_\odot$)	[ref.]	M_{H_2} ($10^8\ M_\odot$)	[ref.]	Notes
Tol 89	$14^h01^m21\overset{s}{.}5$	$-33°03'50''$	*Spitzer*/IRS	15	8.0	[57]	13	[58]	$\cdots$		H II
Circinus	$14^h13^m09\overset{s}{.}6$	$-65°20'21''$	*ISO*/CAM	4.0	(?)		55	[46]	11	[59]	Sy
NGC 5253	$13^h39^m55\overset{s}{.}7$	$-31°38'29''$	*ISO*/SWS	3.3	8.2	[17]	0.91	[60]	$\lesssim 0.1$	[61]	Irr H II
Arp 220	$15^h34^m57\overset{s}{.}2$	$+23°30'11''$	*ISO*/CAM	73	(?)		280	[38]	160	[62]	ULIRG
NGC 6240	$16^h52^m58\overset{s}{.}8$	$+02°24'06''$	*ISO*/CAM	98	(?)		88	[9]	310	[9]	LIRG
NGC 6946	$20^h34^m51\overset{s}{.}2$	$+60°09'17''$	*ISO*/CAM	5.5	9.1	[63]	56	[64]	33	[65]	H II
Mrk 930	$23^h31^m58\overset{s}{.}3$	$+28°56'50''$	*Spitzer*/IRS	73	8.1	[44]	28	[66]	$\cdots$		H II
NGC 7714	$23^h36^m14\overset{s}{.}1$	$+02°09'19''$	*Spitzer*/IRS	37	8.5	[67]	17	[68]	22	[68]	Pec H II

References. — [2] Bergvall et al. (2000); [3] Zaritsky et al. (1994); [4] Boomsma et al. (2005); [5] Houghton et al. (1997); [6] Bernloehr (1993); [7] Yun & Hibbard (2001); [8] Alloin et al. (1979); [9] Bettoni et al. (2003); [10] Otte et al. (2001); [11] Dutil & Roy (1999); [12] Staveley-Smith & Davies (1987); [13] Helfer et al. (2003); [14] Storchi-Bergmann et al. (1995); [15] Ondrechen & van der Hulst (1989); [16] Gerin et al. (1988); [17] Heckman et al. (1998); [18] Hunter et al. (1994); [19] Roy & Walsh (1997); [20] Jorsater & van Moorsel (1995); [21] Sandqvist et al. (1995); [22] Izotov et al. (1999); [23] Thuan et al. (1999); [24] Pilyugin et al. (2004); [25] Kobulnicky & Skillman (1997); [26] Stil & Israel (2002); [27] Israel (1997); [28] Ravindranath & Prabhu (2001); [29] Dahlem et al. (2001); [30] Dahlem et al. (1990); [31] Pérez-Montero & Díaz (2003); [32] Sauvage et al. (1997); [33] van Zee et al. (1998); [34] Boselli et al. (2002); [35] Appleton et al. (1981); [36] Walter et al. (2002); [37] Mas-Hesse & Kunth (1999); [38] Casasola et al. (2004); [39] Sargent et al. (1989); [40] Thuan et al. (2004); [41] Israel (2005); [42] Kunth & Joubert (1985); [43] Thuan & Martin (1981); [44] Izotov & Thuan (1998); [45] Sage et al. (1992); [46] Huchtmeier & Richter (1988); [47] Dahlem et al. (1993); [48] Schaerer et al. (2000); [49] Richter et al. (1994); [50] Wild et al. (1997); [51] Bresolin et al. (2004); [52] Dean & Davies (1975); [53] Helfer et al. (2003); [54] Webster & Smith (1983); [55] Tilanus & Allen (1993); [56] Lundgren et al. (2004); [57] Durret et al. (1985); [58] Paturel et al. (2003); [59] Elmouttie et al. (1998); [60] Reif et al. (1982); [61] Meier et al. (2002); [62] Sanders et al. (1991); [63] Kobulnicky et al. (1999); [64] Carignan et al. (1990); [65] Tacconi & Young (1986); [66] Hopkins et al.

(2002); [67] Gonzalez-Delgado et al. (1995); [68] Struck & Smith (2003).

Note. — The sources are ordered according to their right ascension. The symbol $^{(?)}$ identifies uncertain values. Entries for the metallicity for which no data exist are marked by $\cdots$, and assumed to be solar-to-supersolar. The H_2 masses are not used to calculate the dust-to-gas mass ratio, because the IR emission was assumed to originate entirely from the H I gas.

2.2. *ISO*/CAM Data Reduction

Most of the sources in Table 1 were observed with *ISO*/CAM (Cesarsky et al. 1996) on board the *ISO* satellite (Kessler et al. 1996). These spectra were used by Madden et al. (2006), and we refer to this work for a detailed description of the data reduction. The CVF performed spectral imaging using a 32×32 detector array, with a sampling of $3''\text{pixel}^{-1}$ or $6''\text{pixel}^{-1}$ in our cases, from $\lambda = 5$ μm to 16.5 μm with one pointing of two CVFs, from $\lambda = 5$ to 9.5 μm and from $\lambda = 9.0$ to 16.5 μm. The spectral resolution goes from $\lambda/\Delta\lambda = 35$ to 51 across the full spectra.

For the data treatment, we used the CAM Interactive Reduction (CIR, version AUG01; Chanial 2003). The subtraction of the dark currents was performed using the Biviano et al. (1998) model which predicts the time evolution for each row of the detector, taking into account drifts along each orbit and each revolution. We masked the glitches using multi-resolution median filtering (Starck et al. 1999) on each block of data after slicing the cube. Additional deglitching was performed manually, examining the temporal cut for each pixel. We corrected the systematic memory effects using the Fouks-Schubert method (Coulais & Abergel 2000). We computed a hybrid flat-field image placing a mask on the source and computing a flat field outside this mask from the median of the temporal cut for each pixel. For the pixels which were on-source, the flat-field response was set to the corresponding calibration flat-field. The conversion from Analog Digital Units to mJy/pixel was performed using the standard in-flight calibration data base. To remove the sky contribution, the sources smaller than the array were masked and, for a given wavelength, the median of the pixels which are off-source were subtracted from each pixel. For the more extended sources, we subtracted an independently observed zodiacal spectrum. The intensity of this spectrum was a free parameter varied in order to match the properly sky subtracted fluxes in the LW2 (6.7 μm) and LW3 (14.3 μm) broadbands. The final product is a 3D spectral-image of each galaxy. We integrated the spectrum into an aperture encompassing the entire galaxy, and to obtain the global SED of the galaxy. When the angular size of the source was larger than the one of the array, we scaled-up the spectrum to match the $IRAS_{12\mu m}$ broadband flux.

2.3. *Spitzer*/IRS Spectrum Extraction

Several of the low-metallicity sources in Table 1 were not observed by *ISO*/CAM, we therefore complemented our database with publically released mid-IR spectra from the *Spitzer*/IRS spectrometer on board the *Spitzer Space Telescope* (Houck et al. 2004b; Werner et al. 2004). Among these galaxies, the spectra of SBS 0335-052, NGC 7714, VII Zw 403, Haro 11 and I Zw 18 are described in details in Houck et al. (2004a), Brandl et al. (2004) and

Wu et al. (2006). We considered only low-resolution data, taken with the SL (Short-Low) module, from $\lambda = 5.2$ μm to 14.5 μm, and the LL (Long-Low) module, from $\lambda = 14.0$ μm to 38.0 μm, both with a spectral resolution of $\lambda/\Delta\lambda \simeq 64 - 128$.

We retrieved the Basic Calibrated Data (BCD) that have been preprocessed by the Spitzer Science Center (SSC) data reduction pipeline, and converted to flux density, corrected for stray light and flatfielded. The extraction of the spectra from the 2D space/wavelength images was performed with the Spectral Modeling, Analysis and Reduction Tool (SMART, version 5.5.6; Higdon et al. 2004). We first inspected the BCD images and identified the hot pixels which have not been masked out by the SSC. We replaced them by the median of their neighbors. For each module, an off-source position is observed. We subtracted this spectrum from the on-source one, in order to remove the sky emission. The extraction of the 1D spectrum was performed inside a column whose width vary with the wavelength. We have excluded the bonus order. Then, the various frames, for each nod position, were coadded. Since the long wavelength end of the SL module and the short wavelength end of the LL one were not systematically overlapping, we finally scaled the SL module, in order to obtain a continuous spectrum. This scaling factor can be as large as 50%. At the time when this publication is written, the *Spitzer*/IRS data handbook recommends not to derive the signal-to-noise ratio from the uncertainties generated by the pipeline. Instead of that, we adopted the recommended systematic error of 20%. However, the SL module of the noisiest spectra (VII Zw 403, Mrk 153, Mrk 930, I Zw 18, Tol 89) exhibits fluctuations larger than this value. To take into account these statistical variations, we smoothed these spectra into a $\Delta\lambda \simeq 0.2$ μm window (4 points), and took the standard deviation inside this window as the error. Similarly to what we did with *ISO*/CAM spectra (§2.2), in order to compensate the fact that we may be overlooking some extended emission, we scaled-up the *Spitzer*/IRS SL and LL spectra to match the $IRAS_{12\mu m}$ and $IRAS_{25\mu m}$. In the case of II Zw 40, the *Spitzer*/IRS spectrum does not exhibit the PAH features that Madden et al. (2006) detected in the extended emission, thus we prefer to use the *ISO*/CAM data for this galaxy. For Tol 89, the *Spitzer*/IRAC$_{8\mu m}$ broadband flux is higher than the integrated spectrum into the same band. This is probably due to the fact that the slit of *Spitzer*/IRS measures only the nucleus emission, which likely has a steeper continuum and weaker features than the extended emission contributing to the total broadband. Therefore, we will consider the mass of PAHs derived for this galaxy to be a lower limit.

2.4. The Multiwavelength SEDs

The UV-to-radio SED of each galaxy was built using data from different catalogs. We extensively used the HYPERLEDA and NED databases. Most of the SEDs include *IRAS* broadband fluxes at 12, 25, 60 and 100 μm (Moshir & et al. 1990; Rice et al. 1988), and J, H, K 2MASS fluxes (Jarrett et al. 2003). For some of the galaxies, we completed the IR SED with the broadband *Spitzer* data reported by Dale et al. (2005). We kept only data encompassing the entire galaxy. The optical data were corrected for Galactic extinction, using the Schlegel et al. (1998) extinction maps.

For NGC 5253, we used the *ISO*/SWS observations of Crowther et al. (1999) to model the spectrum of this galaxy.

3. MODELING THE PANCHROMATIC SEDS OF GALAXIES TO DERIVE THE PAH AND DUST ABUNDANCES

3.1. Motivations and Approach

Determining the PAH abundance from the 8 and 24 μm fluxes or even from the mid-IR spectrum requires: *(i)* knowledge of the contribution of other dust species to the mid-IR emission, in order to determine the intrinsic emission in the PAH bands; and *(ii)* knowledge of the ISRF they are subjected to, since PAHs are stochastically heated. The dust that contributes to the mid-IR emission is hot dust radiating at equilibrium temperature in H II regions, as well as very small grains undergoing temperature fluctuations in PDRs. Therefore, determining the PAH abundance requires a panchromatic approach, to model the SEDs of galaxies. It requires knowledge of star formation history, and processing of the stellar SED by the gas and dust in the ionized and neutral phases of the galaxy.

The 8/24 μm flux ratio provides information on the strength of the PAH features in the galaxy, although it is relatively limited. In general, the *Spitzer*/IRAC$_{8\mu m}$ flux is dominated by the $6 - 9$ μm PAH features, but in some cases, such as low metallicity galaxies or deeply embedded sources, the 8 μm flux may be dominated by, respectively, the continuum (Madden et al. 2006; Wu et al. 2006) or the 9.7 μm silicate feature (e.g. Spoon et al. 2004; Hao et al. 2007). When there are no PAHs and the *Spitzer*/IRAC$_{8\mu m}$ band is dominated by the continuum, the 8/24 μm ratio reflects the color of the mid-IR emitting silicates and graphites. The *Spitzer*/MIPS$_{24\mu m}$ flux is dominated by the continuum emission from the silicate and carbon grains. However, this part of the SED is very sensitive to the abundance of small grains (e.g. Galliano et al. 2003, 2005), and can originate additionally from large

grains close to strong sources of radiation (e.g. Plante & Sauvage 2002; Vanzi & Sauvage 2004).

Fig. 1 shows the ratio of the two bands, for the sources presented in Table 1. The figure shows that when the PAH-to-continuum ratio is small, the $8/24$ μm ratio plateaus around a value of $\simeq 0.1$, which roughly represents the color of the mid-IR continuum. The figure illustrates that the separation between the PAH bands and the continuum is important to study the evolution of their strengths with the metallicity. The error bars on the ratio, in Fig. 1, come from the propagation of the observational errors. The error bars on the metallicity were not systematically given by the authors who published them. An error of 0.1 dex in the O/H number abundance accounts for the typical dispersion between independent measurements. There were 6 sources, in Table 1, for which no metallicity measurements were reported. However, all of them have the morphology, optical colors, IR emission and H_2 content of solar or supersolar systems, with NGC 1399 probably having the largest metallicity. We assign an arbitrary $Z = (2 \pm 1)\, Z_\odot$ to these galaxies, and consider them to be uncertain.

Knowledge of the shape of the ISRF to determine the PAH abundance is important, since the absorption properties of PAHs are significantly different from the ones of solid-state grains (carbonaceous or silicates) believed to be the carriers of the mid-IR continuum. Fig. 2 shows the different wavelength-dependence of the mass absorption coefficient, $\kappa_{\rm abs}$, of various types of grains. It shows that the value of $\kappa_{\rm abs}$ for PAHs drops by 4 orders of magnitude between 0.1 and 1 μm, where the stars emit most of their energy, while the $\kappa_{\rm abs}$ of graphite and silicate dust drop by less than 2 orders of magnitude. However, most of the energy is absorbed at shorter wavelengths. Thus, the PAHs are more sensitive to very young stellar populations than the grains responsible for the 24 μm continuum (Fig. 3), and a correct determination of their excitation rate should take into account this property.

3.2. The Contribution of H II Regions to the SED of a Galaxy

Models of the spatial distribution of the dust in our Galaxy indicate that H II regions dominate the infrared SED up to wavelengths of $\sim$ 60 μm (Sodroski et al. 1997; Paladini et al. 2007). In principle, the contribution of H II regions could be derived from any tracer of the recombination rate, like the radio free-free continuum. However, the free-free-to-IR ratio depends significantly on the density and dust-to-gas mass ratio in the H II region (e.g. Petrosian et al. 1972; Mezger et al. 1974), requiring detailed modeling of H II regions as a function of these parameters.
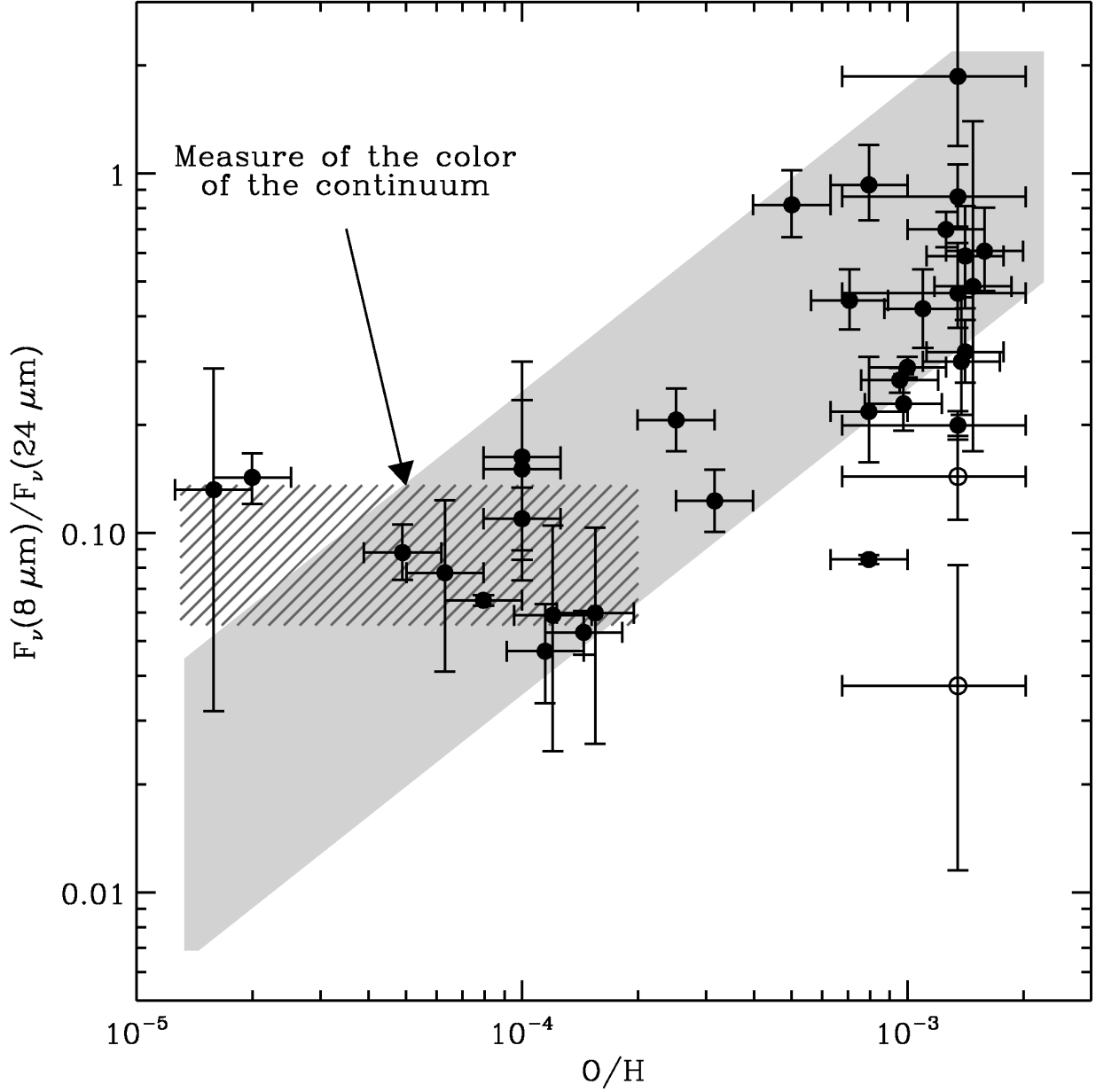
Fig. 1.— Mid-IR color as a function of the oxygen number abundance, for the sample in Table 1. This figure illustrates the importance of knowing the mid-IR continuum emission in order to derive the intensity of the PAH bands. Our observed SEDs have been integrated over the $Spitzer$/IRAC$_{8\mu m}$ and $Spitzer$/MIPS$_{24\mu m}$ bandpasses, in order to produce this plot. The two open circles are the (U)LIRGs of our sample. The grey stripe is the $\pm 1\sigma$ linear correlation between $\log(\mathrm{O/H})$ and $\log\left(F_\nu(8\ \mu\mathrm{m})/F_\nu(24\ \mu\mathrm{m})\right)$. The hatched stripe shows the range of the ratio $(0.06 \lesssim F_\nu(8\ \mu\mathrm{m})/F_\nu(24\ \mu\mathrm{m}) \lesssim 0.13)$, which is a measure of the color of the silicate and graphite continuum, when the PAH features are weak.
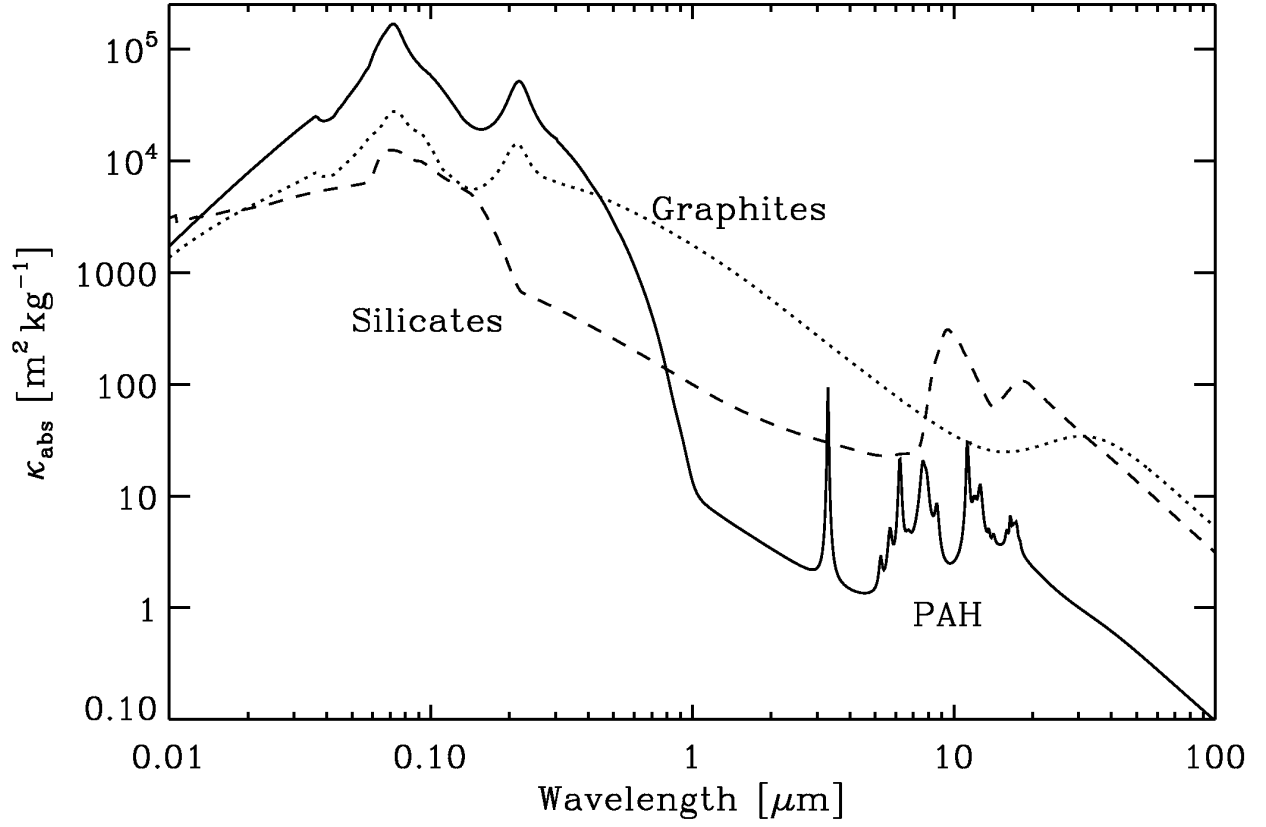
Fig. 2.— The wavelength-dependence of the mass absorption coefficient of the PAHs (Draine & Li 2007), graphites (Laor & Draine 1993) and silicates (Weingartner & Draine 2001), integrated over the Zubko et al. (2004) size distribution, for the bare grain model with solar abundance constraints (BARE-GR-S).
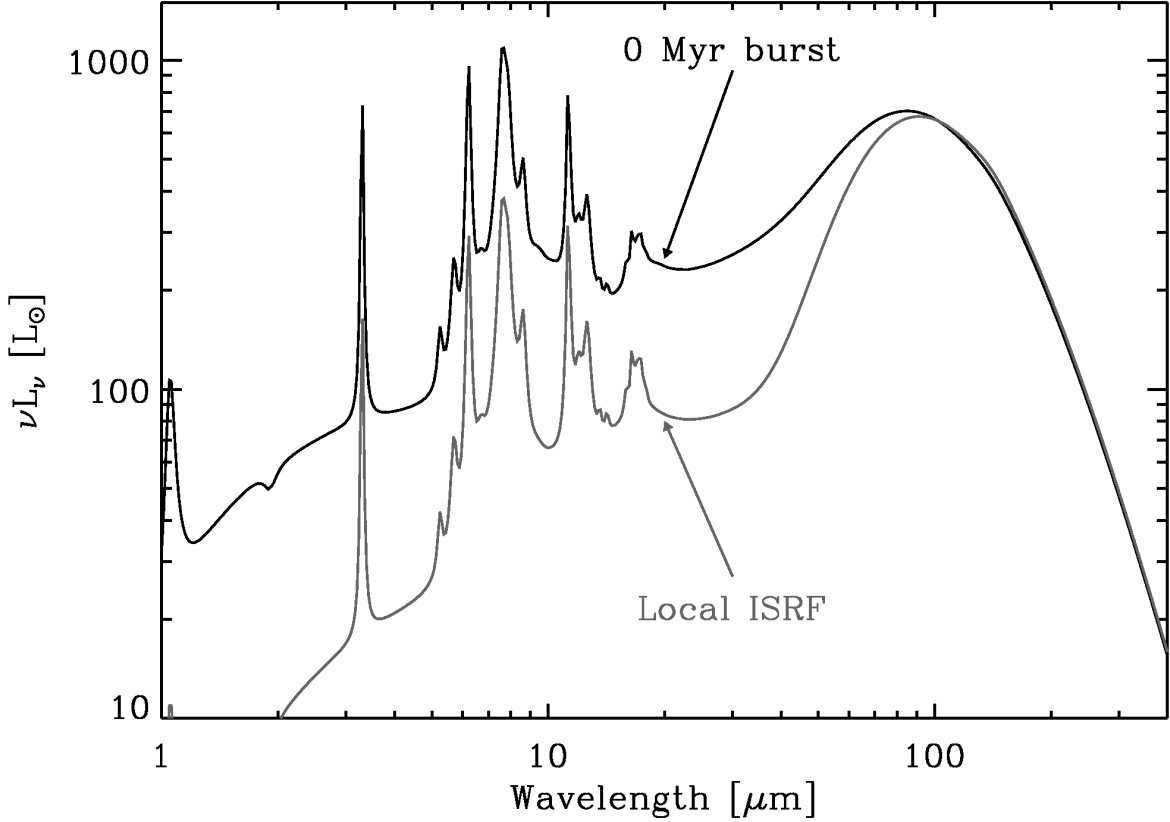
Fig. 3.— Sensitivity of the mid-IR SED to the age of the stellar populations. The two SEDs come from the same grain populations (abundances and size distribution; Zubko et al. 2004); the only difference is the shape and intensity of the interstellar radiation field they are experiencing. The black SED is heated by a young UV-rich instantaneous burst, while the grey one is the subjected to the local ISRF. It shows that for a given far-IR spectrum, the PAH emission can vary by a factor of $\simeq 3$ depending on the shape of the ISRF, therefore affecting the estimate of the PAH abundance by the same amount.

We consider H II regions to be made of a central ionizing star, surrounded by PAH-free dusty ionized gas. The output of an individual H II region therefore consists of: *(i)* escaping non-ionizing stellar radiation; *(ii)* IR emission from the reprocessing of the stellar emission by dust; and *(iii)* radio free-free emission from the reprocessing of ionizing photons by the gas. We created a library of H II region spectra for stars of different spectral types, embedded into a gas of different densities and dust-to-gas mass ratios. The total contribution of H II regions to a galaxy's SED is derived by integrating the spectra of indvidual H II regions over the stellar initial mass function (IMF).

There are several simplifying assumptions in our procedure. Individual H II regions are considered to be spherical, homogeneous, consisting of pure Hydrogen. In calculating the infrared emission, we neglected scattering of stellar radiation by the dust. We assumed that all the dust radiates at equilibrium dust temperature, and that PAH are destroyed and therefore absent into the H II region itself. In calculating the emission from the ensemble of H II regions, we assumed that they are not clustered, so that the total radiation is an IMF weighted sum over all spectral types, assumed to be surrounded by gas with the same density.

The theoretical evolution of the SED of H II regions and their surrounding molecular material has been extensively discussed by Bressan et al. (2002), Panuzzo et al. (2003) and Dopita et al. (2005, 2006a,b). In these studies, the spectrum of an H II region depends on its evolutionary state, controlled by its age, density and the dissipation time scale of the surrounding molecular clouds. In comparison, our approach is more flexible and empirical, in which the parameters can vary more freely instead of being constrained by evolutionary models.

In the following, we describe how we derive the SED of H II regions. The definition of each mathematical variable is summarised in Table 2.

Table 2. Mathematical Variables Used Throughout the Paper.

Name	Units	Definition
		General Variables
ν	Hz	Frequency of the radiation
λ	μm	Wavelength of the radiation
M_{gas}	$M_\odot$	Gas mass (Hydrogen, Helium and metals) of the region or galaxy
M_{dust}	$M_\odot$	Dust mass of the region or galaxy
$Z_{\mathrm{dust}} = M_{\mathrm{dust}}/M_{\mathrm{gas}}$		Dust-to-gas mass ratio
Z_{gas}		Metal mass fraction in the gas phase (or metallicity)
$m_{\mathrm{H}} = 1.67 \times 10^{-24}$	g	Mass of a single H atom
m_{dust}	g	Average mass of a dust grain
a	μm	Grain radius
$f(a)$	grain μm^{-1}	Grain size distribution, normalized to unity
$Q_{\mathrm{abs}}(a,\nu)$		Absorption efficiency of a grain of radius a
$\sigma_{\mathrm{dust}}(\nu) = \int_0^\infty \pi a^2 Q_{\mathrm{abs}}(a,\nu)\, f(a)\, \mathrm{d}a$	cm^2 grain^{-1}	Average dust cross-section per grain
m	$M_\odot$	Mass of individual stars
$\phi(m)$	$M_\odot^{-1}$	Initial mass function
		H II Region Variables (§3.2)
$\nu_1 = 3.29 \times 10^{15}$	Hz	Frequency of the Lyman break
R_s	cm	Radius of the equivalent dust-free Strömgren sphere of a single H II region
$y = r/R_s$		Radial coordinate normalised to R_s
n_{H}	H cm^{-3}	Number of H atoms (or protons) per unit volume
n_{dust}	grain cm^{-3}	Number of dust particles per unit volume

Table 2—Continued

Name	Units	Definition
$n_e(y)$	$e\,\mathrm{cm}^{-3}$	Number of electrons per unit volume
$x(y) = n_e/n_{\mathrm{H}}$		Ionization fraction of Hydrogen
$\sigma_{\mathrm{H}}(\nu)$	$\mathrm{cm}^2\,\mathrm{H}^{-1}$	Ionization cross-section of Hydrogen (Eq. 2.4 of Spitzer 1978)
T_e	K	Electron temperature
T_{dust}	K	Equilibrium dust temperature
$L_\nu(\nu, y)$	$L_\odot\,\mathrm{Hz}^{-1}$	Total monochromatic luminosity, passing through the shell of radius y
$L_\nu^{\mathrm{OB}}(\nu)$	$L_\odot\,\mathrm{Hz}^{-1}$	Intrinsic monochromatic luminosity emitted by the central star, given by Panagia (1973)
$L_{\mathrm{B}}(y)$	$L_\odot$	Luminosity of the case B recombination lines at a radius y
$L_\nu^{\mathrm{dust}}(\nu, y)$	$L_\odot\,\mathrm{Hz}^{-1}$	Monchromatic luminosity reprocessed by the dust at a radius y
$L_\nu^{ff}(\nu, y)$	$L_\odot\,\mathrm{Hz}^{-1}$	Monchromatic luminosity of the free-free cooling at a radius y (Eq. 3.54 of Spitzer 1978)
$\alpha_{\mathrm{A}}(T_e)$	$\mathrm{cm}^3\,\mathrm{s}^{-1}$	Case A recombination coefficient (Table 2.1 of Osterbrock 1989)
$\alpha_{\mathrm{B}}(T_e)$	$\mathrm{cm}^3\,\mathrm{s}^{-1}$	Case B recombination coefficient (Table 2.1 of Osterbrock 1989)
$L_\nu^{\mathrm{H\,II}}(\nu, m, Z_{\mathrm{dust}}, n_{\mathrm{H}})$	$L_\odot\,\mathrm{Hz}^{-1}$	Monochromatic luminosity of an individual H II region
t_{burt}	Myr	Age of the burst of star formation
$L_\nu^{\mathrm{burst}}(\nu, t_{\mathrm{burst}}, Z_{\mathrm{dust}}, n_{\mathrm{H}})$	$L_\odot\,\mathrm{Hz}^{-1}$	Monocromatic luminosity of a distribution of H II regions

Global SED Variables (§3.3)		
t_{SF}	Myr	Age of the galaxy
$M_\star$	$M_\odot$	Mass of the non-ionizing stars
f_{sync}		Ratio between the synchrotron and the free-free at $\lambda = 1$ cm
M_{dust}	$M_\odot$	Dust mass in the PDRs
$f_{\mathrm{PAH}} = M_{\mathrm{PAH}}/M_{\mathrm{dust}}$		PAH mass fraction
$f_+ = M_{\mathrm{PAH}^+}/M_{\mathrm{PAH}}$		Fraction of ionized PAHs
L_i	$L_\odot$	Luminosity of a mid-IR ionic line

Table 2—Continued

Name	Units	Definition
$U_\nu(\nu)$	$\mathrm{erg\,s^{-1}\,cm^{-3}\,Hz^{-1}}$	Monochromatic radiation density in the PDRs
$U = \displaystyle\int_0^\infty U_\nu(\nu)\,\mathrm{d}\nu$	$\mathrm{erg\,s^{-1}\,cm^{-3}}$	Integrated radiation density in the PDRs
$L_\nu^\star(\nu, t_{\mathrm{SF}}, M_\star)$	$L_\odot\,\mathrm{Hz^{-1}}$	Monochromatic luminosity emitted by the non-ionizing stars
$L_\nu^{\mathrm{sync}}(\nu, f_{\mathrm{sync}})$	$L_\odot\,\mathrm{Hz^{-1}}$	Monochromatic luminosity of the synchrotron radiation
$L_\nu^{\mathrm{Zub}}(\nu, U, M_{\mathrm{dust}}, f_{\mathrm{PAH}}, f_+)$	$L_\odot\,\mathrm{Hz^{-1}}$	Monochromatic luminosity emitted by the dust in a given U
$L_\nu^{\mathrm{PDR}}(\nu, \alpha, U_-, U_+, M_{\mathrm{dust}}, f_{\mathrm{PAH}}, f_+)$	$L_\odot\,\mathrm{Hz^{-1}}$	Monochromatic luminosity emitted by the dust in PDRs
$P_e^{\mathrm{H\,II}}(\nu, A_V^{\mathrm{H\,II}})$		Escaping fraction of the H II region photons
$P_e^{\mathrm{PDR}}(\nu, A_V^{\mathrm{PDR}})$		Escaping fraction of the PDR photons
$L_{\mathrm{burst}} = \displaystyle\int_0^\infty L_\nu^{\mathrm{burst}}\,\mathrm{d}\nu$	$L_\odot$	Intrinsic luminosity radiated by the H II regions
$\langle P_e L_{\mathrm{burst}} \rangle = \displaystyle\int_0^\infty P_e^{\mathrm{H\,II}} L_\nu^{\mathrm{burst}}\,\mathrm{d}\nu$	$L_\odot$	Escaping luminosity from the H II regions
$L_{\mathrm{PDR}} = \displaystyle\int_0^\infty L_\nu^{\mathrm{PDR}}\,\mathrm{d}\nu$	$L_\odot$	Luminosity radiated by the dust in the PDRs
$\langle P_e L_{\mathrm{PDR}} \rangle = \displaystyle\int_0^\infty P_e^{\mathrm{PDR}} L_\nu^{\mathrm{PDR}}\,\mathrm{d}\nu$	$L_\odot$	Escaping luminosity from the PDRs
$L_\star = \displaystyle\int_0^\infty L_\nu^\star\,\mathrm{d}\nu$	$L_\odot$	Intrinsic luminosity radiated by the non-ionizing stars
$\langle P_e L_\star \rangle = \displaystyle\int_0^\infty P_e^{\mathrm{PDR}} L_\nu^\star\,\mathrm{d}\nu$	$L_\odot$	Escaping luminosity from the non-ionizing stars

Elemental and Dust Evolution Variables (§5)		
$\Sigma_{\mathrm{gas}}(t)$	$M_\odot\,\mathrm{pc^{-2}}$	Gas mass surface density
Σ_{gas}^0	$M_\odot\,\mathrm{pc^{-2}}$	Initial gas mass surface density
$\Sigma_{\mathrm{SFR}}(t)$	$M_\odot\,\mathrm{yr^{-1}\,pc^{-2}}$	Star formation rate surface density
Z_{ISM}		Total metal mass fraction (gas and dust) in the ISM
$\tau(m)$	Myr	Lifetime of a star of mass m
$m_{\mathrm{ej}}(t)$	$M_\odot$	Mass of gas ejected by a star of mass m, after a time $\tau(m)$
$Y_Z(m)$	$M_\odot$	Mass of metals ejected by a star of mass m, after a time $\tau(m)$
$\mu_{\mathrm{gas}}(t) = \Sigma_{\mathrm{gas}}(t)/\Sigma_{\mathrm{gas}}^0$		Reduced gas mass of the system

3.2.1. The Modeling of Individual H II Regions

We assume that PAHs are totally depleted inside the ionized gas phase (the actual H II region), and that their mass fraction is constant outside of these regions, inside the photodissociation regions. Furthermore, we assume that the H II regions are homogeneous, spherical, and that they contain only Hydrogen and dust. The dust-free Strömgren radius R_s (e.g. Spitzer 1978; Osterbrock 1989) of such a region is defined by the balance between the rate of ionizing photons emitted by the central star and by the electrons recombining to the ground level, and the rate of recombinations to any level higher than the fundamental state:

$$\frac{4\pi}{3} R_s^3 n_{\rm H}^2 \alpha_{\rm B}(T_e) = \int_{\nu_1}^{\infty} \frac{L_\nu^{\rm OB}(\nu)}{h\nu} \, {\rm d}\nu. \tag{1}$$

We use this quantity to normalize the radial coordinate r to the dimensionless radius $y = r/R_s$. In each shell of radius y and thickness ${\rm d}y$, the Hydrogen optical depth is given by:

$$\mathrm{d}\tau_{\rm H}(\nu, y) = [1 - x(y)] \, n_{\rm H} \, R_s \times \sigma_{\rm H}(\nu) \, \mathrm{d}y, \tag{2}$$

the dust optical depth is:

$$\mathrm{d}\tau_{\rm dust}(\nu, y) = n_{\rm dust}(y) \, R_s \times \sigma_{\rm dust}(\nu) \, \mathrm{d}y, \tag{3}$$

and the volume of the shell is ${\rm d}V(y) = 4\pi \, R_s^3 \, y^2 \, {\rm d}y$. We solve the radiative transfer equation, from the central star to the photoionization front:

$$\frac{\mathrm{d}L_\nu(\nu, y)}{\mathrm{d}y} = -L_\nu(\nu, y) \times \left(\frac{\mathrm{d}\tau_{\rm H}(\nu, y)}{\mathrm{d}y} + \frac{\mathrm{d}\tau_{\rm dust}(\nu, y)}{\mathrm{d}y} \right) + \frac{\mathrm{d}L_\nu^{\rm dust}(\nu, y)}{\mathrm{d}y} + \frac{\mathrm{d}L_\nu^{ff}(\nu, y)}{\mathrm{d}y}, \tag{4}$$

together with the photoionization equilibrium in each shell:

$$\alpha_{\rm A}(T_e) \, x(y)^2 n_{\rm H}^2 \, \mathrm{d}V(y) \times h\nu_1 = \int_{\nu_1}^{\infty} L_\nu(\nu, y) \, \mathrm{d}\tau_{\rm H}(\nu, y) \, \mathrm{d}\nu. \tag{5}$$

Eq. (5) gives the value of $x(y)$.

We assume that all the case B recombination lines are resonantly scattered by the gas and are finally absorbed locally by the dust. Therefore the dust is heated both by the stellar continuum and these recombination lines:

$$\int_0^{\infty} \frac{\mathrm{d}\tau_{\rm dust}(\nu, y)}{\mathrm{d}y} L_\nu(\nu, y) \, \mathrm{d}\nu + L_{\rm B}(y) = n_{\rm dust} \frac{\mathrm{d}V}{\mathrm{d}y}(y) \int_0^{\infty} \sigma_{\rm dust}(\nu) \, 4\pi B_\nu(\nu, T_{\rm dust}) \, \mathrm{d}\nu. \tag{6}$$

In Eq. (6), we assume that the dust is at thermal equilibrium with the radiation field. Very small grains may still undergo temperature fluctuations, but since their size distribution is

Table 2—Continued

Name	Units	Definition
$\tau_{\mathrm{dust}}(t)$	Myr	Dust lifetime
$\langle m_{\mathrm{ISM}} \rangle$	$M_{\odot}$	Average gas mass swept-up by a single SN II

poorly known, we neglect this effect in calculating the IR emission. This will lead to an underestimate of the $\sim 1 - 20~\mu$m continuum. We will discuss in §3.3 an empirical way to compensate this underestimation.

Finally, we take into account the fact that dust sublimates in the center of H II regions (e.g. Inoue 2002), by considering that each shell where the equilibrium temperature of the dust exceeds its sublimation temperature is free of this dust specie. We adopt sublimation temperatures of 2500 K and 1800 K for graphite and silicate, respectively (Kruegel 2003).

We solved Eqs. (4) and (5) for stars of masses 8 $M_\odot < m < 100~M_\odot$, with a grid of densities ranging from $n_H = 1~\mathrm{cm}^{-3}$ to $n_H = 3 \times 10^4~\mathrm{cm}^{-3}$, and a grid of dust-to-gas mass ratios ranging from $Z_{\mathrm{dust}} = 1/120$ (Galactic value; Zubko et al. 2004) to $Z_{\mathrm{dust}} = 1/12000$.

3.2.2. The Total Contribution of H II Regions

At the scale of a galaxy, the SED of the ionized gas phase is the combination of several H II regions. We assume that all the H II regions of a given galaxy have the same density, and the same dust-to-gas mass ratio. We adopt a Salpeter initial mass function:

$$\phi(m) \propto m^{-2.35} \qquad \text{for} \qquad m_- < m < m_+ \qquad (7)$$

$$\text{normalised to} \quad \int_{m_-}^{m_+} \phi(m)~\mathrm{d}m = 1$$

$$\text{with} \qquad \begin{cases} m_- & = & 0.1~M_\odot \\ m_+ & = & 100~M_\odot \end{cases}$$

The total SED of an ensemble of H II regions is then given by:

$$L_\nu^{\mathrm{burst}}(\nu, t_{\mathrm{burst}}, Z_{\mathrm{dust}}, n_H) = \int_{m_-}^{m_+(t_{\mathrm{burst}})} L_\nu^{\mathrm{H\,II}}(\nu, m, Z_{\mathrm{dust}}, n_H) \times \phi(m)~\mathrm{d}m. \qquad (8)$$

The upper mass decreases with the age of the burst of star formation. Fig. 4 shows several of these SEDs.

In our case, the age of the H II region does not have an important effect on the shape of the H II SED. Indeed, the age affects essentially the ionizing-to-non-ionizing photon rate. Since our H II SEDs are integrated only out to the photoionization front, the ionizing photons dominate the total power input. Therefore, in what follows, we will consider H II SEDs with an age of 4 Myr.
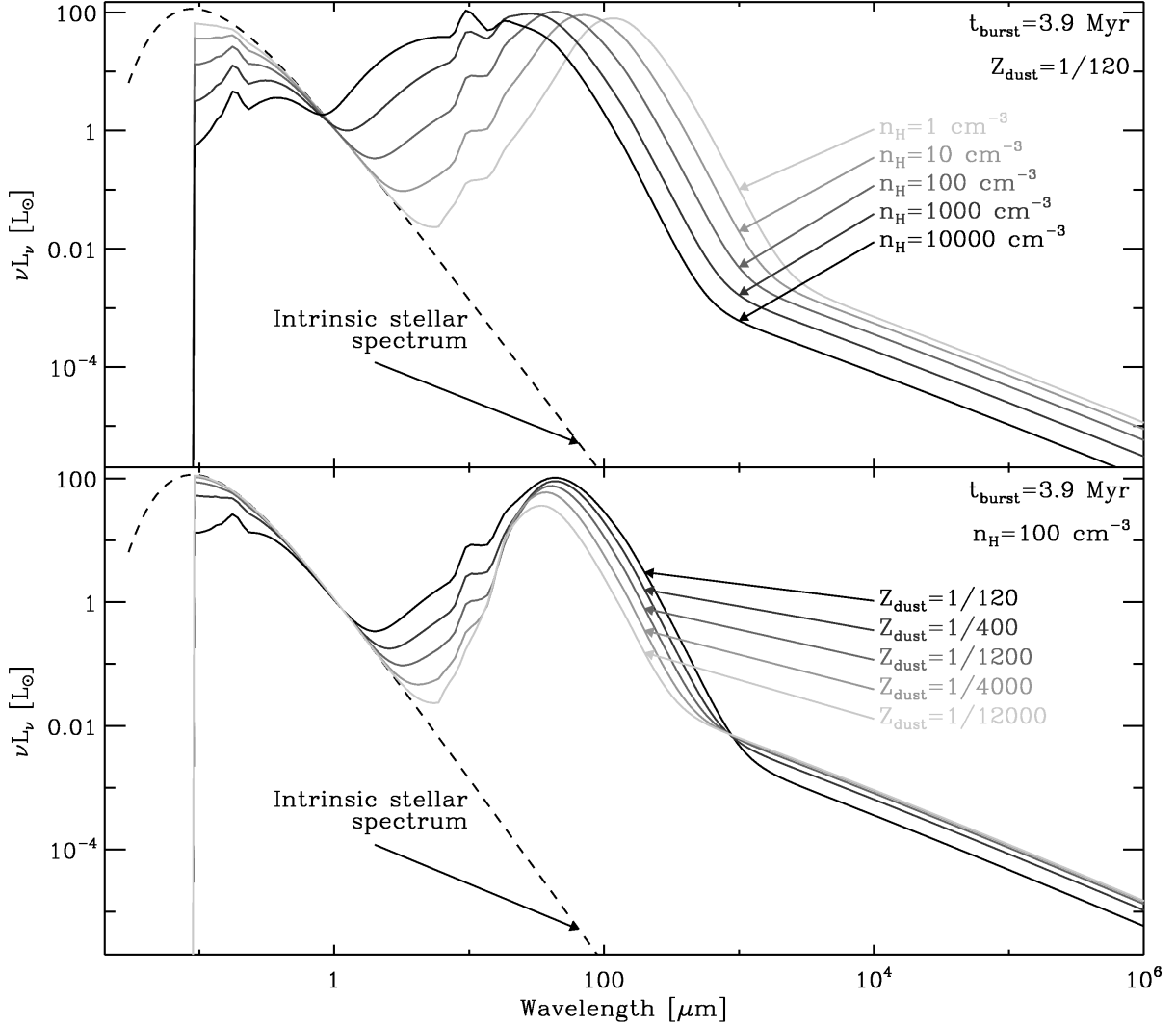
Fig. 4.— SED of an ensemble of H II regions (Eq. 8): for a given age and dust-to-gas mass ratio, varying the density (top panel); and for a given age and density, varying the dust-to-gas mass ratio (bottom panel). The density tends to increase the dust temperature, as well as the free-free-to-IR ratio (top panel). Indeed, when the density is high, the dust absorbs directly a significant fraction of the ionizing photons. Inversely, when Z_{dust} drops, more ionizing photons are absorbed by the gas. The free-free-to-IR ratio is then higher, and the dust luminosity lower (bottom panel).

3.3. The Inclusion of Emission from PDRs and the Resulting Galactic SEDs

3.3.1. The Building Blocks
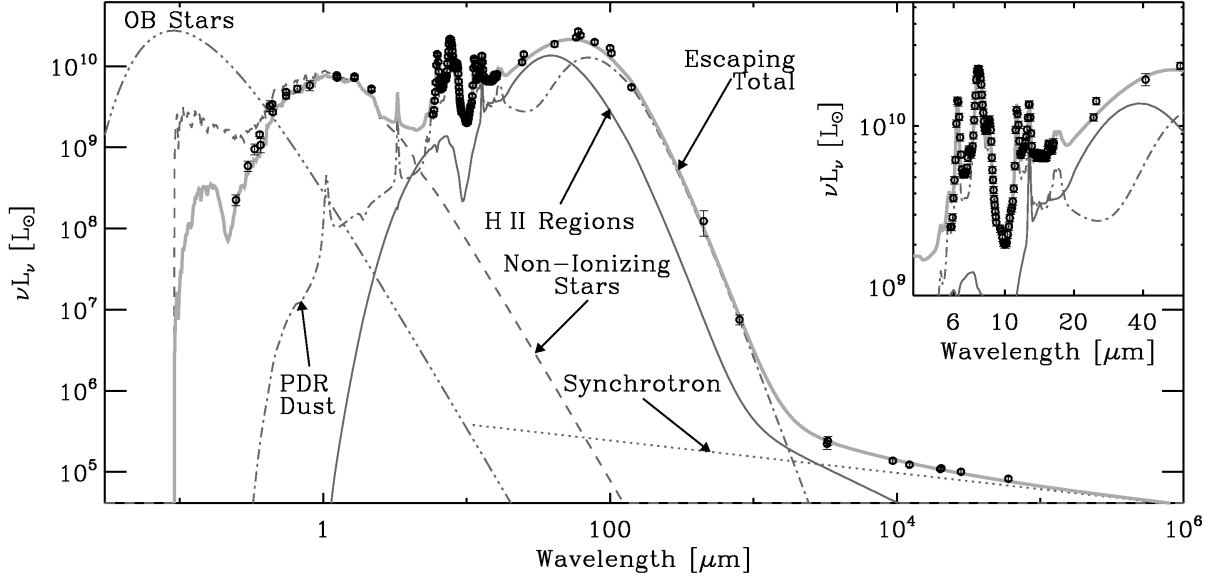
Fig. 5.— Demonstration of the panchromatic SED model applied on a galaxy.

A significant fraction of the radiation escaping from H II regions is absorbed by the dust in the surrounding molecular clouds, as well as in the diffuse ISM. These dense and diffuse PDR components are also heated by the ambient non-ionizing radiation field. Technically, all the parameters of our model are adjusted simultaneously. However, for clarity, we can decompose the procedure in the following steps:

1. Observations of at least two data points sampling the radio continuum constrain the synchrotron-to-free-free ratio. The synchrotron emission is $L_\nu^{\mathrm{sync}} \propto \nu^{-0.8}$.

2. The resulting free-free continuum, together with observations of the mid-IR continuum between ~ 5 and ~ 60 μm are used to constrain the parameters of the H II regions. We use the H II templates presented in §3.2, attenuated with a slab extinction $P_e^{\mathrm{H\,II}}(\nu) = \exp\left[-\tau_{\mathrm{dust}}(\nu)\right]$, to account for absorption by intervening dust to the H II region. The power absorbed, $L_{\mathrm{burst}} - \langle P_e L_{\mathrm{burst}} \rangle$, contributes to the heating of the dust in PDRs. As mentioned in §3.2, we have not taken into account the emission from stochastically heated grains in this phase. To correct empirically for this effect, we redistribute a part of the H II dust power into the sum of two modified black bodies of temperatures

130 K and 300 K (peaking around 15 and 5 μm). The luminosity of each individual black body is free to vary. We enforce that this redistribution does not exceed 40% of the total H II dust luminosity. The dust-to-gas mass ratio in the H II phase is assumed to be equal to the one in the PDRs.

3. Optical/near-IR broadbands are used to constrain the escaping diffuse stellar radiation, $L_\nu^\star$, using the stellar population synthesis code PÉGASE (Fioc & Rocca-Volmerange 1997), with a Salpeter IMF, and a star formation rate as a function of time proportional to a power-law of the gas surface density with an index of 1.4 (Kennicutt 1998). We vary the initial gas mass surface density $\Sigma_{\rm gas}^0$ from 3 $M_\odot\,{\rm pc}^{-2}$ to 300 $M_\odot\,{\rm pc}^{-2}$. Here again, we assume a slab extinction, for the sake of simplicity. The power absorbed, $L_\star - \langle P_e L_\star \rangle$, contributes to the heating of the dust in PDRs.

4. The far-IR/submm observed SED constrains the dust emission from the PDRs. In order to account for variations of the radiation density, U, in these regions, we assume a power-law distribution, following the empirical prescription introduced by Dale et al. (2001):

$$L_\nu^{\rm PDR}(\nu) \propto \int_{U_-}^{U_+} L_\nu^{\rm Zub}(\nu, U) \times U^{-\alpha}\,{\rm d}U, \tag{9}$$

where $L_\nu^{\rm Zub}(\nu, U)$ is the dust SED corresponding to a single radiation density U. We adopt the dust properties of the Galactic diffuse ISM modeled by Zubko et al. (2004), for bare grains with solar abundance constraints. We fix the silicate-to-graphite mass ratio, but let free to vary the PAH-to-dust mass ratio, $f_{\rm PAH}$, as well as the fraction of ionized PAHs, f_+. These PAH properties are constrained by the detailed fit of the features seen on the mid-IR spectrum. The shape of the radiation field exciting the dust is:

$$U_\nu(\nu) \propto L_\nu^{\rm burst}(\nu) + L_\nu^\star(\nu). \tag{10}$$

This dust component is attenuated by the same factor than the diffuse ISRF, $P_e^{\rm PDR}(\nu)$, in order to reproduce the silicate extinction feature at 9.7 μm.

5. Our mid-IR spectra exhibit several fine structure ionic lines: $[{\rm Ar\,II}]_{6.98\mu m}$, $[{\rm Ar\,III}]_{8.99\mu m}$, $[{\rm S\,IV}]_{10.51\mu m}$, $[{\rm Ne\,II}]_{12.81\mu m}$, $[{\rm Ne\,III}]_{15.56\mu m}$, $[{\rm S\,III}]_{18.68\mu m}$, $[{\rm S\,III}]_{33.48\mu m}$ and $[{\rm Si\,II}]_{34.82\mu m}$. We fit these lines in order to get a better χ^2, but we do not use them for our physical interpretation. We adopt a Gauss profile whose width is determined by the resolution of the spectrograph. The luminosity, L_i, of each line is free to vary.

The total SED is then:

$$L_\nu(\nu) = P_e^{\rm H\,II}(\nu) \times L_\nu^{\rm burst}(\nu) + P_e^{\rm PDR}(\nu) \times \left[L_\nu^{\rm PDR}(\nu) + L_\nu^\star(\nu)\right] + L_\nu^{\rm sync}(\nu) + \sum_i L_\nu^{(i)}(\nu). \tag{11}$$

The energy conservation implies that:

$$\langle P_e L_{\mathrm{PDR}} \rangle = L_{\mathrm{burst}} - \langle P_e L_{\mathrm{burst}} \rangle + L_\star - \langle P_e L_\star \rangle. \tag{12}$$

Fig. 5 demonstrates this model, and Fig. 6 illustrates its geometry.

3.3.2. The Model Results

We fit the observed UV-to-radio SED, $L_\nu^{\mathrm{obs}}(\lambda_i) \pm \Delta L_\nu^{\mathrm{obs}}(\lambda_i)/2$ (i denoting an individual wavelength), of each one of the sources in Table 1, with Eq. (11), minimizing the χ^2. We weight each data point depending on the density of adjacent points:

$$\chi^2 = \sum_i \frac{\min_j(\lambda_j - \lambda_i)}{\lambda_i} \left(\frac{L_\nu^{\mathrm{obs}}(\lambda_i) - L_\nu(\lambda_i)}{\Delta L_\nu^{\mathrm{obs}}(\lambda_i)} \right)^2. \tag{13}$$

Eq. (13) prevents the χ^2 to be dominated by the parts of the electromagnetic spectrum where its sampling by the observations is dense. From this fit, we derive the value of the various free parameters. In particular, we are interested in the total PAH-to-gas (and PDR-dust-to-gas) mass ratio, $Z_{\mathrm{PAH(dust)}}$:

$$Z_{\mathrm{PAH(dust)}} = \frac{M_{\mathrm{PAH(dust)}}}{\mu \, (M_{\mathrm{H\,I}} + M_{\mathrm{H_2}})} \qquad \text{where} \qquad \mu = \frac{1}{1 - Y_\odot - Z_{\mathrm{gas}}}. \tag{14}$$
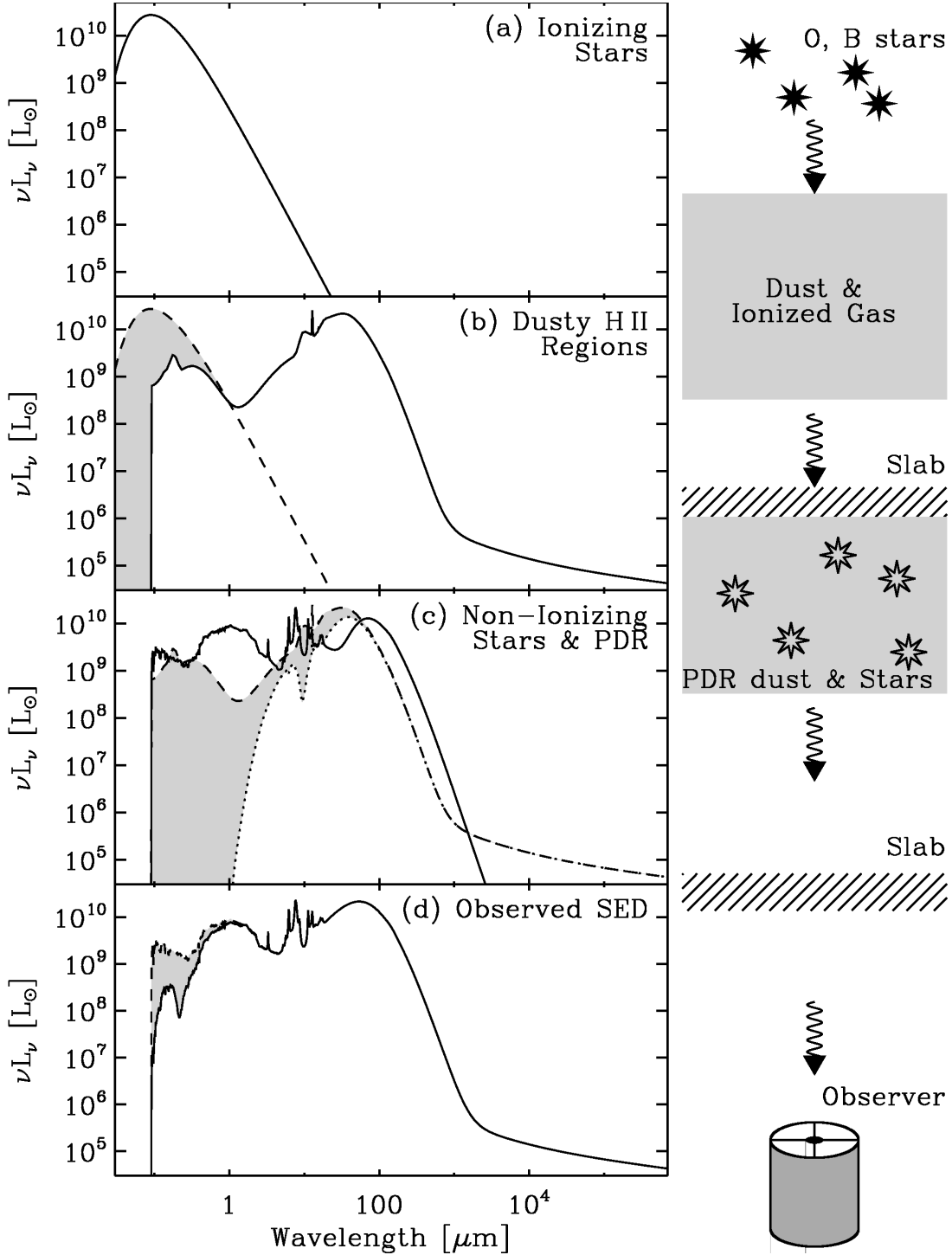
Fig. 6.— Illustration of the geometry of the model (Eq. 11). The left panels, from the top to the bottom shows the combination of the various SED building blocks from the massive star clusters to the observer. The solid lines are the total SED at each step; the dashed lines are the SED of the previous step; the part of the SED that has been absorbed is shown in grey. The right panel illustrate the path of the photons from the star clusters to the observer.

4. THE PAH AND DUST ABUNDANCES IN GALAXIES

We applied the method described in §3 to the sample in Table 1 (Figs. 7 to 24). The results are presented in Fig. 25 and Table 3.

PAH features are not detected in I Zw 18, SBS 0335-052, Mrk 153, NGC 5253 and NGC 1399. For these galaxies, we get an upper limit by fitting the short-wavelength part of the mid-IR spectrum with the maximum PAH amount allowed by the observational errors.

I Zw 18: The H I extends far out of the star forming region. Instead of normalizing the dust masses by the value of $M_{\mathrm{H\,I}}$ in Table 1, we consider that the H I mass associated to the star forming region is the one of the object H I-A (van Zee et al. 1998), where $M_{\mathrm{H\,I}} = 4.4 \times 10^7 \ M_\odot$.

SBS 0335-052: The 65 μm flux is the one reported by Hunt et al. (2005). The fit of this flux gives a far-IR dust temperature slightly colder than what we would obtain by fitting only the slope of the *Spitzer*/IRS spectrum. However, this gives a conservative solution, since we derive only an upper limit on the mass of PAHs, in this galaxy. The H I halo extends also far out of the star forming region. We assume that the star forming region has the same size than the optical galaxy, i.e. a radius of 1.6 kpc (6″). We derive the corresponding mass of H I, using the average column density of $N_{\mathrm{H\,I}} = 7.4 \times 10^{20}$ cm^{-2} reported by Pustilnik et al. (2001). We find $M_{\mathrm{H\,I}} = 4.6 \times 10^7 \ M_\odot$.

VII Zw 403: This *Spitzer*/IRS spectrum of this galaxy has been studied by Wu et al. (2006). However, they did not report any PAH detection. The degradation of the spectral resolution that we performed on this spectra (see §2.3) increases the signal-to-noise ratio significantly. We report a 4σ detection of the 7.7 μm feature, and marginal detections of the 6.2 and 8.6 μm features. This is the lowest metallicty PAH detection to date. Similarly to I Zw 18 and SBS 0335-052 the H I halo extends far out of the star forming region. To correct for this effect, we consider that the star forming region has a size $1' \times 0.5'$, with a column density $N_{\mathrm{H\,I}} = 1.6 \times 10^{21}$ cm^{-2} (Thuan et al. 2004). This leads to an effective $M_{\mathrm{H\,I}} = 1.1 \times 10^7 \ M_\odot$. This galaxy has only one radio point. To remain conservative, we assume that it is free-free dominated.

Mrk 153: The mid-infrared spectrum of this galaxy show prominent silicate emission. We do not have any radio observation of this object, therefore the contribution of H II regions to the total SED is rather uncertain.

Haro 11: As quoted by Bergvall et al. (2000), the ratio $M_{\mathrm{H\,I}}/L_{\mathrm{B}} < 0.01$ is abnormally low in this galaxy. The low value of the H I mass explains the high value of its dust-to-gas

mass ratio (Fig. 25). On the contrary, its PAH-to-dust mass ratio is not peculiar. This source, at 92 Mpc, is one of the most distant object in our sample.

IC 342: This galaxy is located at 10° of Galactic latitude. Hence, it is highly extincted by the foreground, which explains the peculiar shape of its optical/near-IR observed SED.

Tol 89: The mid-IR spectrum of this galaxy samples only its nucleus. That is the reason why it underestimates the $Spitzer$/IRAC$_{8\mu m}$ flux. To be conservative, we derive the lower limit on the PAH mass by fitting the spectrum, and the upper limit, by fitting the broad band. This galaxy has only one radio point. Therefore, we assume that it is free-free dominated.

NGC 1068: This galaxy contains a powerful AGN. In principle our model can not be applied to this object, since it does not take into account the contribution of the accretion disc. However, we fit this galaxy as if it was a starburst, in order to test the robustness of our approach.

NGC 1399: This object is a cD galaxy. Its interstellar medium is likely very tenuous and the mid-IR emission is dominated by the contribution of evolved stars. It has not been represented on the upper panel of Fig. 25, since we only know the upper limits on the PAH and H I gas masses. However, it is shown on the lower panel; the higher open circle is the ratio between the upper limit on the PAH mass and the lower limit on the dust mass.

Circinus: This galaxy is located at Galactic latitude below 5°. Like IC 342, its optical fluxes are very uncertain.

The top panel of Fig. 25 shows the variation of the PAH and dust to gas mass ratios with the metallicity of the interstellar medium. Each individual galaxy can be seen as a snapshot of galaxy evolution, at a given time. First, we note that the Galactic values of the dust-to-gas mass ratios are in agreement with the one of the other galaxies, around the same metallicity. These Galactic values were derived by Zubko et al. (2004), from the fit of the emission and extinction of the diffuse interstellar medium, with further constraints from the elemental depletion pattern. Thus, it is a very reliable estimation. This comparison confirms that our method does not overlook a significant amount of dust, at least around the solar metallicity. Second, the trends of Z_{PAH} and Z_{dust}, with the metallicity are not identical. Our sample spreads two orders of magnitude in metallicity. We can see that the PAH-to-gas mass ratio rises by five orders of magnitudes, while the dust-to-gas mass ratio, by only three. This differential evolution is illustrated in the lower panel of Fig. 25, showing the PAH-to-dust mass ratio. This figure is the analog of Fig. 1, but instead of considering

integrated fluxes, it deals with abundances. The PAH-to-dust mass ratio rises by two orders of magnitude, over our sample, while the $\mathrm{IRAC}_{8\mu m}/\mathrm{MIPS}_{24\mu m}$ band ratio varies only by one order of magnitude.
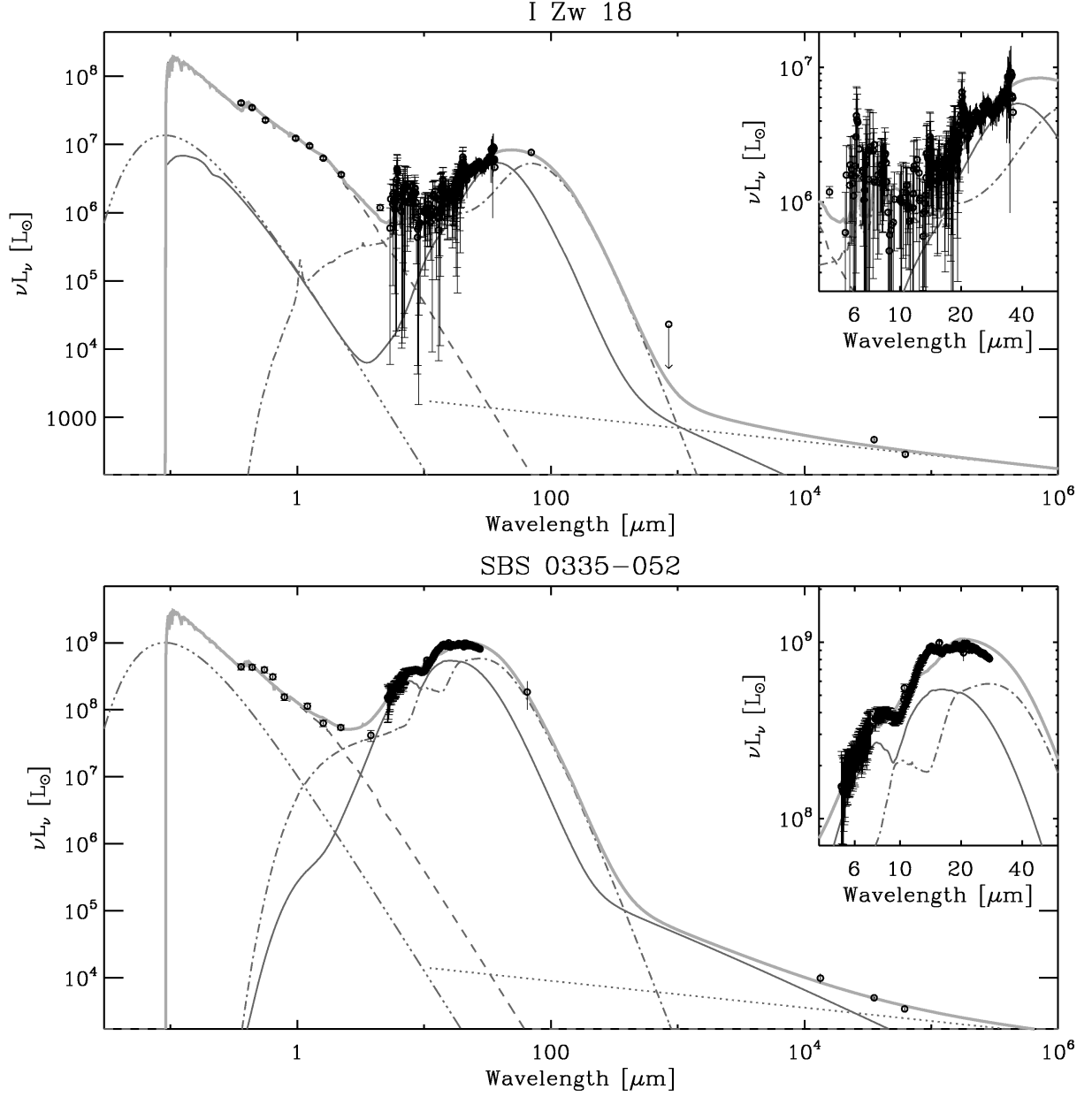
Fig. 7.— Fit of the galaxies' SEDs. The black lines are the components of the model (Fig. 5) and the thick grey line is the total observed SED. The circles with error bars are the broadband and spectral observations. The *top-right panel* shows the detailed fit of the mid-IR spectrum.
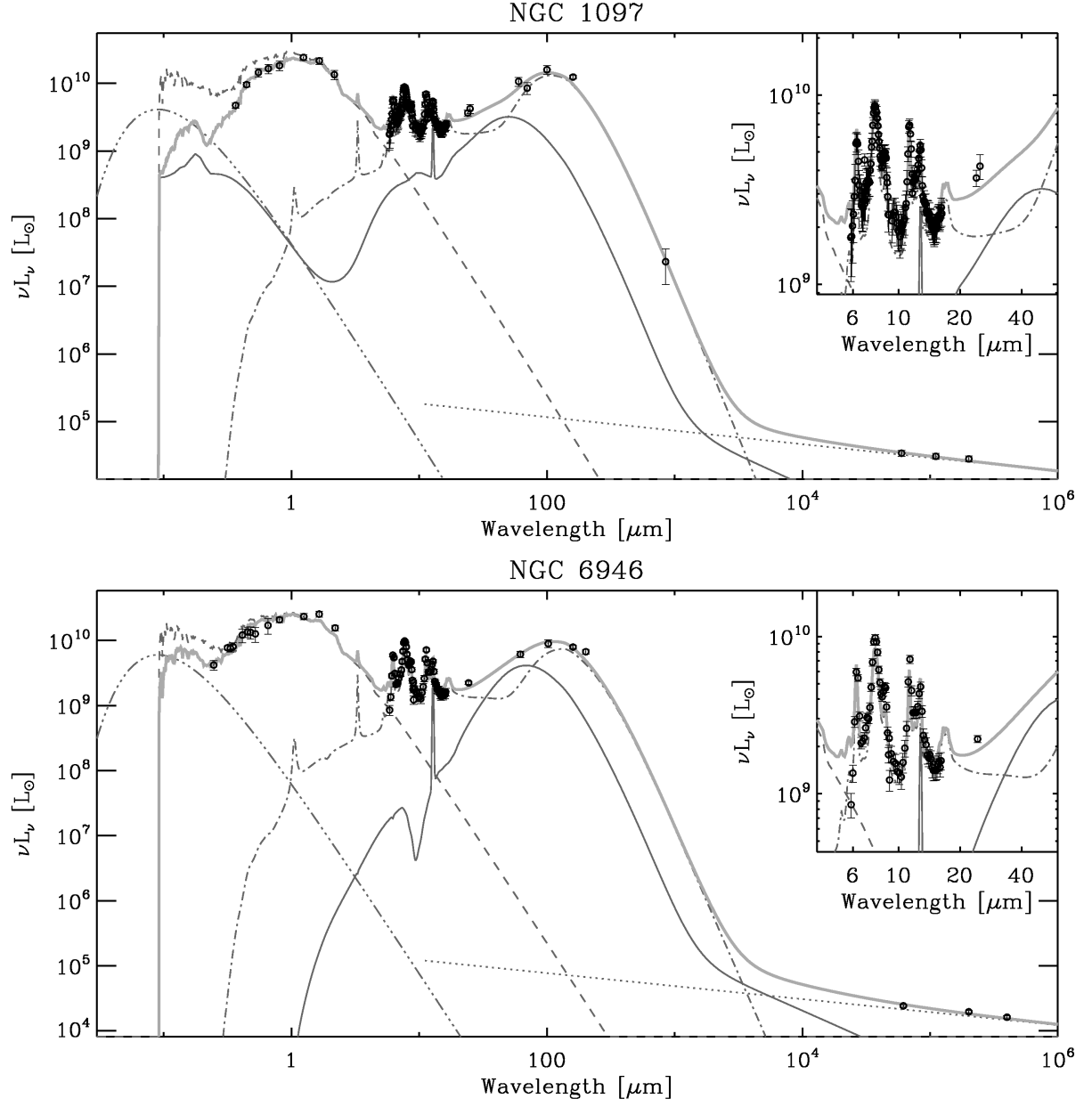
VII Zw 403

Mrk 153
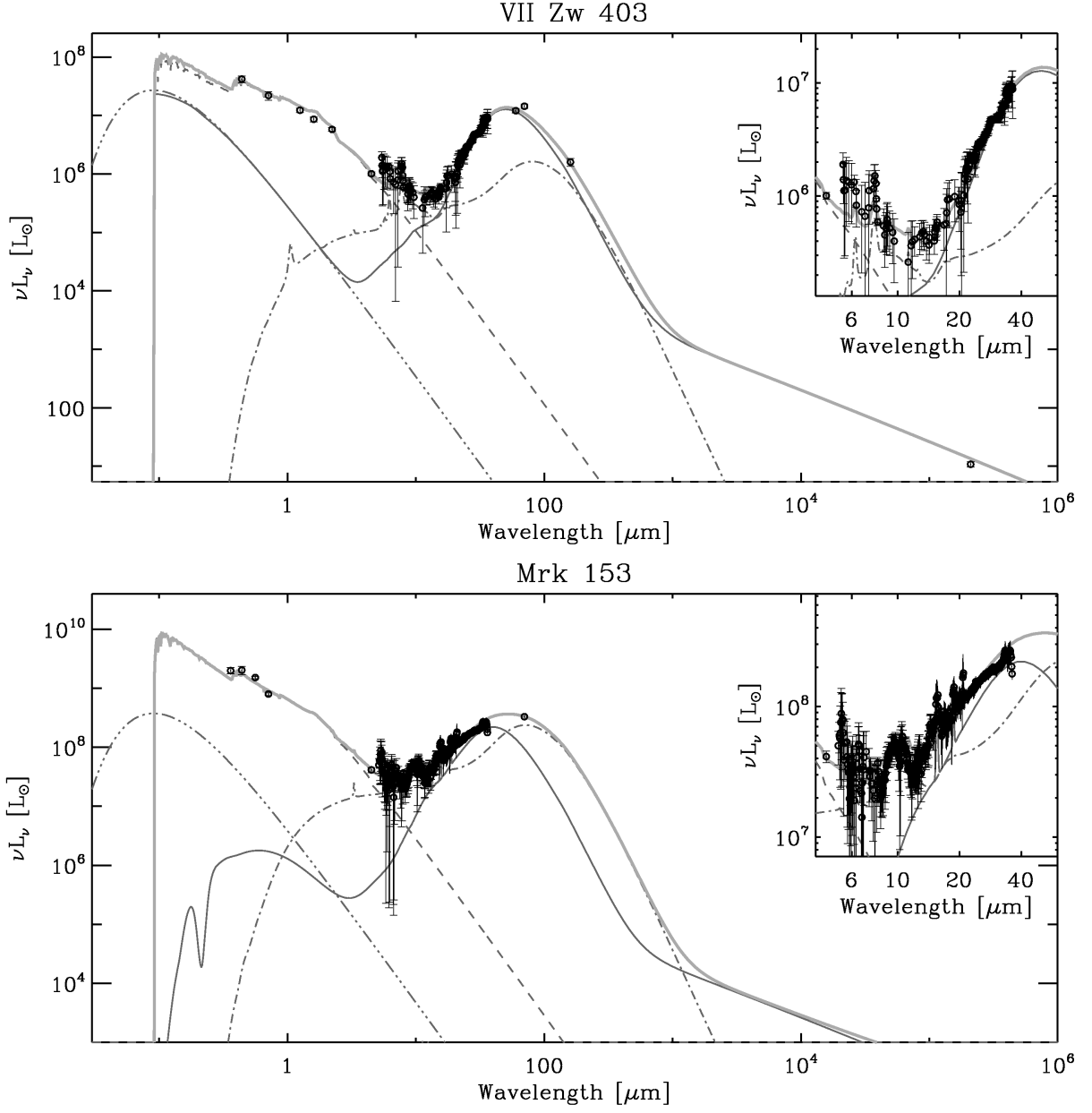
Fig. 8.— Fit of the galaxies' SEDs. See Fig. 7 for details.

Haro 11

NGC 1140
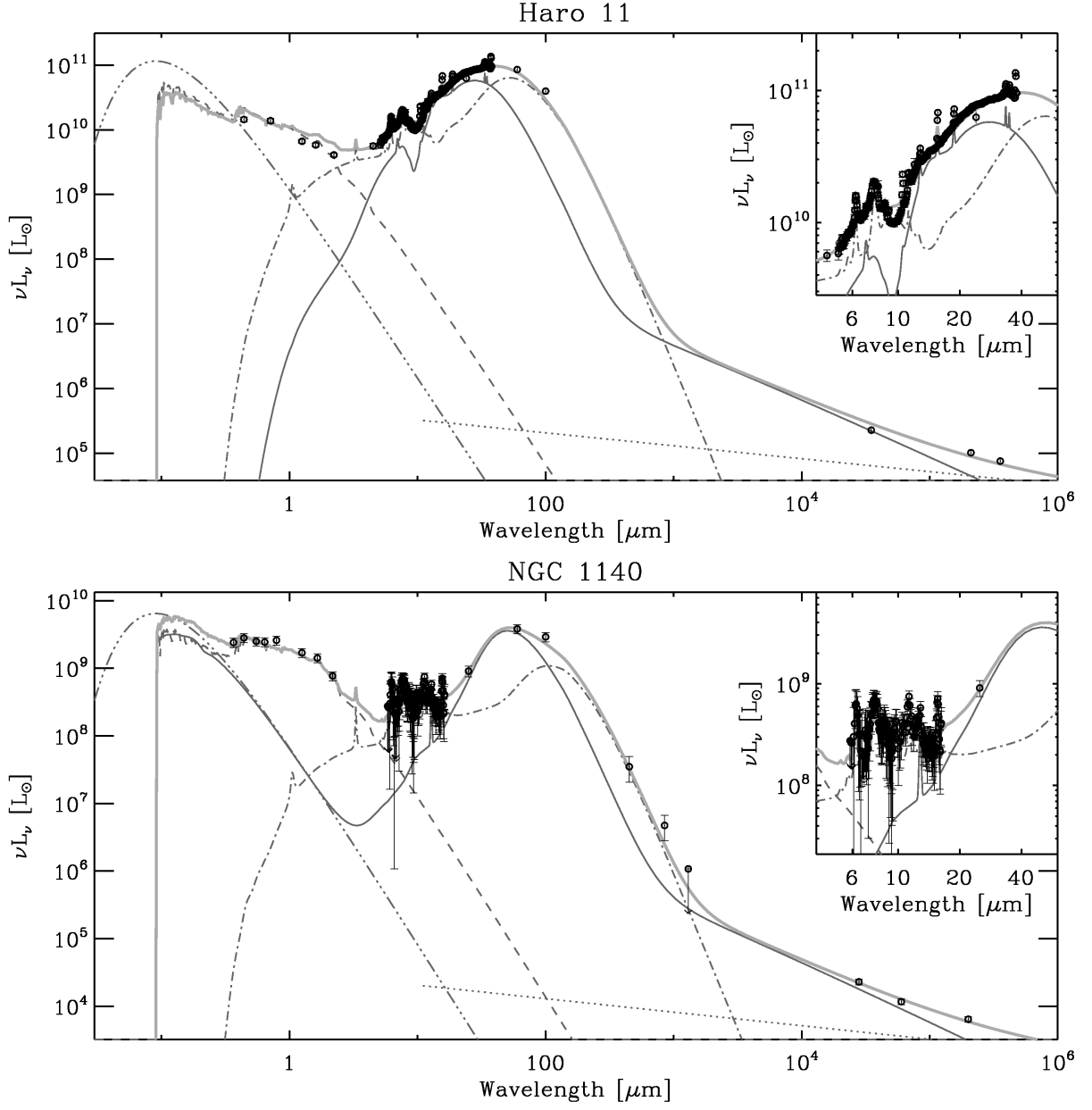
Fig. 9.— Fit of the galaxies' SEDs. See Fig. 7 for details.
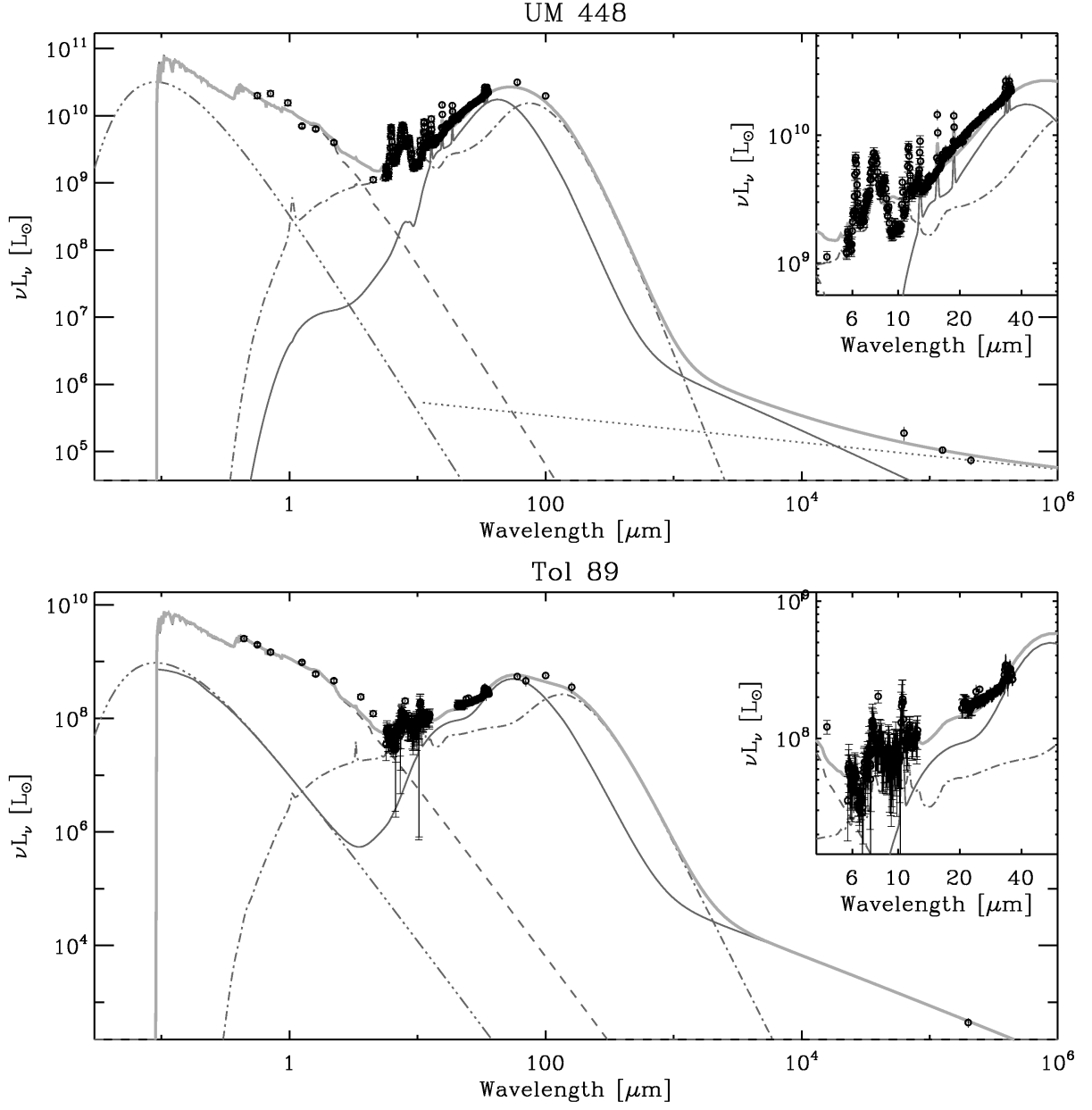
Fig. 10.— Fit of the galaxies' SEDs. See Fig. 7 for details.
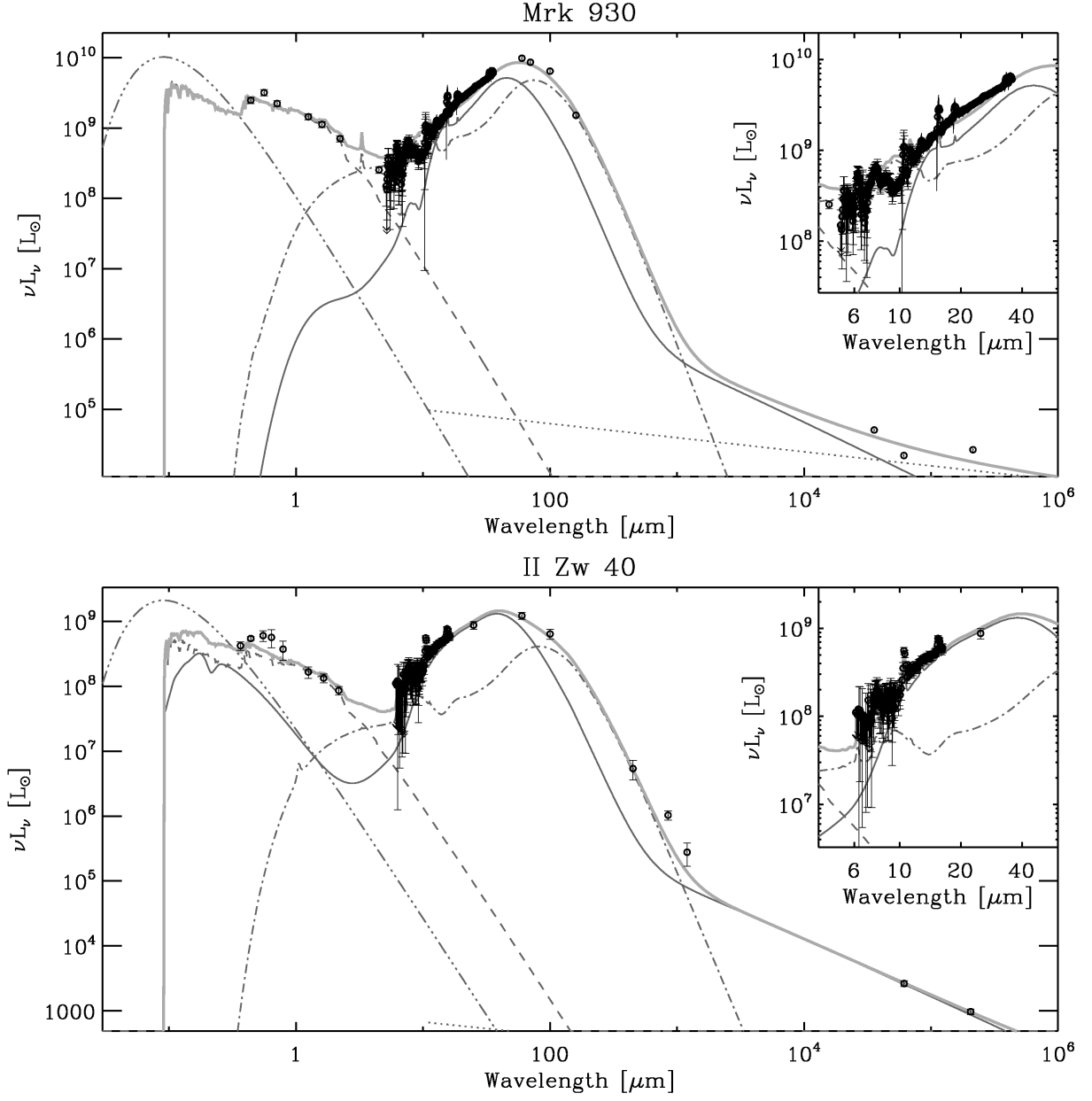
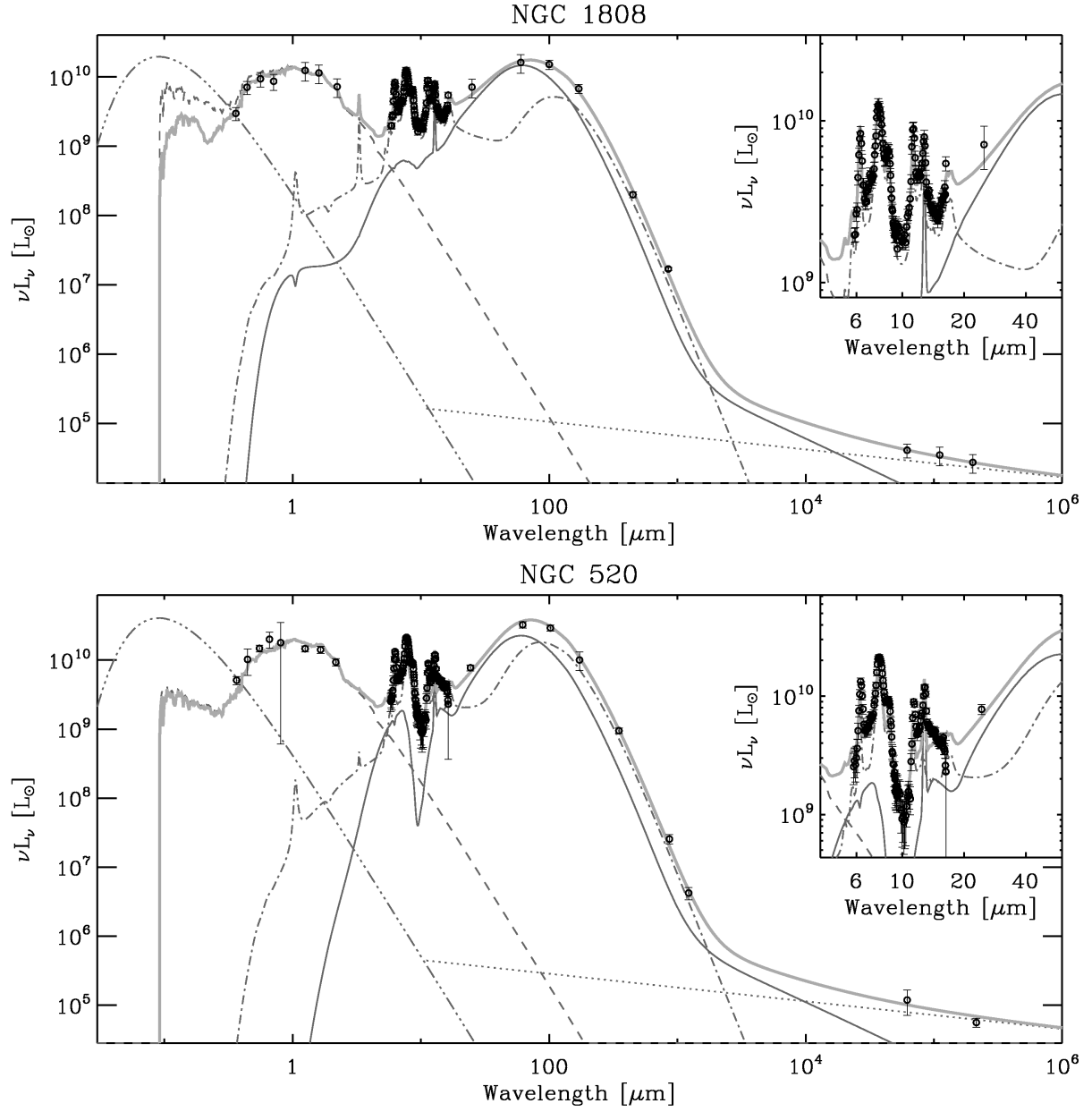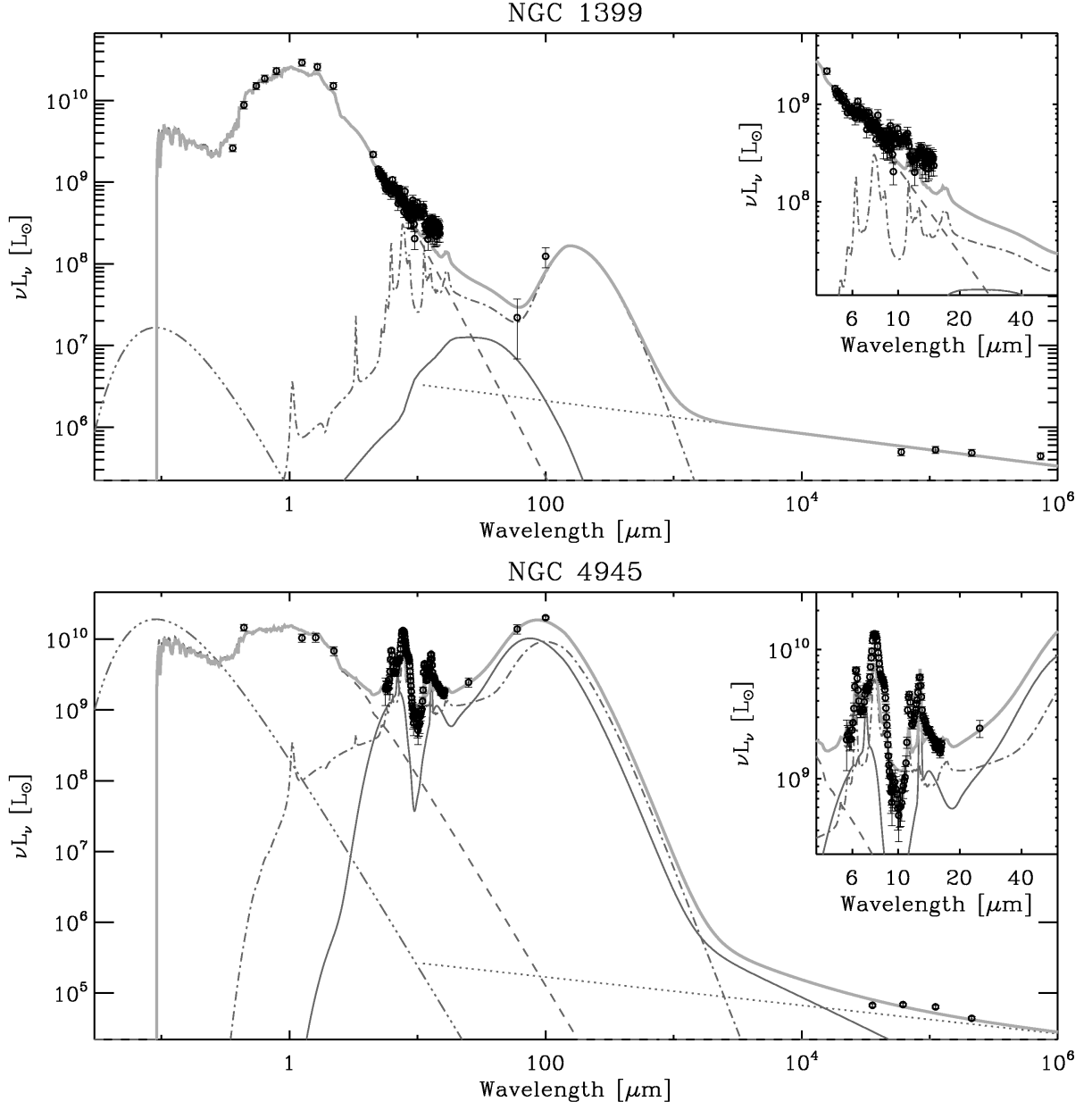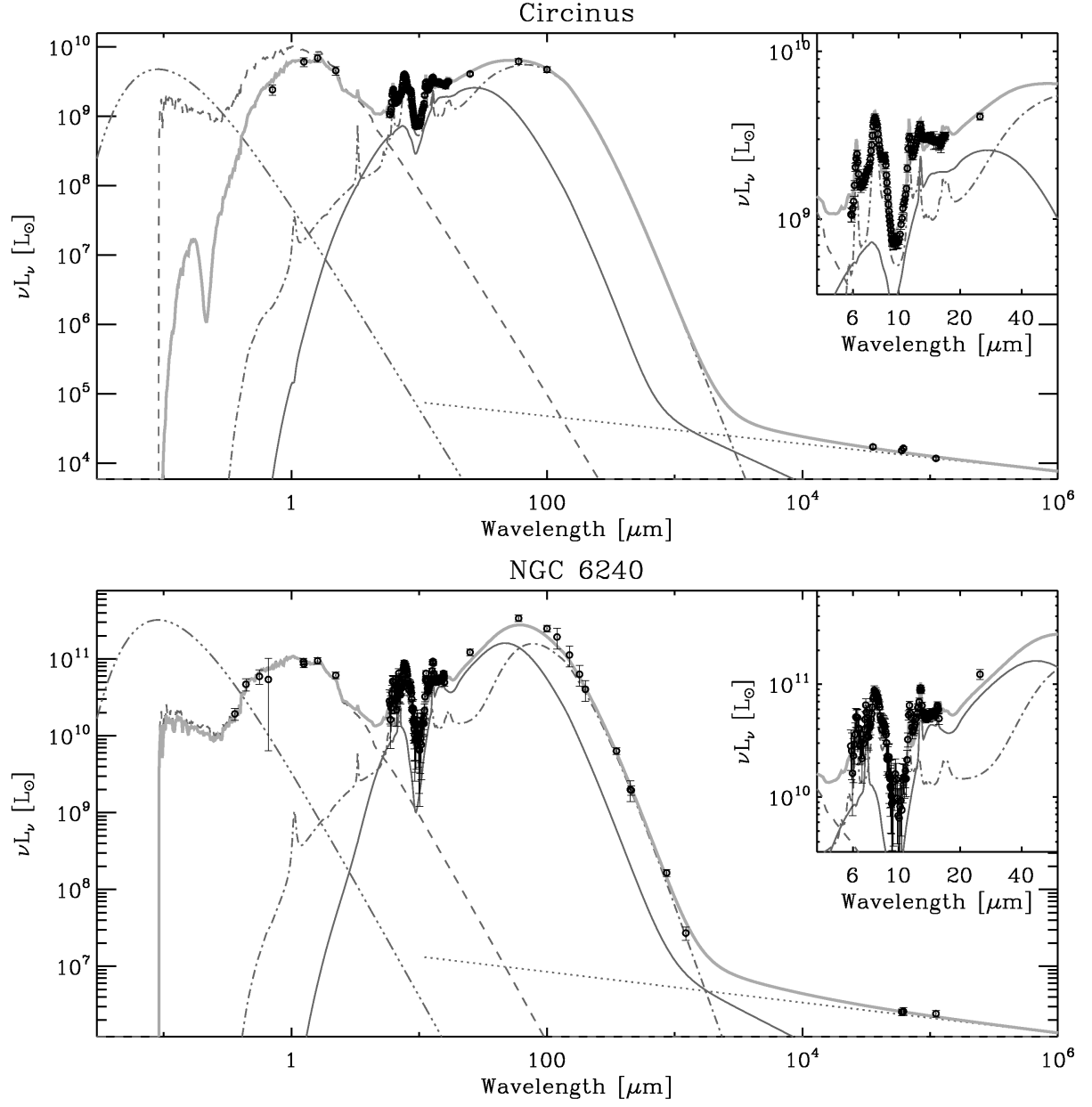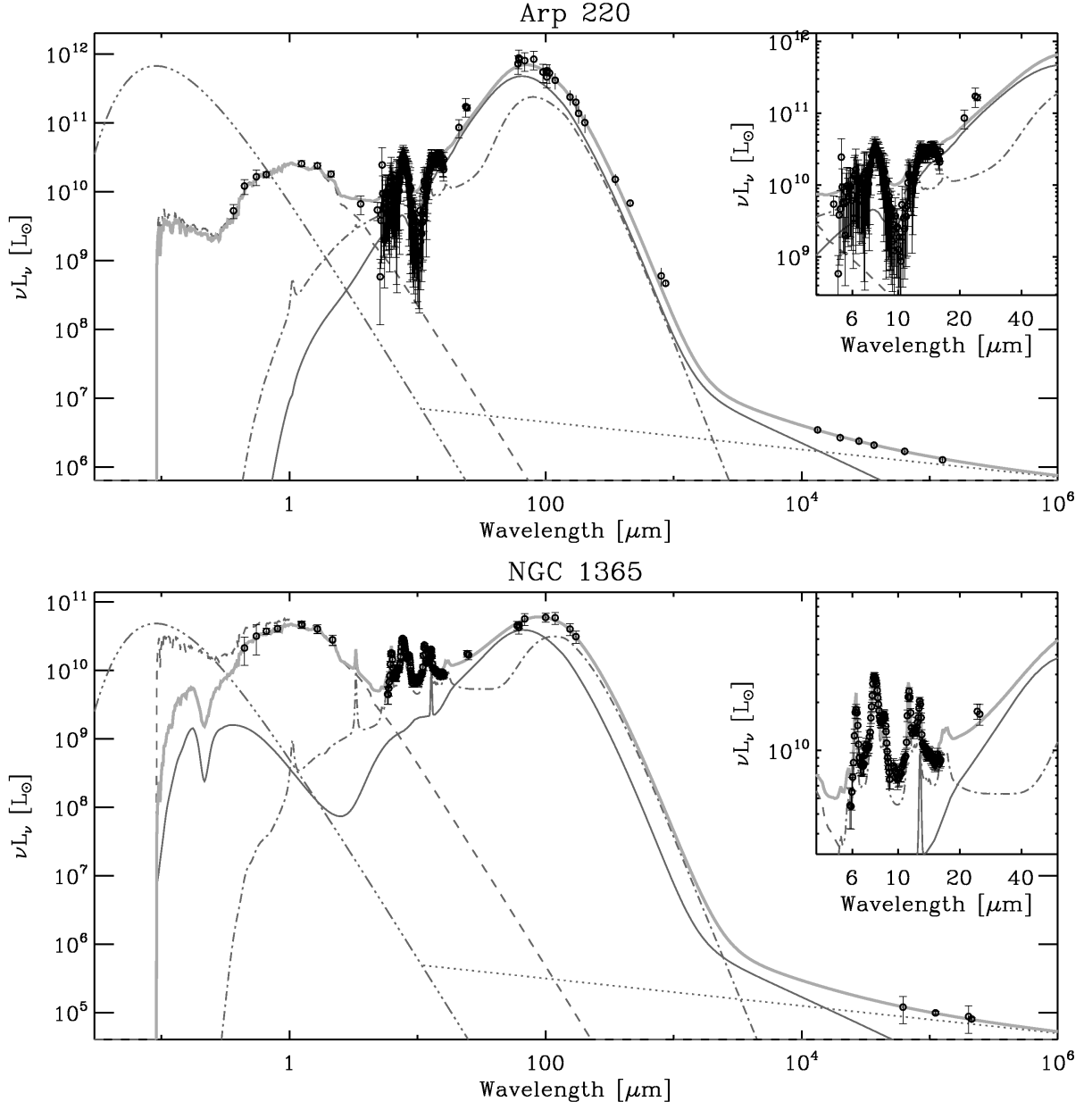Fig. 11.— Fit of the galaxies' SEDs. See Fig. 7 for details.
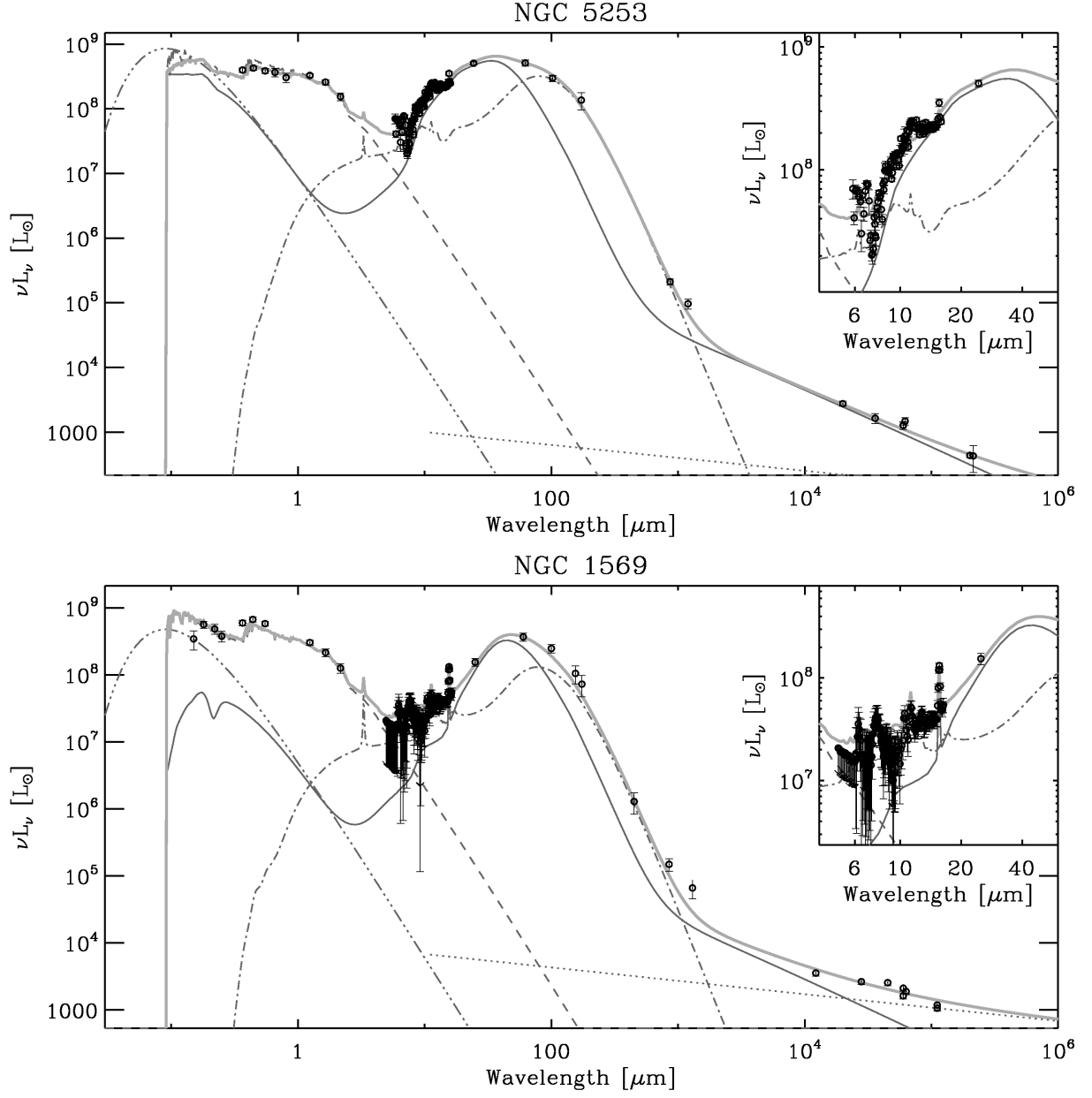
Fig. 12.— Fit of the galaxies' SEDs. See Fig. 7 for details.
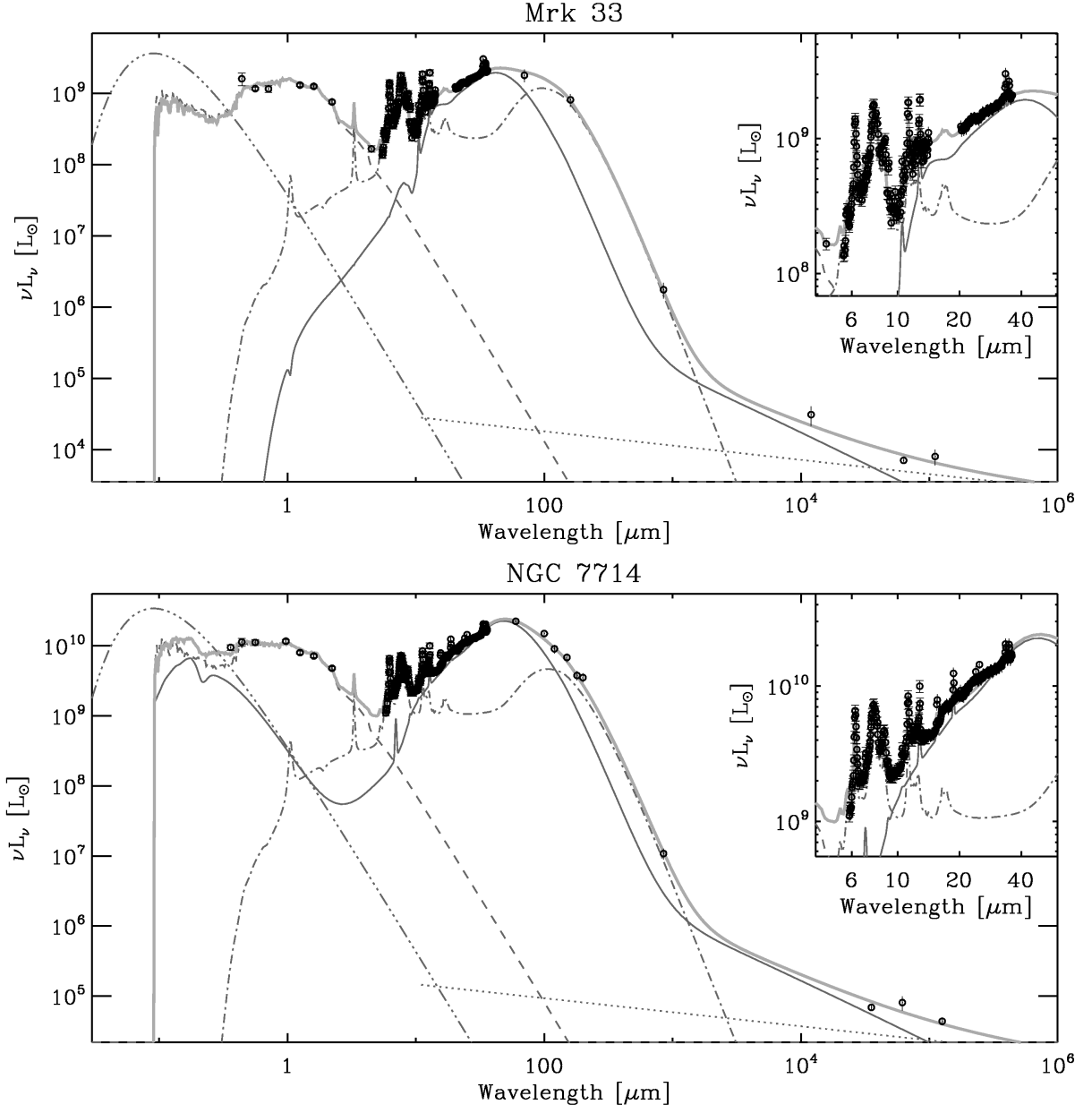
Fig. 13.— Fit of the galaxies' SEDs. See Fig. 7 for details.
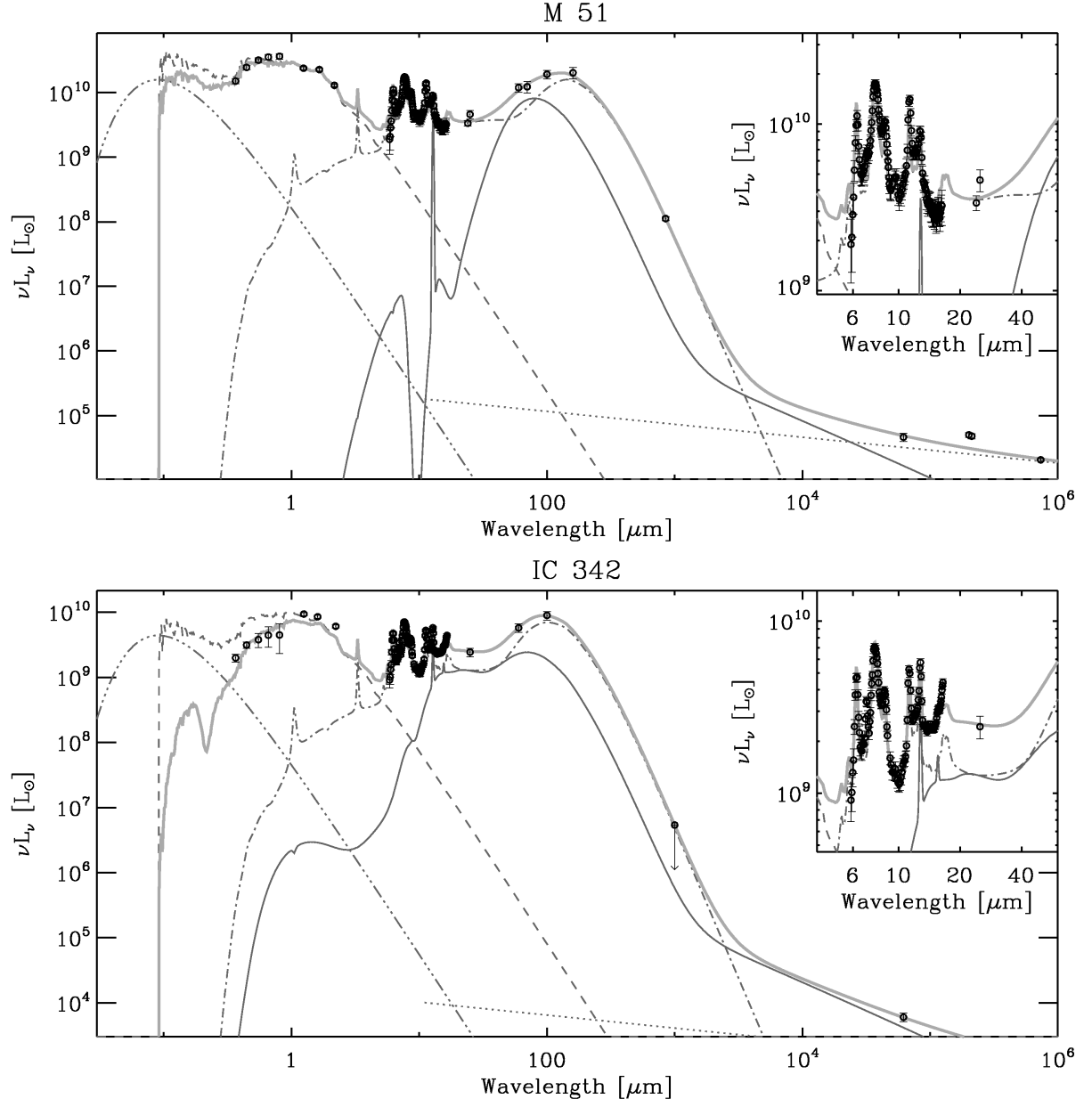
Fig. 14.— Fit of the galaxies' SEDs. See Fig. 7 for details.
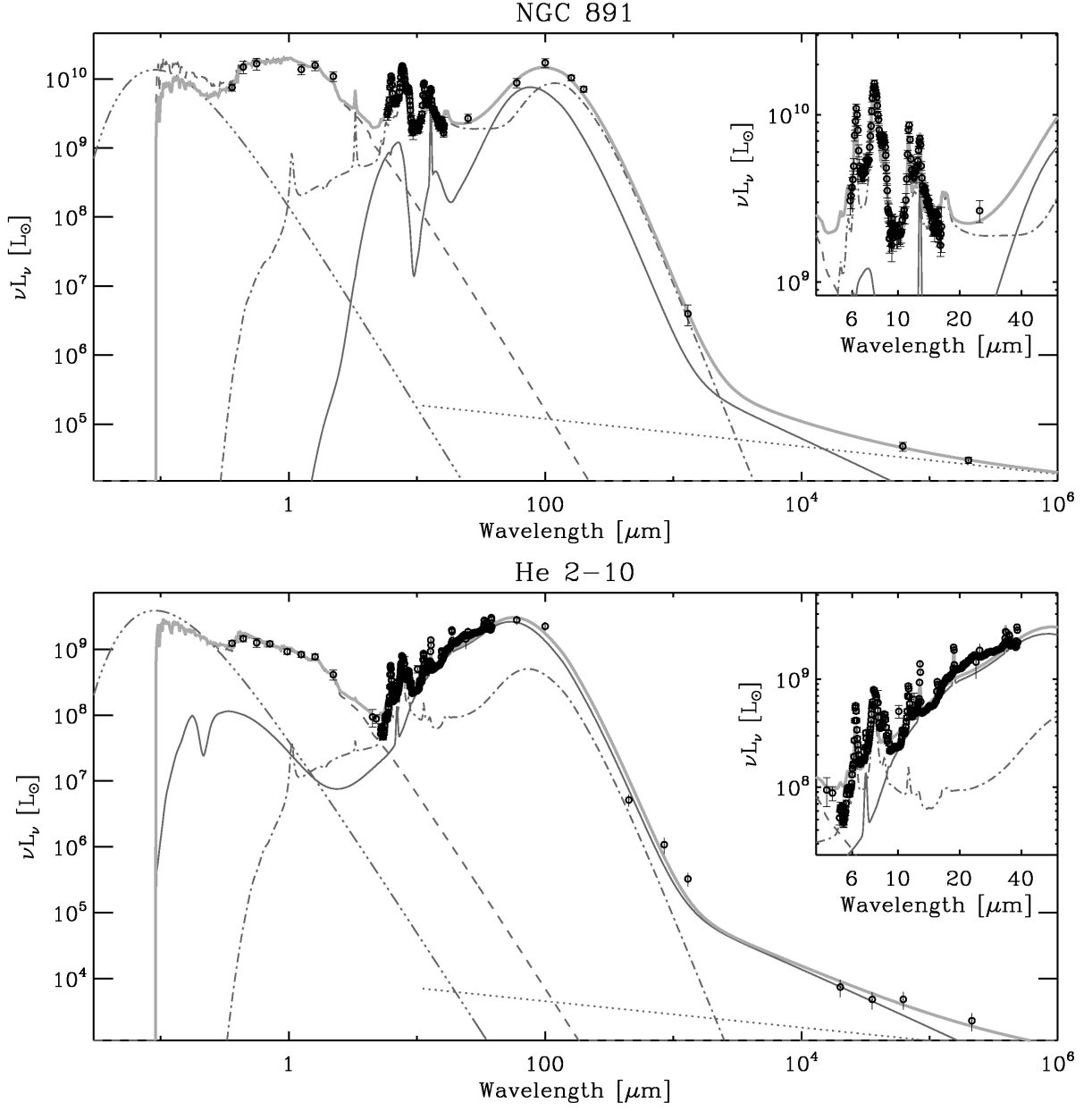
Fig. 15.— Fit of the galaxies' SEDs. See Fig. 7 for details.
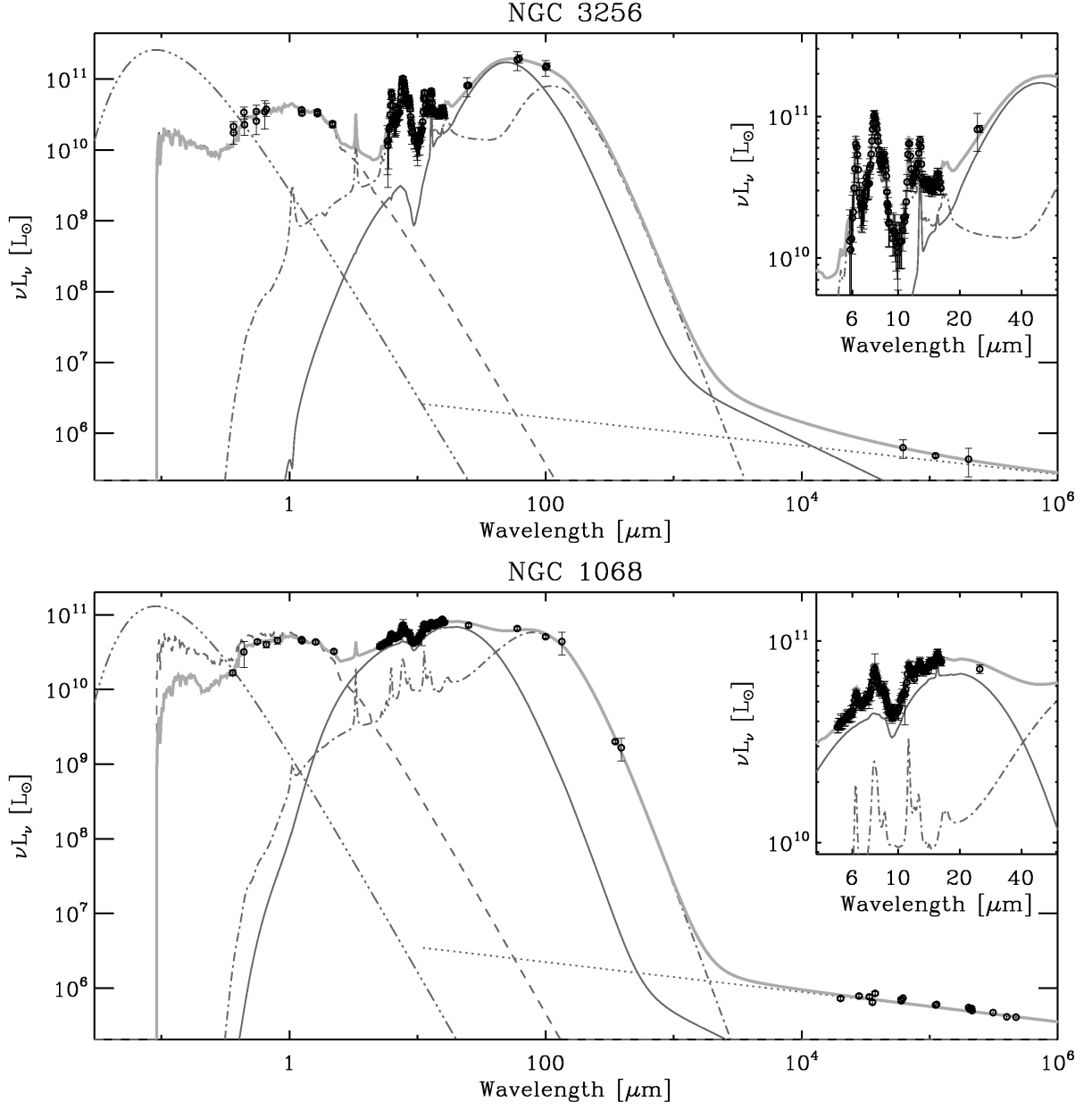
Fig. 16.— Fit of the galaxies' SEDs. See Fig. 7 for details.

NGC 253

M 82
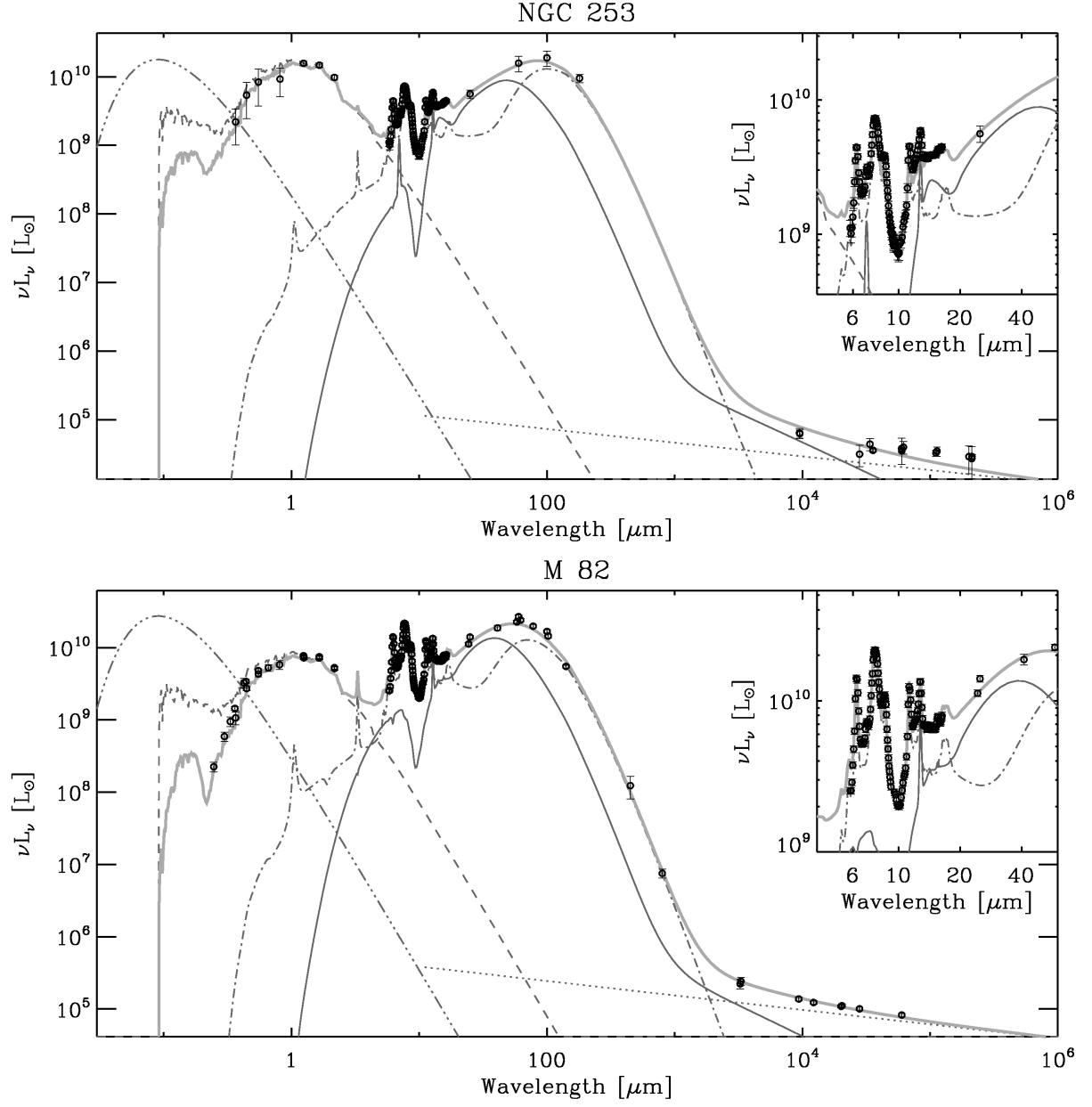
Fig. 17.— Fit of the galaxies' SEDs. See Fig. 7 for details.

Fig. 18.— Fit of the galaxies' SEDs. See Fig. 7 for details.

Fig. 19.— Fit of the galaxies' SEDs. See Fig. 7 for details.

NGC 1399

NGC 4945

Fig. 20.— Fit of the galaxies' SEDs. See Fig. 7 for details.

Fig. 21.— Fit of the galaxies' SEDs. See Fig. 7 for details.

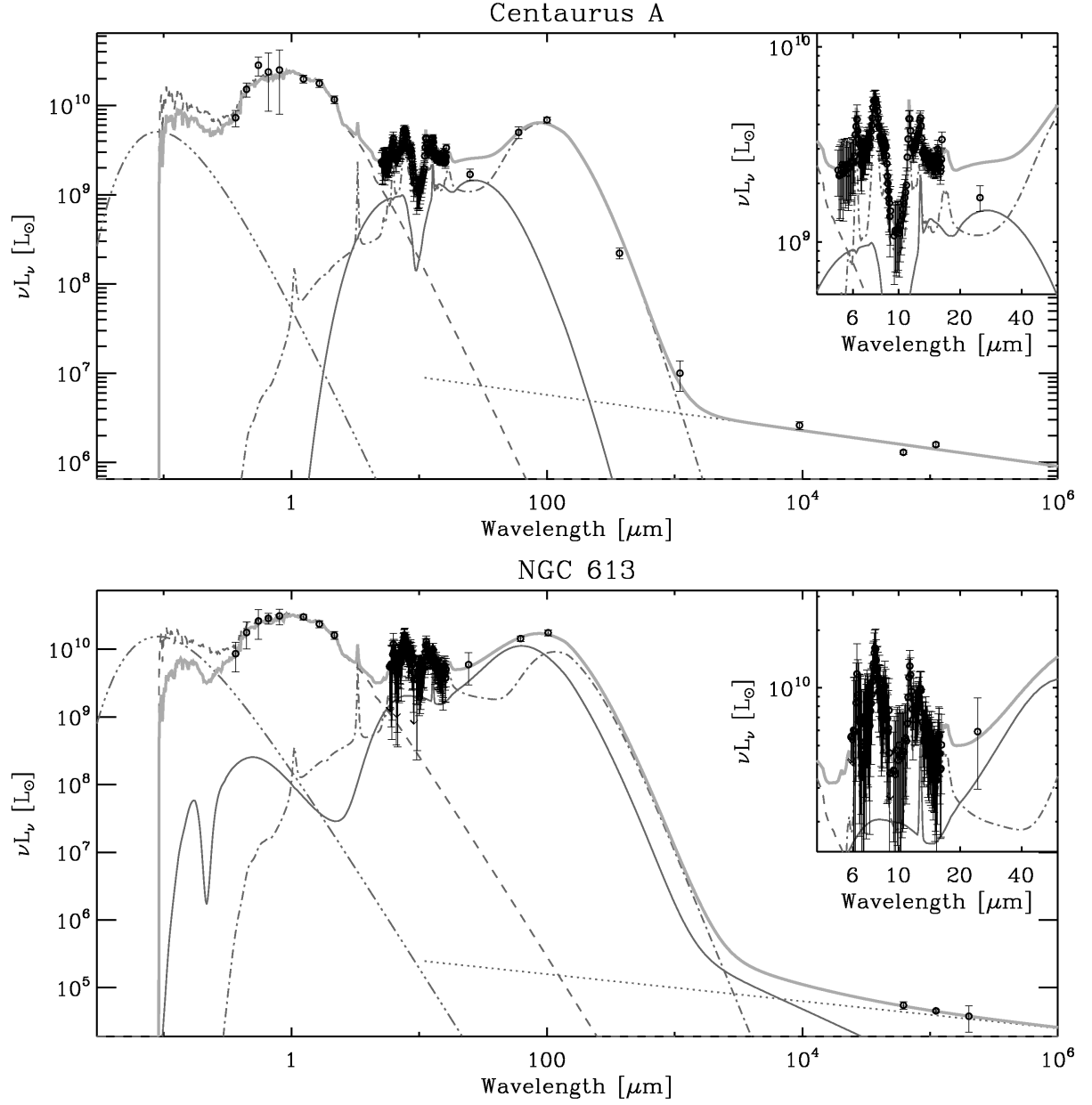Fig. 22.— Fit of the galaxies' SEDs. See Fig. 7 for details.

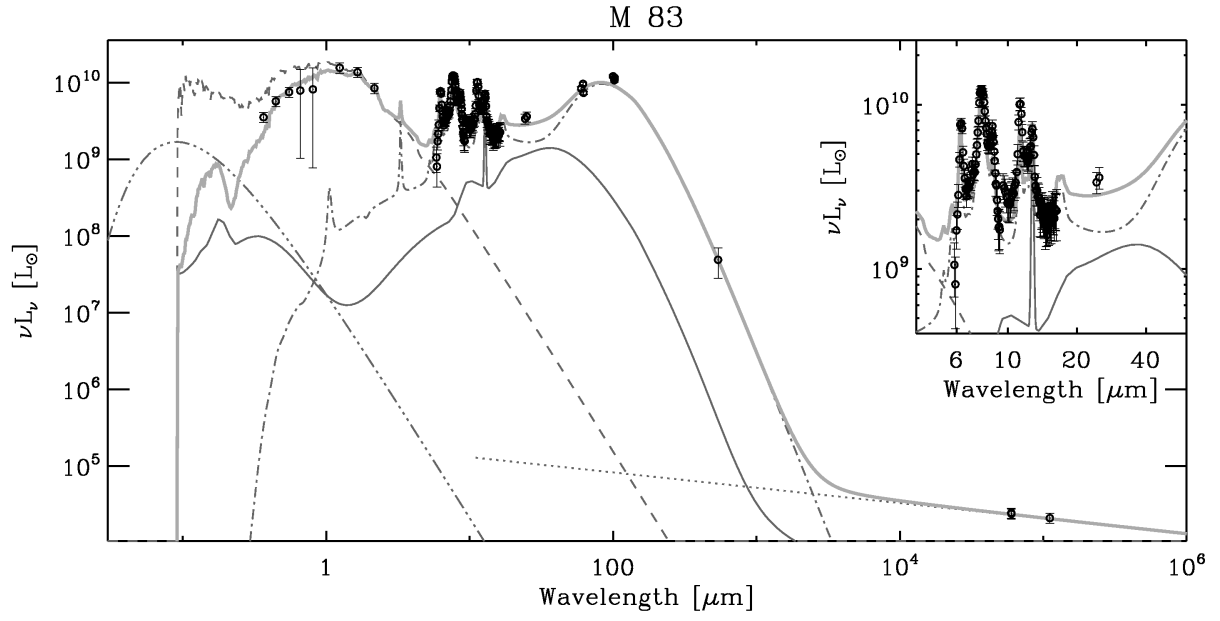Fig. 23.— Fit of the galaxies' SEDs. See Fig. 7 for details.

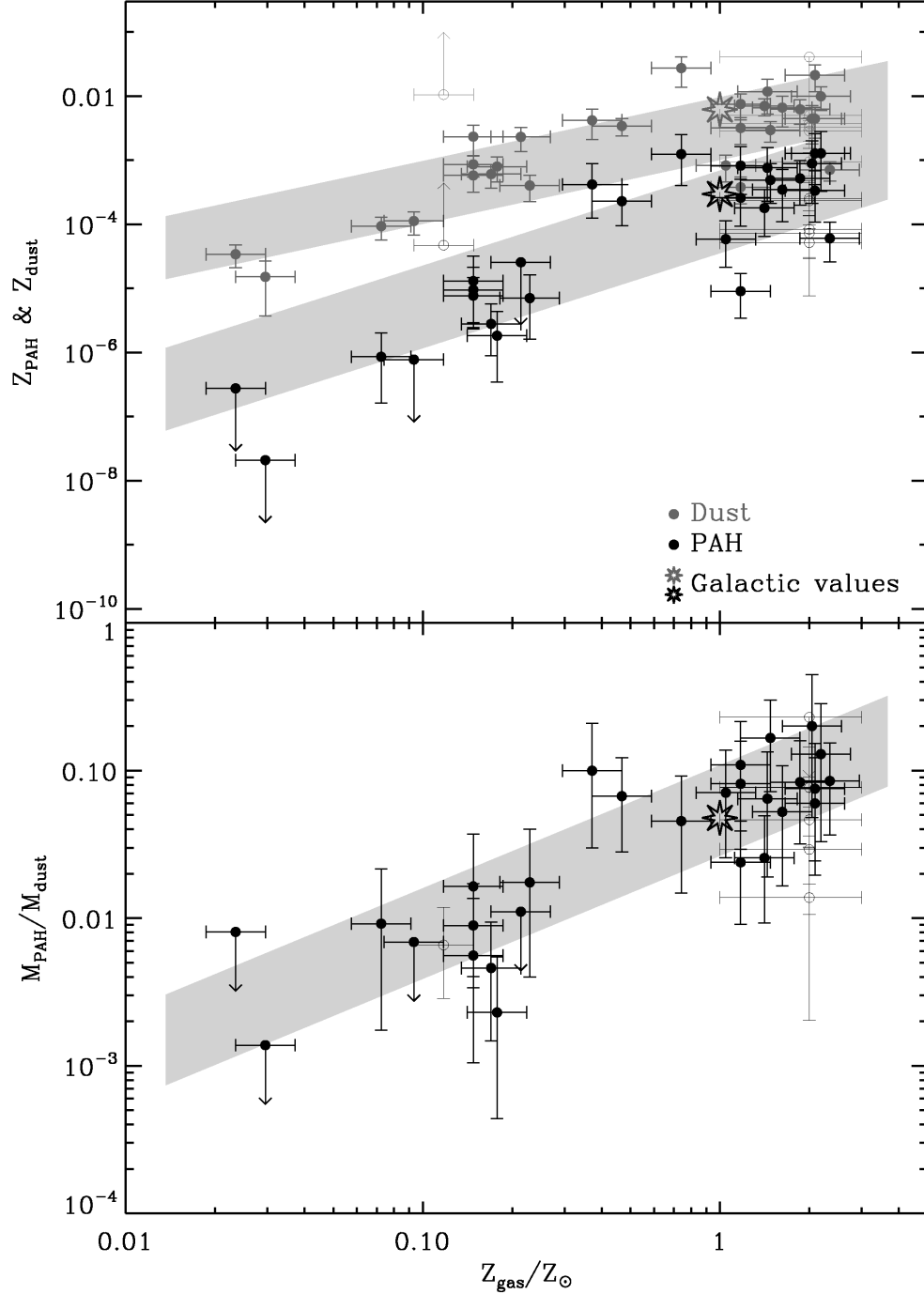Fig. 24.— Fit of the galaxies' SEDs. See Fig. 7 for details.

Fig. 25.— <u>Top panel</u>: dust-to-gas mass ratio for PAHs, Z_{PAH}, and the dust that gives rise to the far-IR emission, Z_{dust}, as a function of metallicity. <u>Bottom panel</u>: mass ratio of PAH-to-dust, as a function of metallicity. The circles correspond to galaxies and the open stars to the the diffuse Galactic ISM (Zubko et al. 2004). The filled circles are the reliable measurements, and the open circles are the ones which are considered uncertain. The grey stripes are the $\pm 1\sigma$ linear correlation, in logarithmic scale. These figures show the two distinct evolutionary trends of Z_{PAH} and Z_{dust} with metallicity.

Table 3. SED Modeling Results

Name	$Z_{\rm gas}$ $[Z_\odot]$	$Z_{\rm PAH}$	$Z_{\rm dust}$	$t_{\rm SF}$ [Myr]	$n_{\rm H}$ [cm^{-3}]	f_+	$L_{\rm burst}$ $[L_\odot]$	$L_{\rm PDR}$ $[L_\odot]$
I Zw 18	$0.023^{+0.005}_{-0.006}$	$\lesssim 2.7 \times 10^{-7}$	$3.4^{+1.3}_{-1.3} \times 10^{-5}$	160	70	...	1.6×10^7	$8.3 \times 10^{6\,(?)}$
SBS 0335-052	$0.030^{+0.006}_{-0.008}$	$\lesssim 2.1 \times 10^{-8}$	$1.5^{+1.1}_{-1.1} \times 10^{-5}$	110	2.0×10^4	...	1.6×10^9	8.6×10^8
VII Zw 403	$0.072^{+0.015}_{-0.019}$	$8.6^{+6.9}_{-11.5} \times 10^{-7}$	$9.3^{+3.6}_{-3.6} \times 10^{-5}$	650	$30^{(?)}$	$1.0^{(?)}$	$3.4 \times 10^{7\,(?)}$	2.6×10^6
Mrk 153	$0.093^{+0.019}_{-0.024}$	$\lesssim 7.7 \times 10^{-7}$	$1.1^{+0.4}_{-0.4} \times 10^{-4}$	190	$110^{(?)}$	0.0	$5.1 \times 10^{8\,(?)}$	$3.6 \times 10^{8\,(?)}$
Haro 11	$0.12^{+0.02}_{-0.03}$	$1.1^{+0.6}_{-0.9} \times 10^{-4\,(?)}$	$1.6^{+0.6}_{-0.6} \times 10^{-2\,(?)}$	680	1.0×10^3	0.7	1.6×10^{11}	9.2×10^{10}
NGC 1140	$0.15^{+0.03}_{-0.04}$	$9.5^{+7.2}_{-11.9} \times 10^{-6}$	$5.8^{+2.6}_{-2.6} \times 10^{-4}$	1610	30	0.4	8.2×10^9	1.8×10^9
UM 448	$0.15^{+0.03}_{-0.04}$	$7.7^{+4.8}_{-7.0} \times 10^{-6}$	$8.6^{+3.2}_{-3.2} \times 10^{-4}$	450	100	1.0	4.3×10^{10}	2.4×10^{10}
Tol 89	$0.15^{+0.03}_{-0.04}$	$1.3^{+1.1}_{-1.9} \times 10^{-5}$	$2.3^{+1.2}_{-1.2} \times 10^{-3}$	470	$20^{(?)}$	$0.3^{(?)}$	$1.2 \times 10^{9\,(?)}$	4.6×10^8
Mrk 930	$0.17^{+0.03}_{-0.04}$	$2.8^{+1.9}_{-2.9} \times 10^{-6}$	$6.1^{+2.4}_{-2.4} \times 10^{-4}$	1360	70	...	1.3×10^{10}	7.2×10^9
II Zw 40	$0.18^{+0.04}_{-0.05}$	$1.8^{+1.5}_{-2.5} \times 10^{-6}$	$7.9^{+3.4}_{-3.4} \times 10^{-4}$	1330	150	$1.0^{(?)}$	2.8×10^9	6.4×10^8
NGC 5253	$0.21^{+0.04}_{-0.06}$	$\lesssim 2.6 \times 10^{-5}$	$2.3^{+0.9}_{-0.9} \times 10^{-3}$	1520	320	...	1.1×10^9	5.0×10^8
NGC 1569	$0.23^{+0.05}_{-0.06}$	$7.0^{+5.4}_{-9.1} \times 10^{-6}$	$4.0^{+1.8}_{-1.8} \times 10^{-4}$	1280	80	0.0	6.3×10^8	2.2×10^8
Mrk 33	$0.37^{+0.08}_{-0.10}$	$4.2^{+2.9}_{-4.6} \times 10^{-4}$	$4.2^{+2.1}_{-2.1} \times 10^{-3}$	5110	130	0.6	4.8×10^9	2.2×10^9
NGC 7714	$0.47^{+0.10}_{-0.12}$	$2.3^{+1.3}_{-1.9} \times 10^{-4}$	$3.4^{+1.0}_{-1.0} \times 10^{-3}$	3100	60	0.6	4.3×10^{10}	9.4×10^9
M 51	$0.74^{+0.15}_{-0.19}$	$1.2^{+0.8}_{-1.3} \times 10^{-3}$	$2.7^{+1.4}_{-1.4} \times 10^{-2}$	2570	10	0.5	2.2×10^{10}	3.1×10^{10}
IC 342	$1.0^{+0.2}_{-0.3}$	$5.8^{+3.7}_{-5.5} \times 10^{-5}$	$8.3^{+3.7}_{-3.7} \times 10^{-4}$	4610	$10^{(?)}$	0.5	$6.2 \times 10^{9\,(?)}$	1.2×10^{10}
NGC 891	$1.2^{+0.2}_{-0.3}$	$2.6^{+1.7}_{-2.5} \times 10^{-4}$	$3.2^{+1.4}_{-1.4} \times 10^{-3}$	3690	10	0.6	1.9×10^{10}	1.7×10^{10}
He 2-10	$1.2^{+0.2}_{-0.3}$	$9.0^{+5.6}_{-8.1} \times 10^{-6}$	$3.8^{+1.7}_{-1.7} \times 10^{-4}$	1240	40	1.0	5.1×10^9	8.4×10^8
NGC 3256	$1.2^{+0.2}_{-0.3}$	$8.2^{+5.3}_{-7.9} \times 10^{-4}$	$7.5^{+3.2}_{-3.2} \times 10^{-3}$	6740	90	0.6	3.7×10^{11}	1.5×10^{11}
NGC 1068	$1.4^{+0.3}_{-0.4}$	$1.8^{+1.1}_{-1.7} \times 10^{-4}$	$7.0^{+2.1}_{-2.1} \times 10^{-3}$	3710	1.0×10^4	0.2	2.0×10^{11}	1.1×10^{11}
NGC 253	$1.4^{+0.3}_{-0.4}$	$7.6^{+5.3}_{-8.2} \times 10^{-4}$	$1.2^{+0.6}_{-0.6} \times 10^{-2}$	14000	100	0.7	2.7×10^{10}	1.9×10^{10}
M 82	$1.5^{+0.3}_{-0.4}$	$4.9^{+2.8}_{-3.9} \times 10^{-4}$	$2.9^{+1.0}_{-1.0} \times 10^{-3}$	9040	530	0.7	3.8×10^{10}	2.4×10^{10}
NGC 1097	$1.6^{+0.3}_{-0.4}$	$3.5^{+2.4}_{-3.6} \times 10^{-4}$	$6.6^{+3.3}_{-3.3} \times 10^{-3}$	6060	50	0.5	5.7×10^9	2.1×10^{10}
NGC 6946	$1.9^{+0.4}_{-0.5}$	$5.2^{+3.2}_{-4.7} \times 10^{-4}$	$6.2^{+2.6}_{-2.6} \times 10^{-3}$	5210	20	0.5	8.4×10^9	1.3×10^{10}
NGC 1808	$2.0^{+0.4}_{-0.5}$	$8.9^{+6.7}_{-11.0} \times 10^{-4}$	$4.4^{+2.7}_{-2.7} \times 10^{-3}$	6040	30	0.6	2.8×10^{10}	1.2×10^{10}
NGC 520	$2.0^{+1.0\,(?)}_{-1.0}$	$2.5^{+1.5}_{-2.2} \times 10^{-4}$	$3.3^{+1.3}_{-1.3} \times 10^{-3}$	13900	50	1.0	5.8×10^{10}	2.8×10^{10}
NGC 1399	$2.0^{+1.0\,(?)}_{-1.0}$	$\lesssim 9.3 \times 10^{-3\,(?)}$	$\lesssim 4.1 \times 10^{-2}$	14000	$300^{(?)}$	...	$2.4 \times 10^{7\,(?)}$	$3.2 \times 10^{8\,(?)}$
NGC 4945	$2.0^{+1.0\,(?)}_{-1.0}$	$8.3^{+5.3}_{-7.9} \times 10^{-5}$	$2.8^{+1.3}_{-1.3} \times 10^{-3}$	4660	10	1.0	2.7×10^{10}	1.4×10^{10}
Circinus	$2.0^{+1.0\,(?)}_{-1.0}$	$7.3^{+4.4}_{-6.4} \times 10^{-5}$	$9.4^{+3.8}_{-3.8} \times 10^{-4}$	14000	1.1×10^3	0.5	7.3×10^9	1.1×10^{10}
NGC 6240	$2.0^{+1.0\,(?)}_{-1.0}$	$2.3^{+1.5}_{-2.2} \times 10^{-4}$	$5.0^{+2.0}_{-2.0} \times 10^{-3}$	12940	100	0.8	4.5×10^{11}	2.3×10^{11}
Arp 220	$2.0^{+1.0\,(?)}_{-1.0}$	$5.2^{+4.4}_{-8.3} \times 10^{-5}$	$3.7^{+2.2}_{-2.2} \times 10^{-3}$	14000	20	$1.0^{(?)}$	9.4×10^{11}	3.0×10^{11}
NGC 1365	$2.1^{+0.4}_{-0.5}$	$3.3^{+2.3}_{-3.4} \times 10^{-4}$	$4.4^{+2.2}_{-2.2} \times 10^{-3}$	5490	20	0.4	7.1×10^{10}	5.5×10^{10}
Centaurus A	$2.1^{+0.4}_{-0.5}$	$1.3^{+0.9}_{-1.3} \times 10^{-3}$	$2.1^{+1.0}_{-1.0} \times 10^{-2}$	5480	8.6×10^3	0.3	8.0×10^9	1.1×10^{10}
NGC 613	$2.2^{+0.4}_{-0.6}$	$1.3^{+1.0}_{-1.5} \times 10^{-3}$	$9.9^{+3.9}_{-3.9} \times 10^{-3}$	5590	20	0.3	2.2×10^{10}	1.8×10^{10}

5.   A MODEL FOR THE GAS AND DUST EVOLUTION

We have developed a one-zone single-phase chemical evolution model, to follow the abundances and composition of the dust and the metallicty as a function of time, in order to interpret the results of our SED modeling. In this section, we will give a brief description of the physical processes which are incorporated. A more detailed discussion can be found in Dwek (1998) and Dwek et al. (2007). Assuming a common star formation history, we will use this model to interpret the observed evolutionary trend of galaxies' SED with metallicity, on a global scale.

5.1.   Metal Enrichment and Gas Evolution

In the present paper, we consider a closed box model. We consider the delayed injection of material by different stellar progenitors, but we assume that the mixing of the elements in the ISM is instantaneous. To be consistent with our stellar population synthesis, we adopt a Salpeter initial mass function, $\phi(m)$ (Eq. 7), where m is the mass of individual stars. We define the average stellar mass:

$$\langle m \rangle \equiv \int_{m_l}^{m_u} m\,\phi(m)\,\mathrm{d}m. \tag{15}$$

The evolution of the gas mass surface density, $\Sigma_{\mathrm{gas}}(t)$, with the time t, is:

$$\frac{\mathrm{d}\Sigma_{\mathrm{gas}}(t)}{\mathrm{d}t} = -\Sigma_{\mathrm{SFR}}(t) + \int_{m_l}^{m_u} \Sigma_{\mathrm{SFR}}(t - \tau(m))\,\frac{m_{\mathrm{ej}}(m)}{\langle m \rangle}\,\phi(m)\,\mathrm{d}m, \tag{16}$$

where $\Sigma_{\mathrm{SFR}}(t)$ is the mass of star formed per unit time and per unit surface area, $\tau(m)$, the lifetime of a star of mass m, and $m_{\mathrm{ej}}(m)$, its mass of gas returned to the ISM. The first term of the right hand side of Eq. (16) is the amount of gas removed by the star formation, and the second term, is the delayed injection of the gas (H, He and metals), by the various progenitors. The ISM metallicity, is defined as:

$$Z_{\mathrm{ISM}}(t) \equiv Z_{\mathrm{gas}}(t) + Z_{\mathrm{dust}}(t), \tag{17}$$

where $Z_{\mathrm{gas}}(t)$ is the metal-to-gas mass ratio, and $Z_{\mathrm{dust}}(t)$, the dust-to-gas mass ratio that will be discussed at §5.2. Its evolution is analog to Eq. (16):

$$\frac{\mathrm{d}\left[\Sigma_{\mathrm{gas}}(t)\,Z_{\mathrm{ISM}}(t)\right]}{\mathrm{d}t} = -Z_{\mathrm{ISM}}(t)\,\Sigma_{\mathrm{SFR}}(t) + \int_{m_l}^{m_u} \Sigma_{\mathrm{SFR}}(t - \tau(m))\,\frac{Y_Z(m)}{\langle m \rangle}\,\phi(m)\,\mathrm{d}m, \tag{18}$$

where $Y_Z(m)$ is the yield of elements heavier than He, by the stars of mass $[m, m + \mathrm{d}m]$.

Table 3—Continued

Name	$Z_{\rm gas}$ $[Z_\odot]$	$Z_{\rm PAH}$	$Z_{\rm dust}$	$t_{\rm SF}$ [Myr]	$n_{\rm H}$ [cm^{-3}]	f_+	$L_{\rm burst}$ $[L_\odot]$	$L_{\rm PDR}$ $[L_\odot]$
M 83	$2.3^{+0.5}_{-0.6}$	$6.0^{+3.4}_{-4.8} \times 10^{-5}$	$7.1^{+2.3}_{-2.3} \times 10^{-4}$	5440	290	0.6	2.5×10^9	1.7×10^{10}

Note. — Most of these quantities are defined in §3 and Table 2. $Z_{\rm PAH}$ and $Z_{\rm dust}$ are the PAH-to-gas and dust-to-gas mass ratios; $t_{\rm SF}$ is the age of the galaxy constrained by the optical and near-IR broad bands; $n_{\rm H}$ is the average gas density in H II regions; f_+ is the mass fraction of cationic PAHs; $L_{\rm burst}$ by the recent burst of star formation; $L^{\rm PDR}$ is the intrinsic bolometric luminosity emitted by the dust inside the neutral phase. The sources are ordered according to their metallicity. The symbol $^{(?)}$ identifies uncertain values.

The elemental yields, $Y_Z(m)$, for the low mass stars ($m \leq 8\ M_\odot$) are taken from Karakas & Lattanzio (2003a,b), and from Woosley & Weaver (1995) for the high mass stars ($m > 8\ M_\odot$). Furthermore, a prescription for the star formation rate is required, in order to solve these equations. This prescription is given by the Schmidt (1959) law, with the coefficients derived by Kennicutt (1998):

$$\frac{\Sigma_{\mathrm{SFR}}(t)}{1\ M_\odot\,\mathrm{yr}^{-1}\,\mathrm{pc}^{-2}} = (2.5 \pm 0.7) \times 10^{-10} \left(\frac{\Sigma_{\mathrm{gas}}(t)}{1\ M_\odot\,\mathrm{pc}^{-2}}\right)^{1.40 \pm 0.15} \tag{19}$$

and is used to replace $\Sigma_{\mathrm{SFR}}(t)$ in Eq. (16). Fig. 26 shows the evolution of the total metallicity, and of the reduced gas mass $\mu_{\mathrm{gas}}(t) \equiv \Sigma_{\mathrm{gas}}(t)/\Sigma_{\mathrm{gas}}^0$, where $\Sigma_{\mathrm{gas}}^0 = \Sigma_{\mathrm{gas}}(0)$ is the initial gas mass surface density.
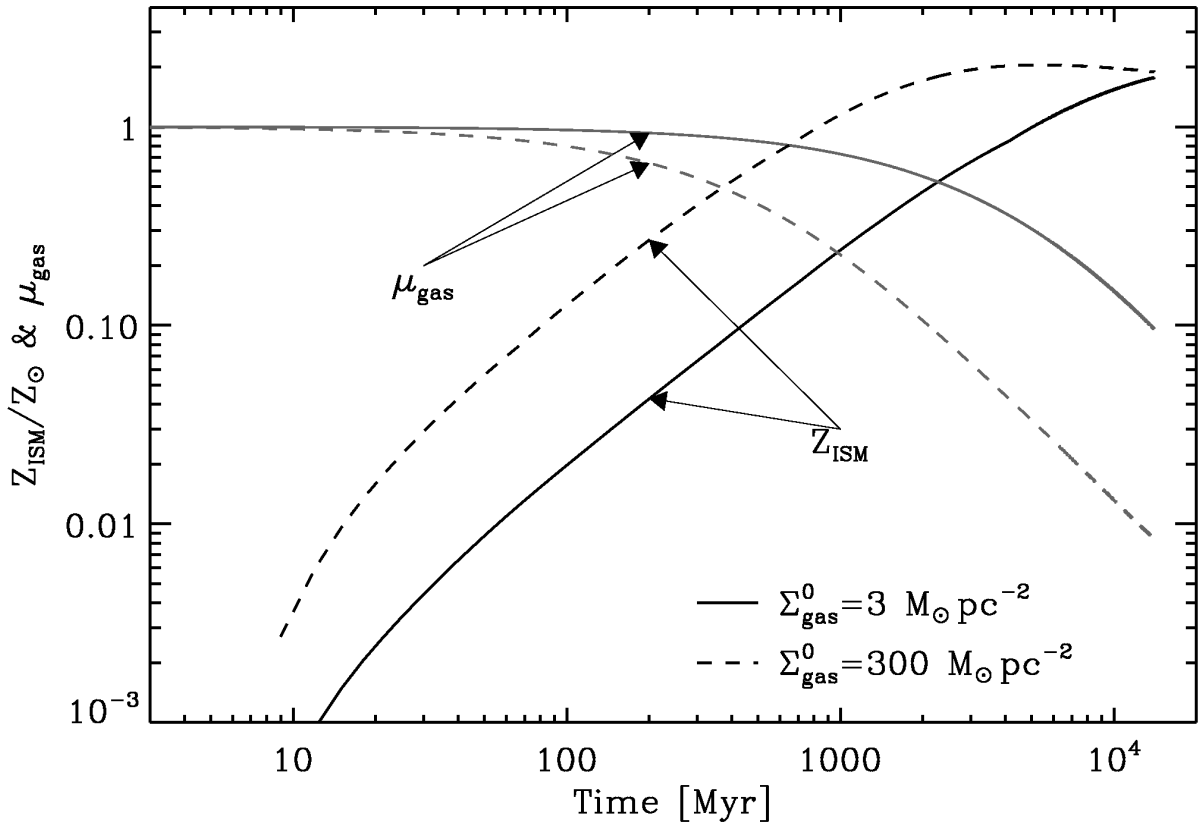
Fig. 26.— Evolution of the total metallicity (in units of $Z_\odot$), and of the reduced gas mass (μ_{gas}), for two different initial surface gas mass densities, Σ_{gas}^0.

5.2. Dust Formation and Destruction

The evolution of the mass surface density, $\Sigma_i(t)$, of a given dust specie, is the sum of three contributions: *(i)* the rate of dust destruction by star formation, *(ii)* the rate of dust condensation in stellar progenitors, *(iii)* the rate of dust destruction in the ISM, by SN blast waves:

$$\frac{\mathrm{d}\Sigma_i(t)}{\mathrm{d}t} = -Z_i(t)\,\Sigma_{\mathrm{SFR}}(t) + \int_{m_l}^{m_u} \frac{Y_i(m)}{\langle m \rangle}\,\Sigma_{\mathrm{SFR}}(t - \tau(m))\,\phi(m)\,\mathrm{d}m - \frac{\Sigma_i(t)}{\tau_{\mathrm{dust}}(t)}, \qquad (20)$$

where $Y_i(m)$ is the yield of the considered dust specie by stars of mass $[m, m + \mathrm{d}m]$, and $\tau_{\mathrm{dust}}(t)$, the dust lifetime in the ISM.

The dust yields are derived from the elemental stellar yields described at §5.1, following Dwek (1998). For low mass stars ($m \leq 8\ M_\odot$), the dust yields depend on the value of the C/O ratio. We assume that the ejecta is microscopically mixed, so that all the excess carbon is locked-up in dust, if C>O. If C<O, then we combine all the available Fe, Si, Mg, Ca and Ti, with one O atom to produce silicate dust, and titanium oxydes. For high mass stars ($m > 8\ M_\odot$), we assume that the ejecta is only macroscopically mixed, so that both carbon and oxygen rich dust can condense. We assume a condensation efficiency of unity for all dust species.

The lifetime of dust, $\tau_{\mathrm{dust}}(t)$ is directly related to the SN II rate (Dwek & Scalo 1980; McKee 1986):

$$\tau_{\mathrm{dust}}(t) = \frac{\Sigma_{\mathrm{gas}}(t)}{R_{\mathrm{SN\ II}}(t)\,\langle m_{\mathrm{ISM}} \rangle}, \qquad (21)$$

where $R_{\mathrm{SN\ II}}(t)$ is the SN II rate per unit area, and $\langle m_{\mathrm{ISM}} \rangle$ is the average effective mass of gas, swept up by a single SN remnant, where the dust is returned back to the gas phase, by either thermal sputtering, or grain-grain collision (Jones et al. 1996). The value of $\langle m_{\mathrm{ISM}} \rangle$ is largely unknown. We explore its effects, by varying it from $\langle m_{\mathrm{ISM}} \rangle = 0\ M_\odot$ (no destruction), to $\langle m_{\mathrm{ISM}} \rangle = 300\ M_\odot$ (typical destruction). The latter value is typical of our Galaxy. Indeed, if $M_{\mathrm{gas}}^{\mathrm{Gal}} \simeq 5 \times 10^9\ M_\odot$ is the total mass of gas in our Galaxy, $R_{\mathrm{SN}}^{\mathrm{Gal}} \simeq 1/30\ \mathrm{yr}^{-1}$, its average SN rate, and $\tau_{\mathrm{dust}}^{\mathrm{Gal}} \simeq 5 \times 10^8\ \mathrm{yr}$, the mean lifetime of an ISM dust particle (Jones 2004), then:

$$\langle m_{\mathrm{ISM}} \rangle \simeq \frac{M_{\mathrm{gas}}^{\mathrm{Gal}}}{R_{\mathrm{SN}}^{\mathrm{Gal}}\,\tau_{\mathrm{dust}}^{\mathrm{Gal}}} \simeq 300\ M_\odot. \qquad (22)$$

An additional destruction mechanism that apllies only to PAHs and very small grains is their photoevaporation in intense radiation fields. This destruction mechanism primarily affects the abundance of PAHs, and is taken into account in the SED model that calculates the dust abundances, by assuming that PAHs do not survive in H II regions.

Fig. 27 shows the evolution of the total dust content formed by massive stars, and the carbon dust formed by AGB stars, for various initial conditions, and destruction efficiencies. The SN II dust evolves almost linearly with the metallicity, in absence of destruction, because the metal enrichment is dominated by massive stars. In contrast, the AGB carbon dust starts rising when the metallicity of the ISM is around $1/20\ Z_\odot$. This value corresponds to a time of ~ 100 Myr (Fig. 26), which the lifetime of the most massive AGB stars. Hence, the carbon dust produced by AGB stars is injected into the ISM, with a delay which corresponds to the lifetime of the stars. This evolutionary trend was previously noted by Dwek (1998) and Morgan & Edmunds (2003). The change in the slope of the AGB carbon dust, around $1\ Z_\odot$, is simply due to the fact that AGB stars of lifetime longer than ~ 1 Gyr are oxygen rich. The dust destruction effects the evolution for $Z \gtrsim 0.1\ Z_\odot$.
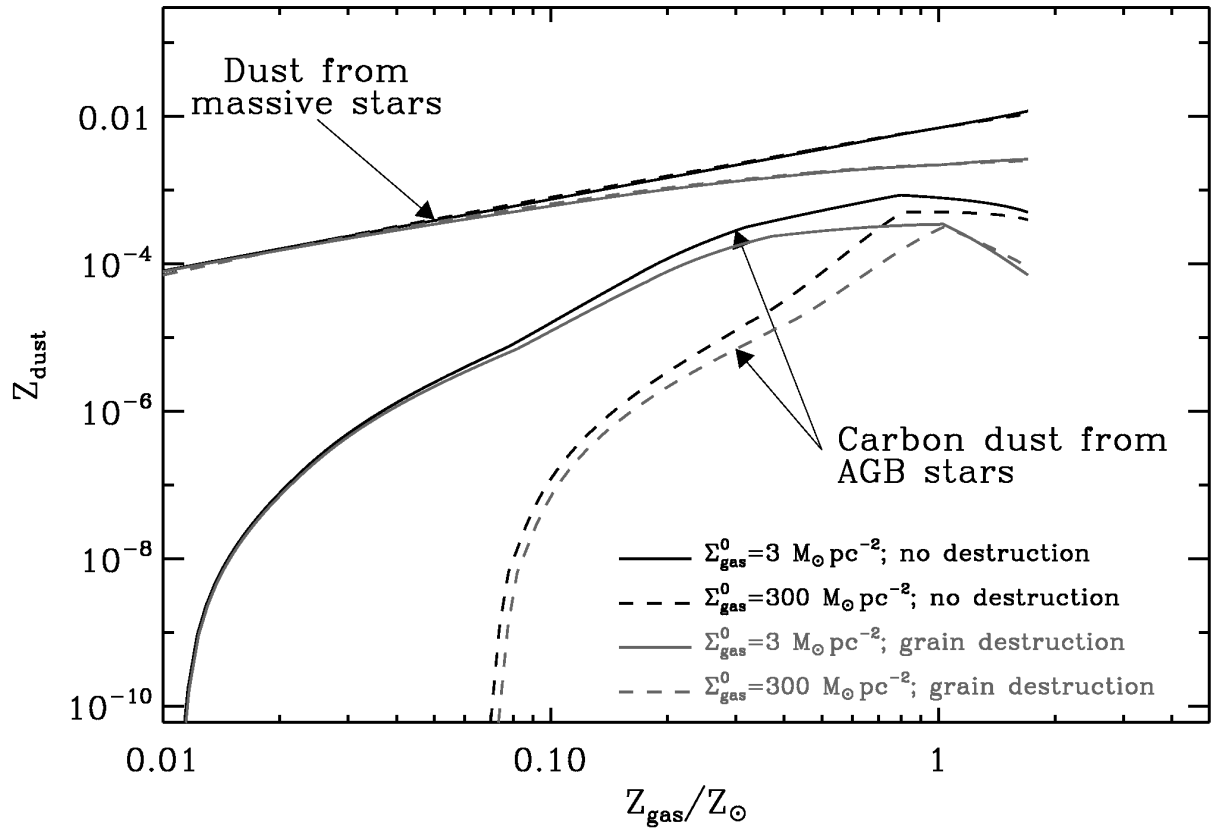
Fig. 27.— Evolution of the dust content with the metallicity of the ISM. We adopt $\langle m_{\mathrm{ISM}} \rangle = 300\ M_\odot$, for the curves with grain destruction.

5.3. Examining the Consistency Between the Stellar Populations and the Elemental Evolution

For consistency, we used the same prescription for the evolution of the star formation rate in both the population synthesis (§4) and the elemental evolution modeling (§5.1). However, we added a late burst of star formation to calculate the galactic SED, which will only have a limited effect on the final elemental abundances of the galaxy. The two models differ in the stellar yields, with the latter using the more recent yields for AGB stars. Fig. 28 examines the effect of this different yields by plotting the galactic age versus metallicity relation for our sample of galaxies. The model calculations, shown as a grey stripe, are in general good agreement with the data. However, for sub-solar metallicities ($\lesssim 0.3\ Z_{\odot}$), several galaxies appear to have an older age, from the stellar point of view, than what would be inferred from their metal enrichment. This discrepancy is probably the consequence of assuming a smooth star formation history. The differences will only manifest themselves as a moderate change in the stellar spectra, and will have no affect on the conclusions of the paper.

5.4. PAHs and the Delayed Injection of AGB Carbon Dust

From an observational point of view, PAHs are believed to form in the circumstellar envelopes of carbon rich AGB stars, and to be subsequently ejected into the ISM through stellar winds. The paucity of UV photons prevents the direct detection of these PAHs, during their formation process in the post-AGB phase of the evolution of these stars (Hony et al. 2001; Boersma et al. 2006). However, PAHs are abundantly observed during the later planetary nebula phase Hony et al. (2001). In what follows, we will assume that PAHs are only formed in the envelopes of AGB stars.

Fig. 29 shows the comparison between the dust and PAH abundances derived from the observations (Fig. 25), and the ones produced by the evolution model (Fig. 27). The agreement between the PAH-to-gas mass ratio, and the carbon dust production by AGB stars is very good, with the galaxies He 2-10 and IC 342 as the only outliers. He 2-10 is a solar metallicity blue compact dwarf galaxy. Its SED is similar to lower metallicity galaxies (Galliano et al. 2005), however its metallicity is very uncertain; for example Vacca & Conti (1992) quoted $1/6\ Z_{\odot}$. This uncertainty may reside in the fact that this galaxy has two cores, resulting from a merger. The properties of these nuclei are different in terms of dust absorption (Phillips et al. 1984), molecular gas content (Baas et al. 1994), compact source distribution (Cabanac et al. 2005), and mid-IR spectrum (Martín-Hernández et al. 2006). Thus, our global approach may not apply to this object. On the contrary the PAH-to-dust
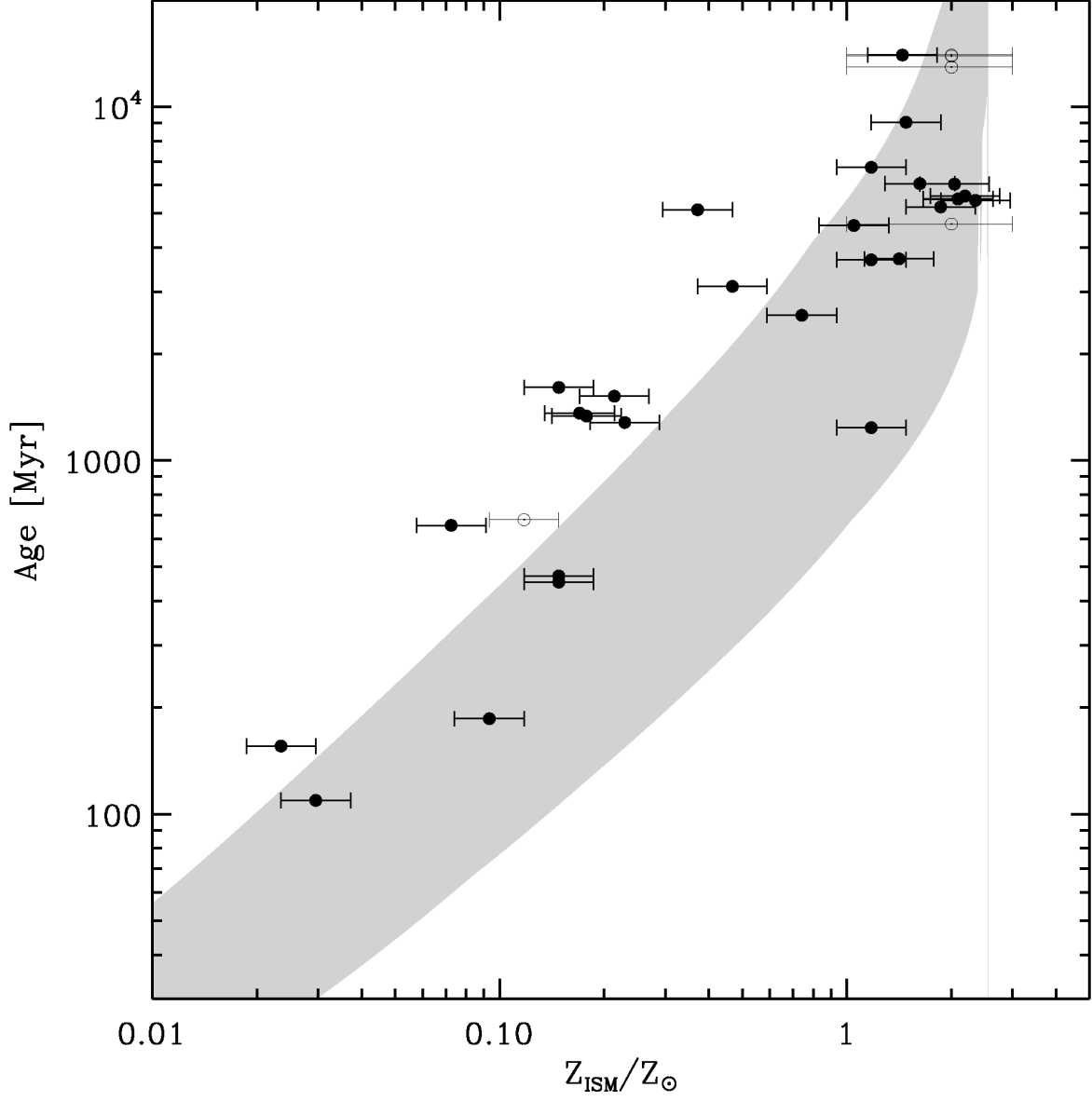
Fig. 28.— Consistency between the stellar populations and the elemental evolution. The error bars are the age of the galaxies derived from population synthesis modeling of the optical and near-IR broad-band observations (Table 3), as a function of the observed metallicity of the gas (Table 1). The grey stripe shows the range of values from the elemental evolution model (Fig. 26).
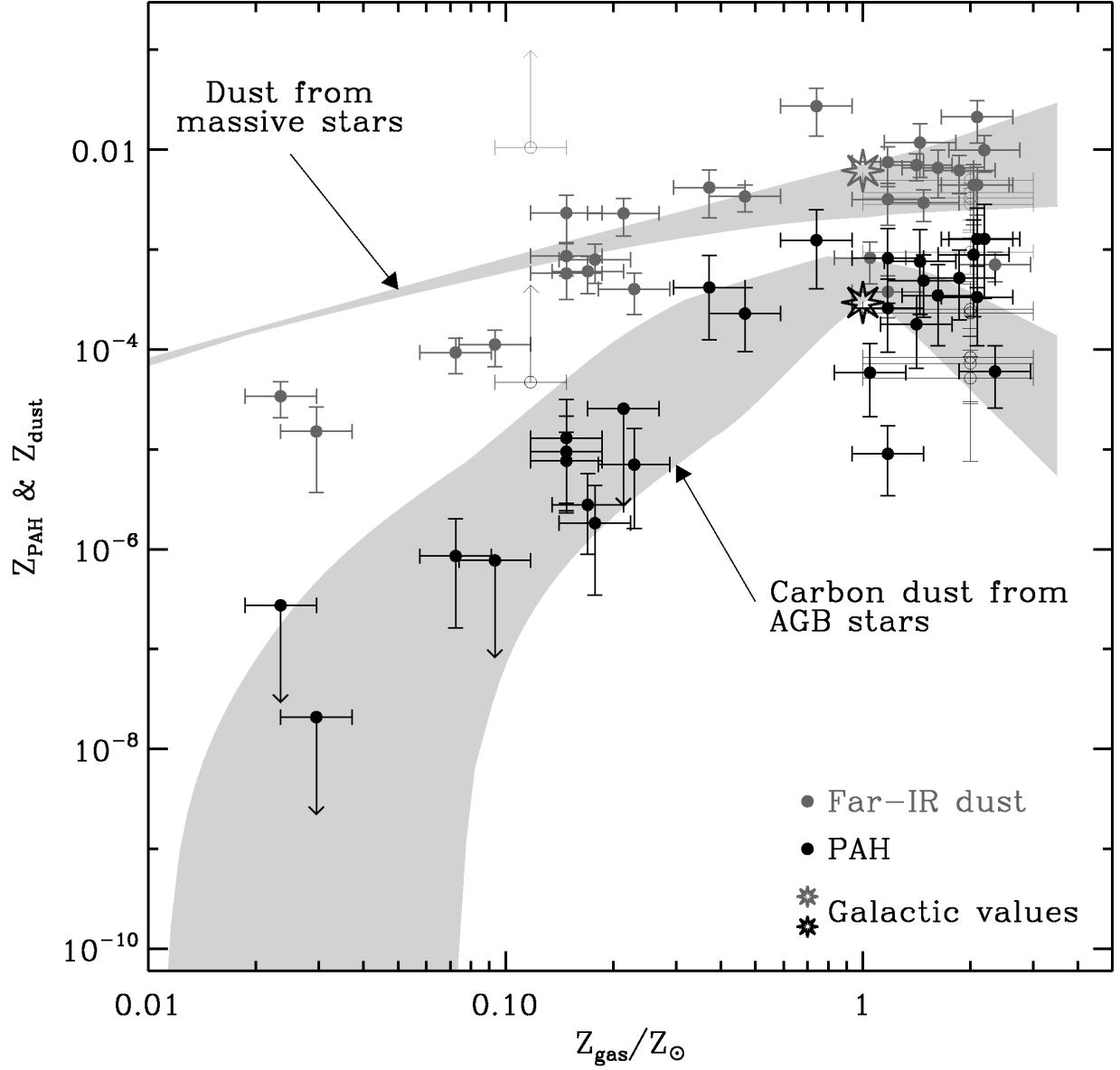
Fig. 29.— Comparison between the metallicity trends of the PAH abundance derived from the observed SED and those derived from the chemical evolution model. The figure highlights the different evolutionary trend of SN II- and AGB-condensed dust.

mass ratio of IC 342 is consistent with the one of other galaxies with the same metallicity (Fig. 25). Only its values of Z_{PAH} and Z_{dust} are systematically shifted. As mentioned in §4 this galaxy suffers a lot of extinction and confusion since it is located at low Galactic latitude. This could alter the estimate of the absolute dust-to-gas mass ratios of this object. We conclude that the striking evolution of the PAH content in galaxies with metallicity can naturally be explained by the delayed injection of carbon dust into the ISM, by AGB stars.

In principle, PAHs can form by other processes, for example, by the hydrogenation of small carbon grains in the ISM. Initially, their abundance will then follow the evolutionary trend of SN-condensed carbon dust. However, their absence in low metallicity systems suggests that they are efficiently destroyed, presumably by shocks or UV radiation, as envisioned in by Madden et al. (2006) or O'Halloran et al. (2006). At later times, the rate of PAH production by these interstellar processes will follow the evolutionary trend of AGB stars, since they will be the major source of carbon dust in the ISM.

The global trend of PAH abundance with metallicity does not preclude the possibility of local variations of PAH abundance in individual galaxies. For example, the SMC which has on the average a metallicity that is $1/6\ Z_\odot$ (Dufour et al. 1982) has at least one region, the molecular cloud SMC B1#1 (Reach et al. 2000), with a PAH-to-dust ratio that is comparable to the Galactic value (Li & Draine 2002). Even in our Galaxy, there are regions with "super Galactic" PAH abundances (e.g. Ridderstad et al. 2006). Such local abundance variations are a natural consequences of processes, such as mixing of stellar ejecta and cycling between the ISM phases, that when globally averaged, will follow the general trend of PAH abundances with metallicity depicted in Fig. 29.

5.5. The Evolutionary Trend of SN-Condensed Dust

The dust content is in good agreement with the dust production by SN II, down to $\sim 0.1\ Z_\odot$ (Fig. 29). Below this value, the model systematically overestimates the observed dust content. Lisenfeld & Ferrara (1998) found a similar deficiency, from IRAS observations of blue compact dwarf and dwarf irregular galaxies. There may be several reasons for this discrepancy.

First, we may have overestimated the gas mass, in the lowest metallicity sources. Indeed, the distribution of H I of these galaxies extends farther out of the star forming region, as discussed in §4. We have attempted to correct this effect, for I Zw 18, SBS 0335-052 and VII Zw 403, by considering only the gas content associated with the optical galaxy. However, we could not correct for the gas located out of the star forming region and along the line of

sight.

Second, we may have underestimated the dust mass by overlooking a cold dust component. Indeed, Galliano et al. (2003, 2005) showed that the millimetre excess observed in the SEDs of NGC 1140, NGC 1569, II Zw 40, and He 2-10, could be consistently explained by the presence of very cold dust, accounting for 40 to 80% of the total dust mass. On Fig. 29, the dust-to-gas mass ratio of these four galaxies is indeed, below the SN II production rate by a factor of ~ 2. Assuming that the high clumpiness of the ISM is a general property of low-metallicity systems, and that the filling factor and/or contrast density of these clumps rises when the metallicity drops, we have a natural explanation for this deviation. We can not address this issue, because of the lack of submillimetre data for these very low-metallicity galaxies.

Third, the discrepancy between the predicted and observed SN II dust at low metallicity could be due to several parameters or assumptions used in the chemical evolution modeling. (1) The IMF could play an important role in the absolute value of the dust production by SN II. It would indicate that the slope of the IMF is metallicity-dependent, and that the contribution of massive stars is lower, at very low Z_{ISM}, which seems to be unlikely, both from a theoretical point of view (star formation), and an observational point of view (star counts). (2) A much more likely explanation could come from the fact that we assumed that the condensation into dust of the elements ejected by the SN II and their mixing in the ISM is instantaneous. If the major part of the dust was to condense into the ISM, and not directly into the SN II-ejecta, then the dust formation would be delayed after the death of the massive stars. (3) Finally, the dust production rates, computed from our dust evolution model, implicitly assume that the star formation rate of the galaxy is smooth and that the mixing is instantaneous. This hypothesis is certainly valid for evolved systems, but could be wrong for very young objects. For example, Legrand et al. (2000) suggested that the star formation history of I Zw 18 is not continuous.

6. CONCLUSION AND SUMMARY

The weakness of the mid-IR aromatic features in low-metallicity environments has been traditionally interpreted as the consequence of the increased selective destruction efficiency of the PAHs in these environments. In this paper, we presented a new interpretation for the observed correlation of the intensity of the mid-IR emission from PAHs with galaxies' metallicity. In our model, this trend is a manifestation of the evolution of the abundance of interstellar carbon that formed in AGB stars with time. A fraction of the carbon dust formed in AGB stars in the form of PAH macromolecules offering a natural explanation of

the evolutionary trend of PAH abundance with galactic metallicity (or time).

To ascertain this trend, we first converted the trend of observed mid-IR fluxes to PAH and dust abundances, by modeling the UV-to-radio SEDs in a sample of 35 nearby galaxies, with metallicities ranging from 1/50 to $\sim 3~Z_\odot$. Our models represent the most detailed decomposition of the dust emission into its gas phase components using a wide range of astrophyical constraints, including: the free-free and mid-IR emissions to constrain the gas and dust radiation from H II regions; the far-IR and optical emission to constrain the ISRF that heats the dust in PDRs. From these models, we determined the abundances of the PAHs and other dust species associated to the neutral phase of the ISM. We then used a chemical evolution model to calculate the abundances of SN- and AGB-condensed dust as a function of time or metallicity. The model takes into account the delayed recycling of the ejecta from low-mass stars caused by their finite main-sequence lifetime.

The main conclusions of this paper are the followings.

1. From the decomposition of the IR emission into its various emission components and dust species, we discovered two distinct evolutionary trends for PAHs and other dust species in galaxies.

2. Comparison of these trends with the chemical evolution models showed that the abundance of PAHs follows that of the carbon dust from AGB stars. The remaining dust species follows the evolutionary trend of SN-condensed dust.

3. The delayed injection of PAHs into the ISM provides a natural explanation for the paucity of these large molecules in low metallicity systems. The subsequent rise in the PAH-to-gas mass ratio with metallicity is then a natural consequence of the increasing contribution of AGB stars to the chemical enrichment of the ISM as they evolve off the main sequence. The trend of the other dust species is a natural consequence of the evolution of SN-condensed dust which is instantaneously injected into the ISM after the birth of the progenitor star.

4. While the model is very successful in observing the gross general trend, there are some systematic deviations showing that dust-to-gas mass ratios inferred from observations fall below the calculated value for SN-condensed dust in the lowest metallicity galaxies. This discrepancy may be due to one or more of the following: *(i)* an overestimate of the H I gas mass used to derive these dust-to-gas mass ratios; *(ii)* an underestimate of the dust mass due to the possible presence of a cold dust component; and *(iii)* a more complex star formation history than used in the model calculations.

5. As an aside, in our analysis of the mid-IR spectra of nearby galaxies, we detected the 7.7 μm aromatic feature at the 4σ level in VII Zw 403, a dwarf galaxy with $Z \simeq 1/20 \; Z_{\odot}$. This is the lowest metallicity galaxy for which PAH emission has been detected to date.

The success of our chemical evolution model, in reproducing the trend of PAH abundances with metallicity, strongly suggests the importance of stellar evolutionary effects in determining the abundances and composition of dust in galaxies. These will have important consequences for determining the opacity of galaxies and their reradiated thermal IR emission. Chemical evolution models for dust must therefore be an integral part of population synthesis models, providing a self-consistent link between the stellar and dust emission components of the SED of galaxies.

REFERENCES

Allamandola, L. J., Tielens, A. G. G. M., & Barker, J. R. 1985, ApJ, 290, L25

Alloin, D., Collin-Souffrin, S., Joly, M., & Vigroux, L. 1979, A&A, 78, 200

Appleton, P. N., Davies, R. D., & Stephenson, R. J. 1981, MNRAS, 195, 327

Baas, F., Israel, F. P., & Koornneef, J. 1994, A&A, 284, 403

Bakes, E. L. O. & Tielens, A. G. G. M. 1994, ApJ, 427, 822

Bergvall, N., Masegosa, J., Östlin, G., & Cernicharo, J. 2000, A&A, 359, 41

Bernloehr, K. 1993, A&A, 270, 20

Bettoni, D., Galletta, G., & García-Burillo, S. 2003, A&A, 405, 5

Biviano, A., Sauvage, M., Gallais, P., et al. 1998, The ISOCAM dark current calibration report, Tech. rep., ESA/ISO Data Centre

Boersma, C., Hony, S., & Tielens, A. G. G. M. 2006, A&A, 447, 213

Boomsma, R., Oosterloo, T. A., Fraternali, F., van der Hulst, J. M., & Sancisi, R. 2005, A&A, 431, 65

Boselli, A., Lequeux, J., & Gavazzi, G. 2002, A&A, 384, 33

Brandl, B. R., Devost, D., Higdon, S. J. U., et al. 2004, ApJS, 154, 188

Bresolin, F., Garnett, D. R., & Kennicutt, Jr., R. C. 2004, ApJ, 615, 228

Bressan, A., Silva, L., & Granato, G. L. 2002, A&A, 392, 377

Cabanac, R. A., Vanzi, L., & Sauvage, M. 2005, ApJ, 631, 252

Carignan, C., Charbonneau, P., Boulanger, F., & Viallefond, F. 1990, A&A, 234, 43

Casasola, V., Bettoni, D., & Galletta, G. 2004, A&A, 422, 941

Cesarsky, C. J., Abergel, A., Agnese, P., et al. 1996, A&A, 315, L32

Chanial, P. 2003, PhD thesis, University of Paris VII

Coulais, A. & Abergel, A. 2000, A&AS, 141, 533

Crowther, P. A., Beck, S. C., Willis, A. J., et al. 1999, MNRAS, 304, 654

Dahlem, M., Aalto, S., Klein, U., et al. 1990, A&A, 240, 237

Dahlem, M., Ehle, M., & Ryder, S. D. 2001, A&A, 373, 485

Dahlem, M., Golla, G., Whiteoak, J. B., et al. 1993, A&A, 270, 29

Dale, D. A., Bendo, G. J., Engelbracht, C. W., et al. 2005, ApJ, 633, 857

Dale, D. A., Helou, G., Contursi, A., Silbermann, N. A., & Kolhatkar, S. 2001, ApJ, 549, 215

Dean, J. F. & Davies, R. D. 1975, MNRAS, 170, 503

Désert, F.-X., Boulanger, F., & Puget, J. L. 1990, A&A, 237, 215

Dopita, M. A., Fischera, J., Sutherland, R. S., et al. 2006a, ApJS, 167, 177

Dopita, M. A., Fischera, J., Sutherland, R. S., et al. 2006b, ApJ, 647, 244

Dopita, M. A., Groves, B. A., Fischera, J., et al. 2005, ApJ, 619, 755

Draine, B. T. & Li, A. 2007, ApJ, 657, 810

Dufour, R. J., Shields, G. A., & Talbot, Jr., R. J. 1982, ApJ, 252, 461

Durret, F., Bergeron, J., & Boksenberg, A. 1985, A&A, 143, 347

Dutil, Y. & Roy, J.-R. 1999, ApJ, 516, 62

Dwek, E. 1998, ApJ, 501, 643

Dwek, E. 2005, in AIP Conf. Proc. 761: The Spectral Energy Distributions of Gas-Rich Galaxies: Confronting Models with Data, ed. C. C. Popescu & R. J. Tuffs, 103

Dwek, E., Arendt, R. G., Fixsen, D. J., et al. 1997, ApJ, 475, 565

Dwek, E., Fioc, M., & Varosi, F. 2000, in LNP Vol. 548: ISO Survey of a Dusty Universe, ed. D. Lemke, M. Stickel, & K. Wilke, 157–+

Dwek, E., Galliano, F., & Jones, A. P. 2007, ApJ, 662, 927

Dwek, E. & Scalo, J. M. 1980, ApJ, 239, 193

Elmouttie, M., Krause, M., Haynes, R. F., & Jones, K. L. 1998, MNRAS, 300, 1119

Engelbracht, C. W., Gordon, K. D., Rieke, G. H., et al. 2005, ApJ, 628, L29

Fioc, M. & Rocca-Volmerange, B. 1997, A&A, 326, 950

Galliano, F., Madden, S. C., Jones, A. P., Wilson, C. D., & Bernard, J.-P. 2005, A&A, 434, 867

Galliano, F., Madden, S. C., Jones, A. P., et al. 2003, A&A, 407, 159

Galliano, F., Madden, S. C., Tielens, A. G. G. M., Peeters, E., & Jones, A. P. 2007, ApJ to be submitted

Gerin, M., Combes, F., & Nakai, N. 1988, A&A, 203, 44

Gonzalez-Delgado, R. M., Perez, E., Diaz, A. I., et al. 1995, ApJ, 439, 604

Grevesse, N. & Sauval, A. J. 1998, Space Science Reviews, 85, 161

Hao, L., Weedman, D. W., Spoon, H. W. W., et al. 2007, ApJ, 655, L77

Heckman, T. M., Robert, C., Leitherer, C., Garnett, D. R., & van der Rydt, F. 1998, ApJ, 503, 646

Helfer, T. T., Thornley, M. D., Regan, M. W., et al. 2003, ApJS, 145, 259

Higdon, S. J. U., Devost, D., Higdon, J. L., et al. 2004, PASP, 116, 975

Hony, S., Van Kerckhoven, C., Peeters, E., et al. 2001, A&A, 370, 1030

Hopkins, A. M., Schulte-Ladbeck, R. E., & Drozdovsky, I. O. 2002, AJ, 124, 862

Houck, J. R., Charmandaris, V., Brandl, B. R., et al. 2004a, ApJS, 154, 211

Houck, J. R., Roellig, T. L., van Cleve, J., et al. 2004b, ApJS, 154, 18

Houghton, S., Whiteoak, J. B., Koribalski, B., et al. 1997, A&A, 325, 923

Huchtmeier, W. K. & Richter, O.-G. 1988, A&A, 203, 237

Hunt, L., Bianchi, S., & Maiolino, R. 2005, A&A, 434, 849

Hunter, D. A., van Woerden, H., & Gallagher, III, J. S. 1994, ApJS, 91, 79

Inoue, A. K. 2002, ApJ, 570, 688

Israel, F. P. 1997, A&A, 328, 471

Israel, F. P. 2005, A&A, 438, 855

Izotov, Y. I., Chaffee, F. H., Foltz, C. B., et al. 1999, ApJ, 527, 757

Izotov, Y. I. & Thuan, T. X. 1998, ApJ, 500, 188

Jarrett, T. H., Chester, T., Cutri, R., Schneider, S. E., & Huchra, J. P. 2003, AJ, 125, 525

Jones, A. P. 2004, in ASP Conf. Ser. 309: Astrophysics of Dust, ed. A. N. Witt, G. C. Clayton, & B. T. Draine, 347

Jones, A. P., Tielens, A. G. G. M., & Hollenbach, D. J. 1996, ApJ, 469, 740

Jorsater, S. & van Moorsel, G. A. 1995, AJ, 110, 2037

Karakas, A. I. & Lattanzio, J. C. 2003a, Publications of the Astronomical Society of Australia, 20, 393

Karakas, A. I. & Lattanzio, J. C. 2003b, Publications of the Astronomical Society of Australia, 20, 279

Kennicutt, Jr., R. C. 1998, ApJ, 498, 541

Kessler, M. F., Steinz, J. A., Anderegg, M. E., et al. 1996, A&A, 315, L27

Kobulnicky, H. A., Kennicutt, Jr., R. C., & Pizagno, J. L. 1999, ApJ, 514, 544

Kobulnicky, H. A. & Skillman, E. D. 1997, ApJ, 489, 636

Kruegel, E. 2003, The physics of interstellar dust (The physics of interstellar dust, by Endrik Kruegel. IoP Series in astronomy and astrophysics, ISBN 0750308613. Bristol, UK: The Institute of Physics, 2003.)

Kunth, D. & Joubert, M. 1985, A&A, 142, 411

Laor, A. & Draine, B. T. 1993, ApJ, 402, 441

Laurent, O., Mirabel, I. F., Charmandaris, V., et al. 2000, A&A, 359, 887

Léger, A. & Puget, J. L. 1984, A&A, 137, L5

Legrand, F., Kunth, D., Roy, J.-R., Mas-Hesse, J. M., & Walsh, J. R. 2000, A&A, 355, 891

Li, A. & Draine, B. T. 2002, ApJ, 576, 762

Lisenfeld, U. & Ferrara, A. 1998, ApJ, 496, 145

Lundgren, A. A., Wiklind, T., Olofsson, H., & Rydbeck, G. 2004, A&A, 413, 505

Madden, S. C., Galliano, F., Jones, A. P., & Sauvage, M. 2006, A&A, 446, 877

Martín-Hernández, N. L., Schaerer, D., Peeters, E., Tielens, A. G. G. M., & Sauvage, M. 2006, A&A, 455, 853

Mas-Hesse, J. M. & Kunth, D. 1999, A&A, 349, 765

McKee, C. F. 1986, Ap&SS, 118, 383

Meier, D. S., Turner, J. L., & Beck, S. C. 2002, AJ, 124, 877

Mezger, P. G., Smith, L. F., & Churchwell, E. 1974, A&A, 32, 269

Morgan, H. L. & Edmunds, M. G. 2003, MNRAS, 343, 427

Moshir, M. & et al. 1990, in IRAS Faint Source Catalogue, version 2.0 (1990), 0

O'Halloran, B., Satyapal, S., & Dudik, R. P. 2006, ApJ, 641, 795

Ondrechen, M. P. & van der Hulst, J. M. 1989, ApJ, 342, 29

Osterbrock, D. E. 1989, Astrophysics of gaseous nebulae and active galactic nuclei (Research supported by the University of California, John Simon Guggenheim Memorial Foundation, University of Minnesota, et al. Mill Valley, CA, University Science Books, 1989, 422 p.)

Otte, B., Reynolds, R. J., Gallagher, III, J. S., & Ferguson, A. M. N. 2001, ApJ, 560, 207

Paladini, R., Montier, L., Giard, M., et al. 2007, A&A, 465, 839

Panagia, N. 1973, AJ, 78, 929

Panuzzo, P., Bressan, A., Granato, G. L., Silva, L., & Danese, L. 2003, A&A, 409, 99

Paturel, G., Theureau, G., Bottinelli, L., et al. 2003, A&A, 412, 57

Pérez-Montero, E. & Díaz, A. I. 2003, MNRAS, 346, 105

Petrosian, V., Silk, J., & Field, G. B. 1972, ApJ, 177, L69+

Phillips, M. M., Aitken, D. K., & Roche, P. F. 1984, MNRAS, 207, 25

Pilyugin, L. S., Vílchez, J. M., & Contini, T. 2004, A&A, 425, 849

Plante, S. & Sauvage, M. 2002, AJ, 124, 1995

Pustilnik, S. A., Brinks, E., Thuan, T. X., Lipovetsky, V. A., & Izotov, Y. I. 2001, AJ, 121, 1413

Ravindranath, S. & Prabhu, T. P. 2001, Ap&SS, 276, 593

Reach, W. T., Boulanger, F., Contursi, A., & Lequeux, J. 2000, A&A, 361, 895

Reach, W. T., Rho, J., Jarrett, T. H., & Lagage, P.-O. 2002, ApJ, 564, 302

Reif, K., Mebold, U., Goss, W. M., van Woerden, H., & Siegman, B. 1982, A&AS, 50, 451

Rice, W., Lonsdale, C. J., Soifer, B. T., et al. 1988, ApJS, 68, 91

Richter, O.-G., Sackett, P. D., & Sparke, L. S. 1994, AJ, 107, 99

Ridderstad, M., Juvela, M., Lehtinen, K., Lemke, D., & Liljeström, T. 2006, A&A, 451, 961

Roussel, H., Vigroux, L., Bosma, A., et al. 2001, A&A, 369, 473

Roy, J.-R. & Walsh, J. R. 1997, MNRAS, 288, 715

Sage, L. J., Salzer, J. J., Loose, H.-H., & Henkel, C. 1992, A&A, 265, 19

Sanders, D. B., Scoville, N. Z., & Soifer, B. T. 1991, ApJ, 370, 158

Sandqvist, A., Joersaeter, S., & Lindblad, P. O. 1995, A&A, 295, 585

Sargent, A. I., Sanders, D. B., & Phillips, T. G. 1989, ApJ, 346, L9

Sauvage, M., Thuan, T. X., & Lagage, P. O. 1997, A&A, 325, 98

Schaerer, D., Guseva, N. G., Izotov, Y. I., & Thuan, T. X. 2000, A&A, 362, 53

Schlegel, D. J., Finkbeiner, D. P., & Davis, M. 1998, ApJ, 500, 525

Schmidt, M. 1959, ApJ, 129, 243

Sodroski, T. J., Odegard, N., Arendt, R. G., et al. 1997, ApJ, 480, 173

Spitzer, L. 1978, Physical processes in the interstellar medium (New York Wiley-Interscience, 1978. 333 p.)

Spoon, H. W. W., Moorwood, A. F. M., Lutz, D., et al. 2004, A&A, 414, 873

Starck, J. L., Abergel, A., Aussel, H., et al. 1999, A&AS, 134, 135

Staveley-Smith, L. & Davies, R. D. 1987, MNRAS, 224, 953

Stil, J. M. & Israel, F. P. 2002, A&A, 392, 473

Storchi-Bergmann, T., Kinney, A. L., & Challis, P. 1995, ApJS, 98, 103

Struck, C. & Smith, B. J. 2003, ApJ, 589, 157

Tacconi, L. J. & Young, J. S. 1986, ApJ, 308, 600

Thuan, T. X., Hibbard, J. E., & Lévrier, F. 2004, AJ, 128, 617

Thuan, T. X., Lipovetsky, V. A., Martin, J.-M., & Pustilnik, S. A. 1999, A&AS, 139, 1

Thuan, T. X. & Martin, G. E. 1981, ApJ, 247, 823

Tielens, A. G. G. M. & Hollenbach, D. 1985, ApJ, 291, 722

Tilanus, R. P. J. & Allen, R. J. 1993, A&A, 274, 707

Vacca, W. D. & Conti, P. S. 1992, ApJ, 401, 543

van Zee, L., Westpfahl, D., Haynes, M. P., & Salzer, J. J. 1998, AJ, 115, 1000

Vanzi, L. & Sauvage, M. 2004, A&A, 415, 509

Vermeij, R., Peeters, E., Tielens, A. G. G. M., & van der Hulst, J. M. 2002, A&A, 382, 1042

Walter, F., Weiss, A., & Scoville, N. 2002, ApJ, 580, L21

Webster, B. L. & Smith, M. G. 1983, MNRAS, 204, 743

Weingartner, J. C. & Draine, B. T. 2001, ApJ, 548, 296

Werner, M. W., Roellig, T. L., Low, F. J., et al. 2004, ApJS, 154, 1

Wild, W., Eckart, A., & Wiklind, T. 1997, A&A, 322, 419

Woosley, S. E. & Weaver, T. A. 1995, ApJS, 101, 181

Wu, Y., Charmandaris, V., Hao, L., et al. 2006, ApJ, 639, 157

Xilouris, E. M., Madden, S. C., Galliano, F., Vigroux, L., & Sauvage, M. 2004, A&A, 416, 41

Yun, M. S. & Hibbard, J. E. 2001, ApJ, 550, 104

Zaritsky, D., Kennicutt, Jr., R. C., & Huchra, J. P. 1994, ApJ, 420, 87

Zubko, V., Dwek, E., & Arendt, R. G. 2004, ApJS, 152, 211